Title
Electromechanical and electron-phonon coupling in two-dimensional transition metal dichalcogenides

Author
Zhu, Hanyu

Publication Date
2016

Peer reviewed|Thesis/dissertation

Electromechanical and electron-phonon coupling in two-dimensional transition metal dichalcogenides

by

Hanyu Zhu

A dissertation submitted in partial satisfaction of the

requirements for the degree of

Doctor of Philosophy

in

Applied Science & Technology

and the Designated Emphasis

in

Nanoscale Science & Engineering

in the

Graduate Division

of the

University of California, Berkeley

Committee in charge:

Professor Xiang Zhang, Chair
Associate Professor Junqiao Wu
Professor Michael Crommie

Fall 2016

Electromechanical and electron-phonon coupling in two-dimensional transition metal dichalcogenides

Abstract

Electromechanical and electron-phonon coupling in two-dimensional transition metal dichalcogenides

by

Hanyu Zhu

Doctor of Philosophy in Applied Science & Technology
and the Designated Emphasis in
Nanoscale Science & Engineering

University of California, Berkeley

Professor Xiang Zhang, Chair

The coupling of mechanical, electrical and optical properties of materials becomes more prominent when the dimensionality is reduced to two, such that the external manipulation from the higher dimension can directly apply to the interior, and the Coulomb interaction is greatly enhanced. Among the existing two-dimensional systems, the Group VIB transition metal dichalcogenides (TMDC) are semiconductors with direct band gap. They are potential solutions for field-effect transistors with 5 nanometer node and beyond, as well as broadband nano-optoelectronics. In addition, their broken inversion symmetry and spin-orbit coupling together give rise to a pair of nonequivalent valleys as energy-efficient information carriers.

This dissertation first presents the quasi-static measurement of piezoelectric effect, i.e. the generation of strain through electric field, in ultra-thin freestanding molybdenum disulfide (MoS_2) films by atomic force microscopy. Such van der Waals layered materials overcame the thermodynamic instability when the thickness of traditional bulk materials approaches single-molecular scale. The ambient piezoelectric coefficient of a single layer, $e_{11} = 2.9 \times 10^{-10}$ C/m, represented the intrinsic symmetry breaking and was free from substrate effects. The dependence of piezoelectric response on number of layers and angle of applied electric field agreed with the crystalline symmetry. In complimentary to the natural in-plane piezoelectricity, the single-layer TMDC was chemically engineered to possess out-of-plane piezoelectricity by selectively replacing the chalcogen atoms on one side. The measured piezoelectric coefficient of $d_{33} = 0.1$ pm/V could be increased further by varying the substitute atoms. These discoveries are applicable to low-power logic switches for computing and electromechanical sensors at molecular level.

At higher frequency, the electromechanical coupling is replaced by phonon-photon interaction, such as Raman scattering and infrared absorption. We characterized the coupling between quasi-static strain and the optical phonon vibration as a result of mechanical nonlinearity in $MoTe_2$ by Raman spectroscopy. Small Grüneisen parameters of 0.45 and 0.25

were found for in-plane and out-of-plane optical phonon respectively under in-plane strain. More importantly, the hexagonal lattice enabled unique chiral phonons with intrinsic angular momentum and magnetic moment, that are capable of transporting electrons between valleys. We estimated the phonon energy from resonant Raman scattering, which came from both defect-activation and double-resonance process, and observed the phonon-assisted intervalence band transition by transient infrared spectroscopy. Infrared spectrum showed distinctive steps from virtual electronic bands projected by the absorption and emission of the valley phonon, in accordance to our theoretical model. The investigation of the phononic chirality and angular momentum conservation by probing the circular polarization of the absorption is ongoing. The valley phonon has potential in information processing and ultrafast optoelectronic modulation.

To my family

I come into being because of you, my dear parents, with unending love that I start to realize more and more. I wish what I will become is beyond your expectation, yet remains within your hope.

Day and night I feel your wholehearted support, my dear Liping, with which I am not only strengthened in the difficult path of research but also transformed into someone who knows how to give and receive care in our weaknesses.

Contents

List of Figures

List of Tables

Acknowledgments

It is my great privilege to give thanks to my mentor Professor Xiang Zhang for the opportunity to immerse in this diverse research soup called Xlab, as well as the sharp and timely instructions during the years. Your generous support and truthful consideration solely to the lifelong benefit of the students will be the guideline of my future career.

I thank Dr. Ziliang Ye and Dr. Yu Ye for your friendship and guidance, academic and non-academic alike, that have become my priceless assets. I would like to express my special gratitude to Dr. Ming Liu, Dr. Yuan Wang and Dr. Xiaobo Yin for helping me launching my first project. I am indebted to Dr. Chris Gladden, Dr. Jun Suk Rho and Dr. Kevin O'Brien for the skill training in nanofabrication and optics. I am also grateful for the talented and kind colleagues in Xlab for their contributions to my research: Dr. Shaomin Xiong, Dr. Zi Jing Wong, Dr. Sui Yang, Dr. Kedar Hippalgaonkar, Dr. Majid Gharghi, Dr. Liang Feng, Dr. Xingjie Ni, Dr. Yimin Li, Dr. Jianwen Dong, Dr. Cheng Gong, Mervin Zhao, Jun Xiao, Ying Wang and Yousif Alsaid. I thank all the other Xlab members for the stimulating time together, as well as the enjoyable and supportive atmosphere you have built. In addition, I thank Professor Lain-Jong Li, Dr. Robert A. Kaindl, Professor Peidong Yang, Professor David B. Bogy and Professor Feng Wang for support and helpful discussion. I am obliged to Dr. Ang-Yu Lu and Dr. Yiming Yang for the fruitful collaboration.

I give special thanks to my friends in Berkeley for sharing the ups and downs together, and my brothers and sisters in faith for bearing each other's burden.

Chapter 1

Introduction

Solid crystals consist of periodically ordered atoms that share electrons in the outer-shell. Due to Pauli exclusion principle in quantum mechanics, these delocalized electrons must occupy different states distinguished by momentum and spin. The energy of each electronic state is determined by the attractive Coulomb potentials of the nuclei and the tightly bound electrons (cores), as well as the repulsive interaction with other delocalized electrons. The ground state with minimal total energy is reached by adjusting the distances between the ionic cores.

When the effective electronic interaction is weak, band theory describes the dependence of electronic energy on the momentum, i.e. the band structure. Therefore, it is intuitive that when the atomic cores are forced to move, such as by mechanical stress and electric field, the electronic states will alter correspondingly. Conversely, when the electrons change state, such as through optical excitation, the atomic cores will also move accordingly. These processes can be nearly time-independent (quasi-static), periodic or non-periodic (transient).

The band structure dictates many physical behaviors of tremendous importance in ap-

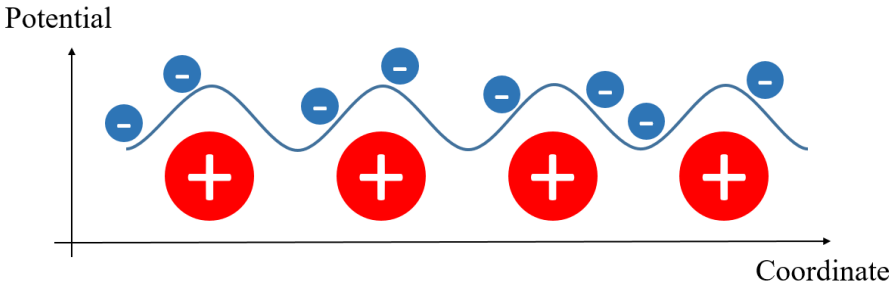

Figure 1.1: Illustration of the solid lattice. The electronic states are influenced by the core potential, while the cores are glued by the valence electrons.

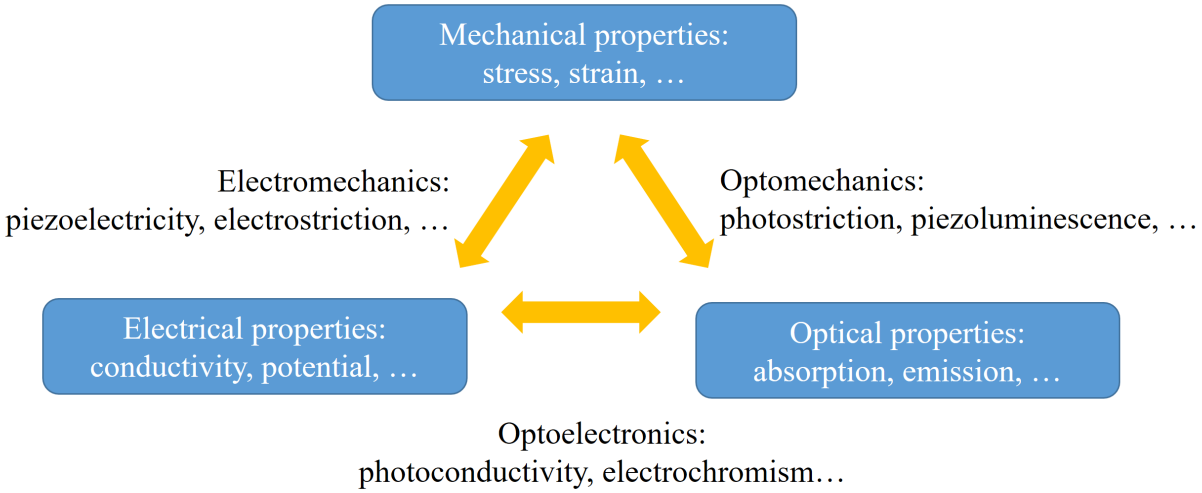

Figure 1.2: The interplay of mechanical, electrical and optical properties as a result of the electron-lattice coupling. Many physical processes associated with the interactions are named accordingly, and have found many applications in industry and consumer products.

plication, such as conductivity and optical emission. In semiconductors, where the energy difference between the highest occupied states and the lowest unoccupied states is non-zero and moderate, small variations in electronic distribution around these states can radically change the conductivity and optical absorption. For example, field effect transistors use electrostatic potential to switch the channel conductivity by orders of magnitude. In semiconductor lasers, electrons are injected into a higher energy band, lifting the population above that of a lower energy band and thus tuning the optical absorption from positive to negative. The quantitative connections behind these observables are also determined by the band structure, whose coupling to the atomic lattice gives rise to myriad of fascinating phenomena.

At the same time, the movement of atomic cores also plays important roles in physical processes like sound propagation and heat transfer. The heavier the nucleus, the slower it responds to external stimuli. A brilliant example is diamond, which has the highest thermal conductivity of any known solids partly due to the light weight of the constituting carbon atoms [1]. This property is commercially employed to distinguish real diamond from stimulants. More phenomena involving the collective motion of lattice will be discussed in the rest of the chapter.

1.1 Engineering materials by quasi-static mechanics

Even small strain can qualitatively change the band structure by separating two bands with the same initial energy, that drives the electron to preferably stay in one of them. In contrast to the original state where the electronic properties are averaged between the two bands, the new state can selectively inherit the property of the favorable band. For example, straining silicon increases the operation speed of the electronic devices in semiconductor industry [2]. The speed of carrier motion under certain electric field is related with the mobility μ:

$$v = \mu E \mu = \frac{q}{\tau m^*} \tag{1.1}$$

where q is the effective charge of the carrier, m^* is the effective mass, and τ is the average time for the carrier to lose its momentum. In silicon, there are six unoccupied band minima (valleys) for conductive electrons to reside (Fig. 1.3). Uniaxial strain lowers the energy of two valleys, such that the electron scattering from them to the other valleys are suppressed, and thus the rate of momentum loss is reduced. On the other hand, two occupied band maxima for conductive holes in silicon have distinctive effective mass. By applying strain the energy of the light hole band is raised above the heavy hole, resulting in its dominance in hole transport and boosting the mobility.

By changing the electron density, strain can also modify the energy contribution from electron-electron interaction. In some cuprate compounds, the interaction makes the electronic motion strongly correlated and no longer described by single-particle band theory. At sufficiently low temperature the correlation is significant enough to pair the electrons with opposite spin and momentum. Thus any scattering will cause opposite effect to the pair and cancels according to quantum superposition principle, and the material becomes superconductive. The critical temperature T_c can be greatly enhanced by pressure, whose record was held by $HgBa_2Ca_2Cu_3O_{8-\delta}$ for more than 20 years [3]. Recently, it was broken by H_2S through another mechanism of pressure induced superconductivity. H_2S is a molecular compound with only localized electrons, but when it is compressed so much that the energy of quantum confinement overcomes the inter-molecular barrier, the crystal becomes metallic and superconducting [4].

Although global hydrostatic pressure is convenient for fundamental research and has little prerequisite from the materials, it is difficult to implement for real application. In contrast, applying local mechanical stress to materials are more feasible but highly dependent on their geometry, microstructure, defect density etc. The uncertainty diminishes at nanoscale when the local crystalline structure becomes nearly perfect and the mechanical strength approaches ideal value [5]. Therefore, nano-materials are more suitable for elastic strain engineering [6]. A classical technique to induce stress is epitaxial growth on lattice-mismatched substrate, where the lattice constant of the film is slightly different (usually within a few percent) from the supporting single crystal (Fig. 1.5). It is the foundation of the previously mentioned strained silicon technology [7], as well as the engineering of novel multiferroic materials [8].

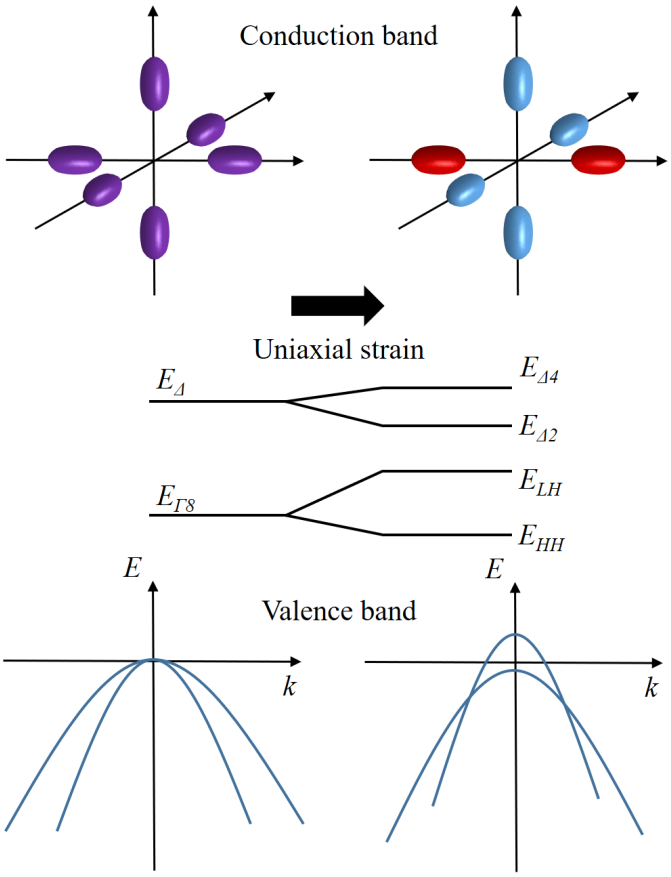

Figure 1.3: Uniaxial strain affects the band structure of silicon and increases the mobility of both electrons in conduction band and holes in valence band.

It only works for very thin films because the accumulated stress energy is proportional to the film thickness. When this energy surpasses the nucleation barrier of defects, the lattice will reconstruct and relax the stress.

1.2 Electrons modified by phonon

Phonon is defined as the quantum unit of the collective lattice vibration, usually with a well-defined spatial periodicity (momentum) and frequency (energy). Although each atom has only small displacement around its equilibrium position, the envelop of the motion can propagate through the lattice (Fig. 1.6). In most cases, since the electrons are sufficiently light and fast, they always reach equilibrium at any given lattice configuration. Under this adiabatic approximation, electrons remain in the ground state but each state has modified

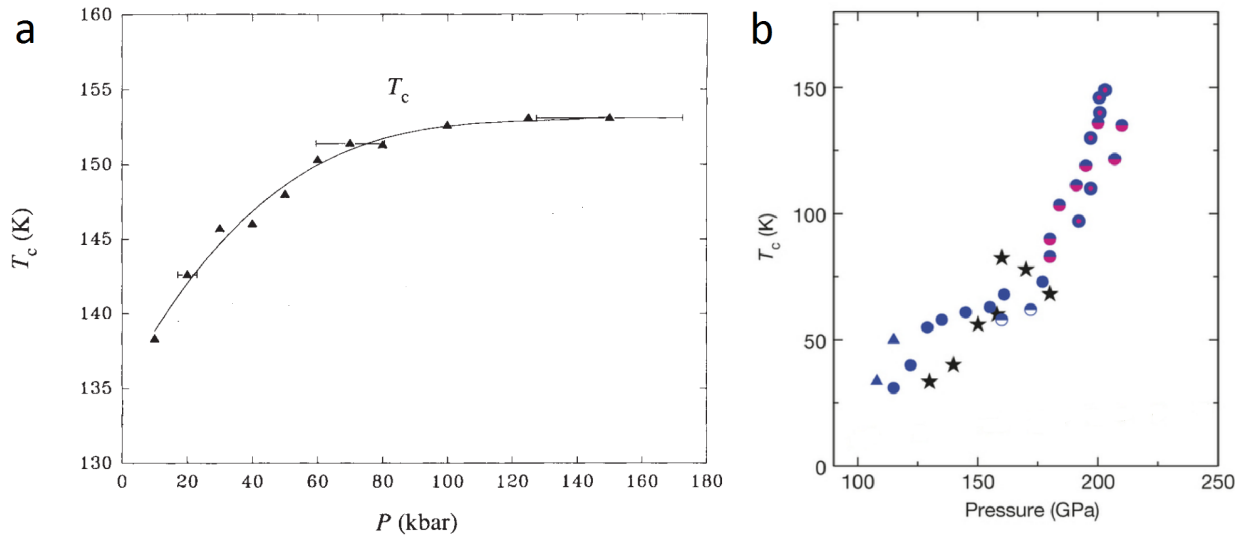

Figure 1.4: Enhancement of superconductivity by pressure in (a) $HgBa_2Ca_2Cu_3O_{8-\delta}$ and (b) H_2S. The stars and circles in (b) denote theoretical and experimental values, respectively. Reprinted with permission from [3, 4]. Copyright Nature Publishing Group.

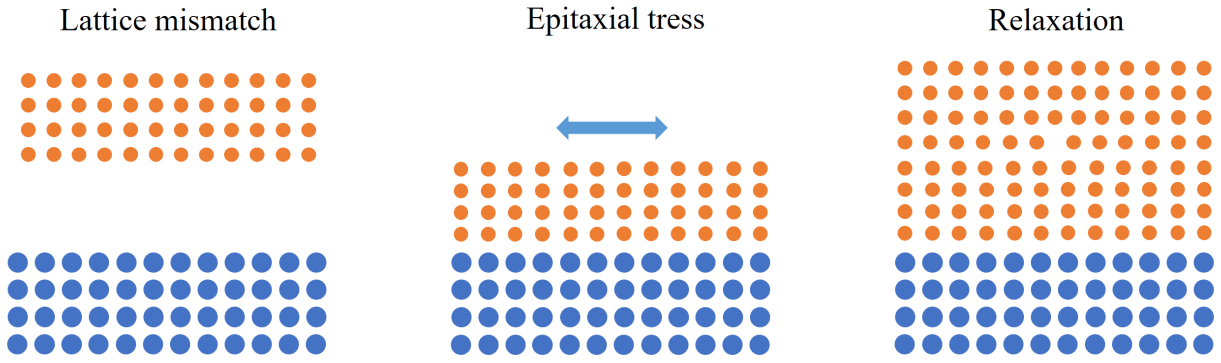

Figure 1.5: Strain of epitaxially grown lattice-mismatched thin film created by enforcing the one-to-one connection between the unit cells of the film and the substrate. However when film becomes thicker, strain tends to relax by the formation of defects.

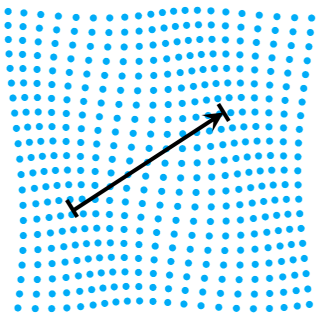

Figure 1.6: Classical depiction of vibrational wave inside a solid lattice propagating along the arrow direction. The length of the arrow equals to the wavelength.

wave function and acquires additional energy. Therefore, the vibration is sustained by the energy transfer back and forth between the kinetic energy of the cores and the electronic energy.

Although individual phonons are not directly visible like photons, due to the low energy levels they are easily excited by thermal fluctuation at room temperature and therefore cause many observable effects. They can be created in the hotter region of a material, propagate to the cooler region and conduct heat. This is particularly important in the situations where good thermal conductivity and electrical insulation are needed, like the packaging of electronics [9]. On the other hand, heat loss from phonons are undesirable for thermoelectricity, where the thermal energy should be funneled to driving electrons and generating voltage [10]. One of the most successful engineering approaches to suppress thermal conductivity while retaining the electrical conductivity is to reduce the characteristic grain size [11]. This is because the phonon mean free path is much longer than electron mean free path in typical thermoelectric materials. When the grain size is smaller than the former but larger than the latter, the boundaries only effectively impede the phononic flow.

Phonon is also the major source of electron scattering in pure, non-magnetic crystal. Qualitatively, when electron passes through the lattice, local excessive charge deforms the nearby lattice and creates phonon. For ionic crystals consisting of positive and negative ions in the lattice, the Coulomb interaction between electrons and ions greatly enhances this interaction. In semiconductor, the probability of such a process is translated to scattering rate and limits the mobility at room temperature [12]. Even when the electron does not move, it constantly emits and reabsorbs virtual phonons. The combined entity of electron and surrounding phonon cloud is called polaron, which has a higher effective mass than the original electron [13]. In some metals where the electron-phonon interaction is strong enough, the virtual phonon can capture another electron and generate an effective attraction between electrons. This pairing mechanism (BCS theory) does not require strong correlation and explains the superconductivity in a wider range of metals [14]. Conversely, the scattering

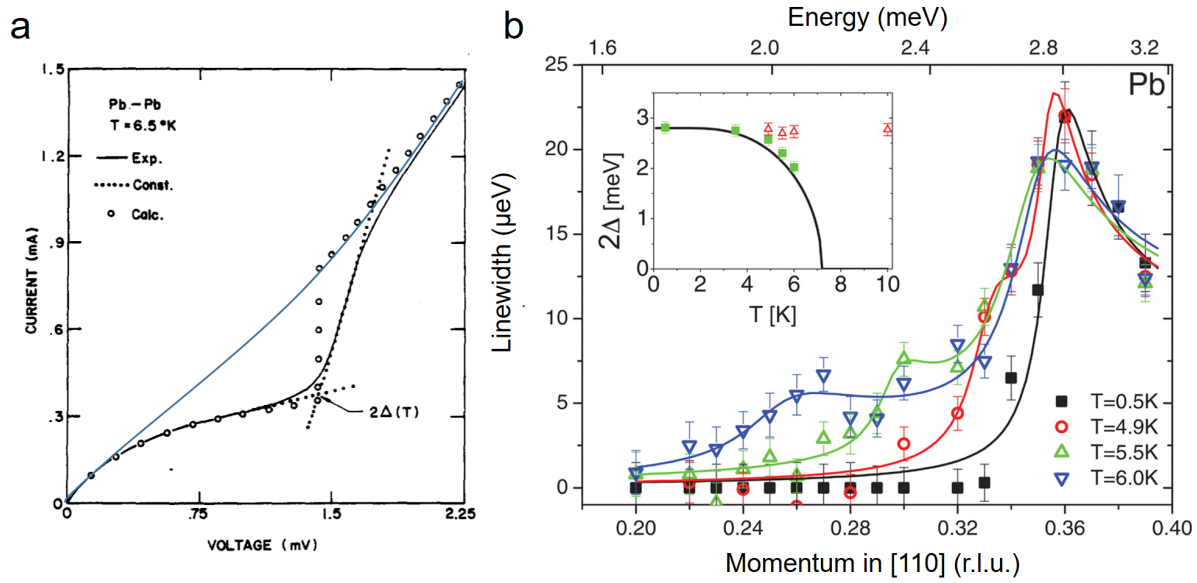

Figure 1.7: Experimental evidences of electron-phonon coupling. (a) The phonon-induced electronic band gap in superconductive Pb measured by tunneling spectroscopy (black curve). The slope of tunneling current as a function of the bias voltage is proportional to the electronic density of state (DOS). The blue line schematically shows the expected tunneling current without electron-phonon coupling for an almost constant DOS. The markers are calculated from BCS theory. Reprinted with permission from Ref. [16]. (b) The electron induced phonon damping (Kohn anomaly) in Pd around 0.35 reciprocal lattice units (r.l.u.) at different temperature measured by inelastic neutron scattering. The solid lines are fitting from BCS theory. Phonon with this momentum connects two electrons with opposite momentum at the Fermi level and therefore has higher damping rate and broader linewidth. Since the process depends only on the electronic momentum at the Fermi level, its peak position does not change with temperature (red triangles in the inset). The phonon bump on the left side of this peak that progressively moves toward it at lower temperature corresponds to the electronic gap width as plotted in the inset (green squares). The gap also agrees well with BCS theory (solid line). From Ref. [17]. Reprinted with permission from AAAS.

of phonons by electrons is also menifested in phonon energy and linewidth, known as the Kohn anomaly [15].

Furthermore, phonon can couple with light through the mediation of electronic states. When an electron absorbs a photon and transits to an excited state, its wavefunction changes and disturbs the surrounding atoms. With a very small probability (usually less than part of a million) it emits a phonon before transiting back to the ground state and emit a photon. The net effect is that the photon transfers some energy to a phonon. Since the phonon energy

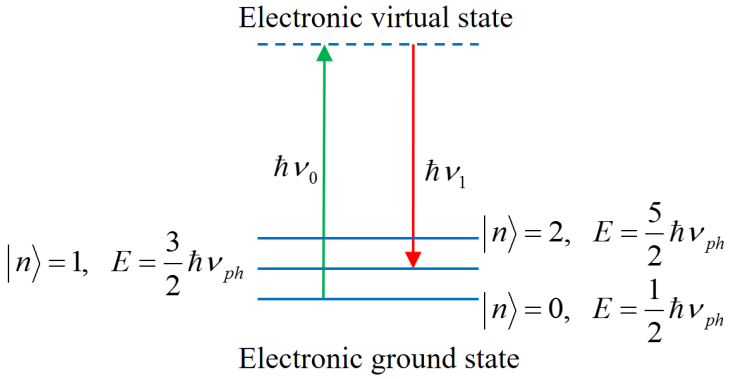

Figure 1.8: Electron in the ground state absorbs the incident photon energy $\hbar\nu_0$, transits to a virtual state, goes back to the ground state dressed with a phonon and emits a photon with lower energy $\hbar\nu_1$. The energy difference is equal to the phonon energy $\hbar\nu_{\mathrm{ph}}$. In some cases the excited state is real and the probability of the transition increases (resonance Raman scattering). In addition, the final state can add more than one phonons (multiple-phonon scattering) or have less phonons than the original state (anti-Stokes Raman scattering).

is characteristic to the materials, this resulting difference of the photon energy (Raman spectroscopy, Fig. 1.8) is widely used to identify the components and the states of the materials.

In order to enhance this very inefficient process, the photon, phonon or both are guided to pass the same area repeatedly [18]. Such an engineered structure that holds the photon or phonon is called a resonant cavity, because it selectively enhances one optical or acoustic mode at a certain frequency while rejecting other modes with nearby frequencies. With higher photon flux, the system starts lasing when the presence of a previously emitted photon-phonon pair stimulates the emission of the next pair with identical energy and phase [19].

1.3 Two-dimensional materials

Dimensionality is a fascinating subject in physics. The classical Newtonian mechanics and Maxwell equations are defined in three-dimensional (3D) space. However, by including the time as the fourth dimension and allowing transformation of the 3+1 dimensional spacetime, the unified theory of electromagnetism and the general relativity emerge. The power of the new paradigm lies in its ability to predict new physical phenomena unexpected from the old 3D theory, such as time dilation of moving objects [20] and gravitational wave [21]. These successes stimulated further research on the possibility of unifying more fundamental

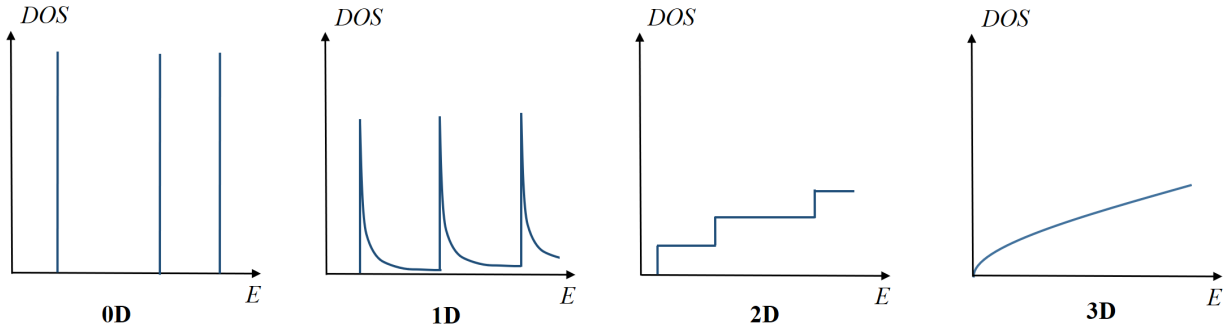

Figure 1.9: The density of states in 0-, 1-, 2- and 3- dimensional space.

interactions with additional dimensions. For example, in string theory the quantization of elementary particles is automatically enforced by the boundary condition in the extra closed dimensions too small to observe directly.

In comparison, low-dimensional systems are easier to realize by confining a particle's movement in a dot, line or plane. In these scenarios, the density of possible quantum modes of the particle at a given energy (density of states, DOS) changes qualitatively. Since the strength of many interactions are proportional to the DOS of the participants, the ground state of the system as well as the elementary excitations in low-dimensional systems are different from their 3D counterpart. For particles with isotropic quadratic kinetic energy in n-dimensional space:

$$E_k = \frac{(\hbar k)^2}{2m^*} \tag{1.2}$$

$$D_n(E) = \frac{\mathrm{d}\Omega}{\mathrm{d}E} \propto \frac{\mathrm{d}k^n}{\mathrm{d}E} \propto m^{*\frac{n}{2}} E^{\frac{n}{2}-1} \tag{1.3}$$

where k is the momentum, Ω is the number of possible states with energy lower than E and m^* is the effective mass. The fact that the DOS does not go to zero at $E \to 0$ in low-dimensional systems has profound consequences in thermodynamics and phase transition [22].

Low-dimensional systems are experimentally observed primarily in three ways. First, in some materials, the strongly anisotropic crystalline structure limits the motion of the particles. For example, in layered metallic transition metal dichalcogenides, the chemical bonds and the electronic states are primarily confined within the layer while the interlayer coupling is weak van der Waals type. The electron-phonon interaction is thus quasi-2D and much stronger than in isotropic 3D materials. It gives rise to charge density wave, in which the Kohn anomaly softens the phonon to zero energy and the lattice distortion becomes permanent [23–25]. Second, due to the presence of sharp potential gradient, the edge, surface and interface of materials usually support quasi-particle states different from the bulk states. The

low-dimensional edge states can be separately studied if the contributions of the bulk states to certain physical observables are suppressed. For example, two-dimensional electron gas (2DEG) forms at the interface of semiconductor heterojunction, semiconductor-insulator interface [26] or even insulator-insulator interface [27]. The edge states also play a critical role in quantum hall effect [28] and topological insulators [29]. Third, chemical synthesis of nanomaterials [30–33] and exfoliation [34] produce true freestanding low-dimensional structures. The interior of the materials is thus fully accessible in terms of observation and manipulation [35, 36]. Compared with 0D (quantum dots) and 1D (nanotubes and nanowires), the planar 2D nanomaterials have the advantage of scalable production and compatibility to conventional thin-film nanofabrication processes. The diversity of naturally crystallized layered materials from insulators, to semiconductors, to semimetals and metals also provides much more research opportunities (Fig. 1.10) [37, 38]. Such a rich library, combined with the fact that they can be arbitrarily stacked without any requirement of lattice match, leads to endless possibilities of heterojunctions with artificial physical interactions, as well as device configurations [39, 40].

2D materials became one of the main focus of materials research since the identification and electrical characterization of single-atomically thin graphene [34]. The production is based on the weak van der Waals interlayer bonding of graphite, and later generalized to various layered materials [42]. Since in the base materials electronic states are not strictly 2D despite of the weak interlayer coupling, the band structures of the resulting monolayers are expected to differ from the base [43]. Graphene, for instance, holds chiral Dirac fermions in contrast to the massive carriers in graphite. Its unique band structure allows the study of high energy particle physics in the condensed matter platform and has generated many exciting discoveries [44]. Yet it also leads to the lack of band gap and prevents the application of such a high-mobility material in energy-efficient field-effect transistor. Nevertheless, owning to its flexibility, superior conductivity, excellent stability and optical nonlinearity, graphene electronics and optoelectronics have been demonstrated for potential industrial implementation [45–47]. For the layered materials with band gap, the difference of band structures between bulk and single layer is also significant. For example, the group VIB transition metal dichalcogenides are known to be indirect semiconductors and never received attention as active optical materials. However the unexpected discovery of photoluminescence in monolayer MoS_2 revealed an indirect-to-direct band gap transition. Since then various two-dimensional optical and optoelectronic devices have been developed, including light emitting diode, photovoltaic devices [48–50] and lasers [51–53].

Other than the DOS, the optoelectronics in 2D materials presents an additional character in contrast to bulk and interfacial electron gas: strong excitonic effect that enhances light matter interaction. Exciton is defined as an electron-hole pair bound by Coulomb attraction. In the simple hydrogen model (positive and negative charge in homogeneous dielectric medium) the binding energy is:

$$E = \left(\frac{e^2}{4\pi\epsilon_0\epsilon_r}\right)^2 \frac{m_{\text{eff}}}{2\hbar^2} \tag{1.4}$$

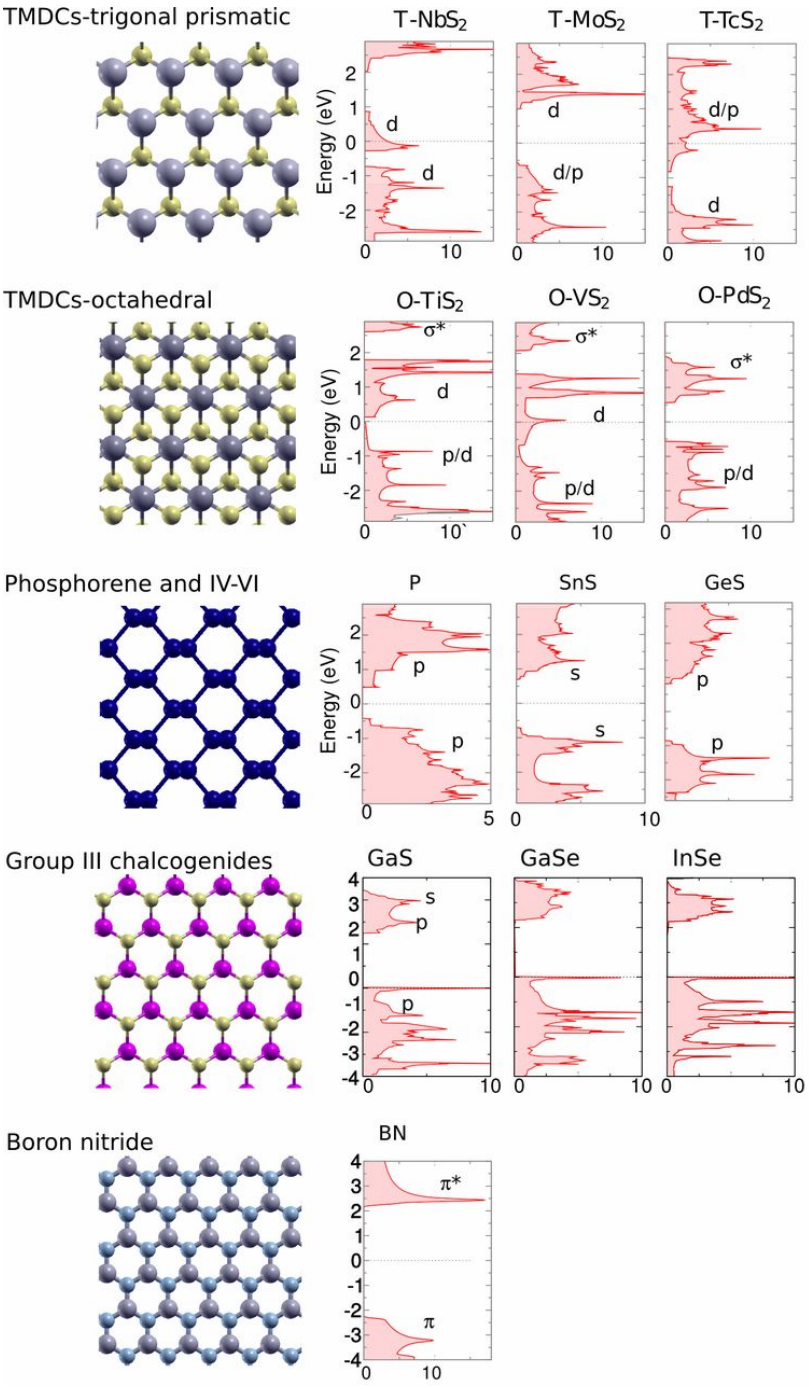

Figure 1.10: The structures and electronic properties of various 2D materials. From top to bottom: metal, semimetal, narrow-gap semiconductor, wide-gap semiconductor and insulator. From Ref. [41]. Reprinted with permission from AAAS.

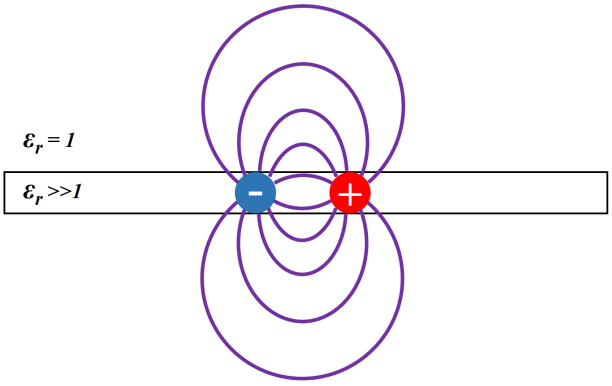

Figure 1.11: The strong Coulomb interaction in two-dimensional materials comes from the weak dielectric screening of the materials. Although the dielectric constant inside the film is large, most of the electric field leaks outside the film and experience the dielectric constant of the vacuum. This effect becomes prominent only when the thickness of the film is smaller than the diameter of the exciton, which is on the order of nanometers.

In many traditional systems the relative dielectric constant ϵ_r is large, which reduces the binding energy. Therefore at room temperature thermal fluctuation can easily break the pair and the excitonic effect is usually negligible. But in freestanding 2D systems the environment is mostly vacuum and the average ϵ_r is close to 1 (Fig. 1.11), causing the binding energy to be order of magnitude larger than thermal fluctuation. Consequently, the optical absorption spectrum of the material is no longer proportional to the electron-hole joint density of states, but exhibits sharp peaks below the band gap corresponding to the excitonic ground state [54–56]. On the optical resonance, since the spatially localized pair must have a broad range of momentum following the Fourier transformation, it covers many electron-hole modes and has much larger coupling strength than a single mode. Therefore, the single-molecular layer absorbs a significant portion of the incident light at the peak wavelength [57]. The intrinsic spontaneous emission rate is also orders of magnitude higher than that of traditional semiconductors [58, 59].

Another unique feature of 2D materials is their electrical tunability. More than 0.1 carrier per unit cell can be injected through electrostatic gating [60], unlike in conventional materials where such a large doping is only possible via chemical doping. Electrostatic gating is cleaner experimental approach to control carrier density because it eliminates the possible side effect of introducing other elements, as well as the sample-to-sample variation [61]. The free carriers strongly influence the linear and nonlinear optical properties of 2D materials because charged excitons have lower energy than neutral excitons, and also because of charge induced band renormalization [57, 62, 63].

1.4 Structure of this thesis

Based on the discussion above, two-dimensional materials are ideal research platforms owning to their outstanding nanomechanical properties [64] that potentially enables significant mechanically induced electronic and optical effects [65], together with the strong phonon-electron interaction [66]. This thesis presents four works in line with these directions in the following sequence:

- Chapter 2-3: the quasi-static mechanical strain controlled by electric field in 2D materials. Content partly comes from [67] and [68].
- Chapter 4: the coupling of quasi-static mechanical strain and high-frequency phonon. Content partly comes from [69]
- Chapter 5: the ultrafast interaction between phonon and light. Content partly comes from [70]

Chapter 2

Piezoelectricity in monolayer molybdenum disulfide

2.1 Introduction to piezoelectricity

Piezoelectricity is defined as the generation of charge at the surface of a material under stress, or conversely the strain induced by electric field (Fig. 2.1). There is a linear relationship between the electrical and mechanical quantities, represented mathematically by the piezoelectric coefficient d_{ij}:

$$d_{ij} = (\frac{\partial D_i}{\partial T_j})\Big|_{\mathbf{E}=0} = (\frac{\partial S_j}{\partial E_i})\Big|_{\mathbf{T}=0} \tag{2.1}$$

where i, j denote the components of the tensors, $\mathbf{D}$ the displacement field (from which charge distribution can be calculated as $\rho = \nabla \cdot \mathbf{D}$), $\mathbf{T}$ the stress tensor, $\mathbf{E}$ the electric field and $\mathbf{S}$ the strain tensor. Another commonly used piezoelectric coefficient e_{ij} is defined by changing the variables:

$$e_{ij} = (\frac{\partial D_i}{\partial S_j})\Big|_{\mathbf{E}=0} = (\frac{\partial T_j}{\partial E_i})\Big|_{\mathbf{D}=0} \tag{2.2}$$

The two coefficients are related with each other by the stiffness tensor $\mathbf{s}$ of the material:

$$\mathbf{d} = \mathbf{s} \cdot \mathbf{e} \tag{2.3}$$

Piezoelectricity occurs in most crystals without inversion symmetry, whose lattice cannot overlap with itself after point reflection, except for those belonging to the chiral octahedral group (432). This is always true for polar materials, although many non-polar crystals are also inversion asymmetric and piezoelectric. Within the polar family, some of them exhibit switchable polarity under moderate electric field [71]. These materials usually undergo structural change and lose their polarity at elevated temperature, because the energy barrier for

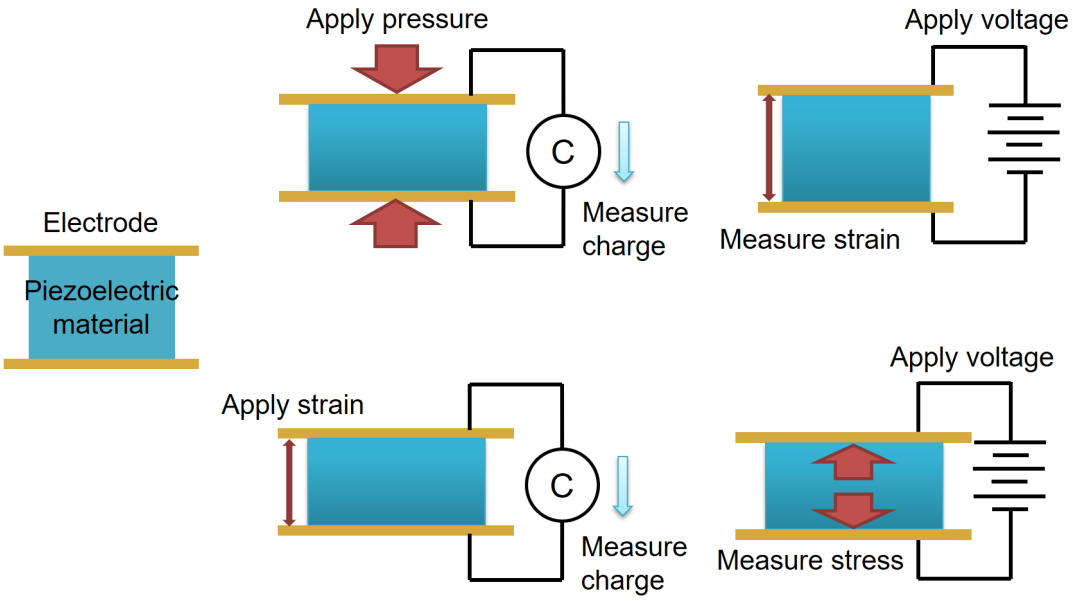

Figure 2.1: The definition of piezoelectricity corresponding to the partial derivatives in Eq. 2.1 and 2.2.

the unit cell to flip orientation is easily overcome by thermal fluctuation [72]. The formation of spontaneous polarization is named ferroelectricity in analogous to the spontaneous magnetic polarization in iron (ferromagnetism).

Since its discovery in 1880, piezoelectricity has found a wide range of applications as sensors, generators and actuators because of the precise and robust conversion between electricity and mechanical force [73]. The rapidly growing demand for high-performance and miniaturized devices in micro-electro-mechanical systems (MEMS) and electronics calls for nanoscale piezoelectric materials [74–76], motivating theoretical investigations of novel low-dimensional systems such as nanotubes and single molecules [77, 78]. Reducing the dimensionality of bulk materials has been suggested to enhance piezoelectricity [79]. However, when the thickness of a material approaches a single molecular layer, the large surface energy can cause piezoelectric structures to be thermodynamically unstable [80]. Therefore, there is no experimental evidence of single-molecular-layer piezoelectricity so far [81]. Recent calculations have predicted the existence of piezoelectricity in these two-dimensional crystals due to their broken inversion symmetry [82]. Given the ability of transition-metal dichalcogenides (particularly MoS_2) to retain their atomic structures down to the single-layer limit without lattice reconstruction even under ambient conditions, our objective to experimentally demonstrate for the first time piezoelectricity in free-standing single-molecular-layer MoS_2. In addition, we will develop a method to quantitatively measure the piezoelectric coefficient in two-dimensional materials.

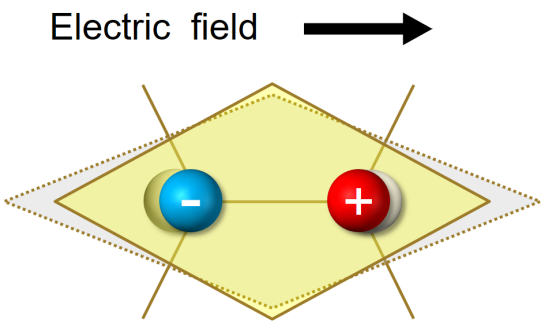

Figure 2.2: Microscopically, the piezoelectricity originates from broken inversion symmetry. Under electric field, the positively and negatively charged ions move in opposite direction and deform the unit cell.

The piezoelectric constants of MoS_2 and other 2D materials calculated in [82] are moderate compared with many other existing materials. However, it is more often that the specific application, rather than merely the value, determines the choice of materials. For example, the relaxor ferroelectrics has the highest strain-electric-field ratio and are widely used in actuators [83]. Yet they are not good at retaining the polarization without external field (hence the name relaxor) and therefore cannot convert mechanical force backward to electricity. Applications that require bidirectional conversion, such as surface acoustic wave devices must use hard ferroelectrics like $LiNbO_3$, despite of their lower piezoelectric response. For precise oscillators the electric and mechanical properties must be highly stable, and single crystal quartz is most common regardless of its very low piezoelectric coefficient.

2.2 Piezoresponse force microscopy

Studying the electromechanical interaction at nanoscale requires precise control over local electrical environment as well as high sensitivity of displacement. These stringent requirements were first satisfied in the late 1960s with the invention of topografiner [84], where a bias was applied between a sharp tip and the sample, and the displacement of 3 Å close to the surface was controlled by the field emission feedback. The feedback signal was later replaced by tunneling current, as in the case of scanning tunneling microscopy [85]. Shortly after, the function of force measurement was added by monitoring the elastic deformation of the cantilever on which the tip is mounted [86]. Finally, an optical lever scheme was devised to measure the bending of the cantilever with $\sim 10^{-3}$ Å$/\sqrt{\text{Hz}}$ sensitivity.

Based on these techniques, piezoresponse force microscopy was developed for investigating the electric-field-induced mechanical strain [87]. The tip is constantly in contact with the sample, i.e. there is repulsive force between them. The height of the tip is maintained by

Table 2.1: Piezoelectric coefficients and fields of application of common materials

	Formula	**Piezoelectric coefficient (pm/V)**	**Application**
Lead zirconate titanate	$Pb(Zr, Ti)O_3$	d_{33} = 100-700 (composition dependent)	Motors and actuators
Lithium niobate	$LiNbO_3$	$d_{15} = 63$	Surface acoustic wave filters
Polyvinylidene fluoride	$(CH_2CF_2)_n$	d_{31} = 20-30 (composition dependent)	Biomedical devices
Zinc oxide	ZnO	$d_{33} = 12$	Microgenerators
Paratellurite	TeO_2	$d_{14} = 8.1$	Optical modulators
Monolayer molybdenum disulfide	MoS_2	$d_{11} = 3.7$ (theory)	Nano-sensors (perspective)
Aluminum Nitride	AlN	d_{33} = 2-5 (process dependent)	Devices for high temperature environment
Quartz	SiO_2	$d_{11} = 2.3$	Oscillators and microbalances

a low-frequency feedback loop that keeps this force constant. A high-frequency alternating bias is applied between the tip and the sample, so that the sample near the tip experience an oscillating electric field. If the sample is piezoelectric, the field creates a proportional local strain:

$$\mathbf{S}(\omega) = \mathbf{d} \cdot \mathbf{E}(\omega) \tag{2.4}$$

where ω is the angular frequency of the bias. Assuming there is sufficient friction and no relative shift between the sample and the tip, the overall effect of the strain field is the mechanical vibration $\mathbf{A}(\omega)$ of the surface together with the tip:

$$\mathbf{A}(\omega) = \mathbf{d}_{\text{eff}} V(\omega) \tag{2.5}$$

where $\mathbf{d}_{\text{eff}}$ is a vector effective piezoelectric coefficient that depends on the geometry of the sample and includes all the anisotropic contributions from elasticity, electric permittivity and piezoelectricity. It is also affected by the geometry of the tip, environment, surface quality etc. Therefore quantitative interpretation of the measurement result is usually challenging [88].

Note that the piezoelectric coefficient is generally very small (∼pm/V) and the corresponding net displacement is often much lower than the noise of position measurement and drift. In addition, there are many other tip-sample interactions, such as electrostatic force [89]:

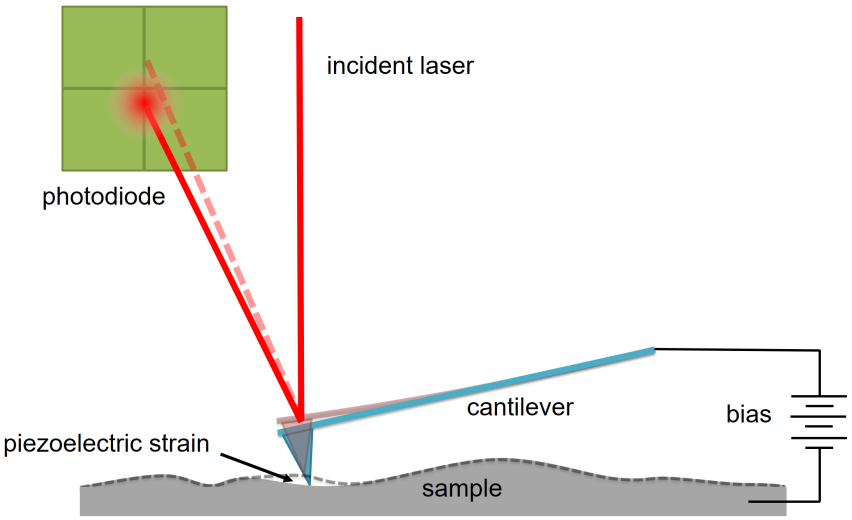

Figure 2.3: Piezoresponse force microscopy measures the local displacement induced by tip bias. The strain bends the cantilever and deflects the laser beam. The beam is projected on a quadrant photodiode, which tells the small shift of the light spot by the differential photovoltage from the top and bottom diode.

$$F(\omega) = -\frac{CV(\omega)\sigma}{\epsilon_0} \tag{2.6}$$

where C is the tip-sample capacitance and σ is the net surface charge; capacitive force [90]:

$$F(2\omega) = -\frac{\partial C}{2\partial z}V(\omega)^2 \tag{2.7}$$

and electrostriction [87]:

$$A(2\omega) = Q_{\text{eff}}V(\omega)^2 \tag{2.8}$$

where Q_{eff} is the electrostriction coefficient. In atmosphere, water can condense near the tip-sample interface and introduce complex electrochemical force [91]. For conductive samples, thermal expansion from Joule heating may emerge [92]:

$$A(2\omega) = \beta\frac{V(\omega)^2}{2R} \tag{2.9}$$

where β is proportional to the thermal expansion coefficient α and also related to the sample's geometry. Lastly, there is Peltier effect if we are measuring semiconductors:

$$A(\omega) = \frac{\alpha r_0 SV(\omega)}{T\kappa_{\text{eff}}\rho_{\text{eff}}} \tag{2.10}$$

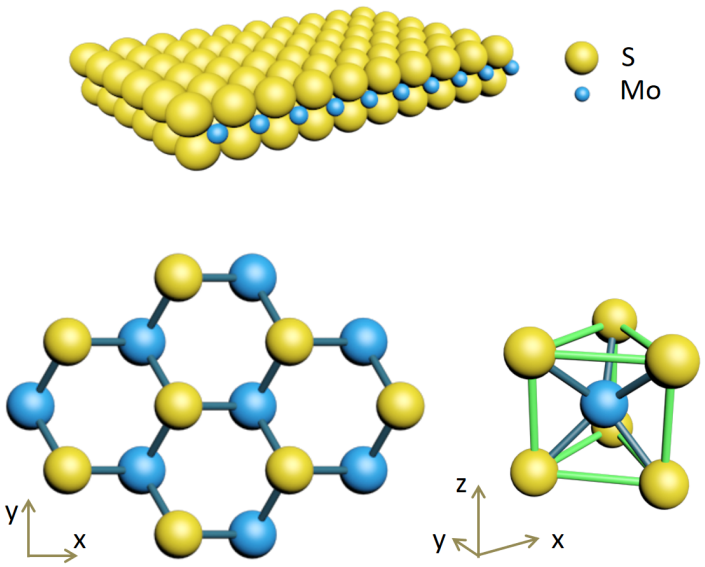

Figure 2.4: A single layer of MoS_2 consists of S–Mo–S stacking with a total thickness of 0.6 nm, with the Mo atom centred in the trigonal prism (bottom left). Viewing from the top (bottom right), each unit cell (denoted by the yellow shadow) consists of two S atoms occupying the same site in the hexagonal lattice, with the Mo atom residing in the opposite site, therefore breaking inversion symmetry in the x–y plane but preserving mirror symmetry in the z direction.

where r_0 is a coefficient with the unit of length that represents the locality of the contact, S the Seebeck coefficient, T the temperature, κ_{eff} the effective thermal conductivity and ρ_{eff} the resistivity.

To extract the piezoelectric signal, a lock-in amplifier is needed to filter the random noise and second harmonic contributions (2ω terms). To distinguish the ω terms mentioned above from piezoelectricity, well-designed control experiment is necessary and will be discussed in the procedure session.

After two decades of development, piezoresponse force microscopy has become a mature instrument to characterize traditional bulk piezoelectric and ferroelectric materials. However, it cannot be directly applied to the measurement of piezoelectricity in single-molecular-layer MoS_2, partly due to the smaller signal but more importantly due to the crystalline symmetry.

2.3 Method and experimental design

Monolayer MoS_2 has D_{3h} symmetry. The membrane has one atomic layer of Mo between two identical S layers, packed in a hexagonal lattice. Each rhombic prismatic unit cell is

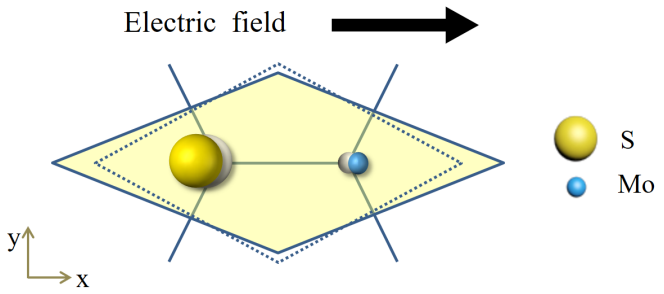

Figure 2.5: With an external electric field pointing from the S site to the Mo site, the Mo–2S dipole is stretched and the unit cell is elongated, creating compressive stress in the x direction and tensile stress in the y direction.

asymmetrically occupied by two S atoms on the left site and one Mo atom on the right, as shown in Fig. 2.4. Through group theory, all the non-zero components of the third-rank tensor d and their relationship can be identified. In fact, there is only one free parameter e_{11} [82]:

$$e_{111} = e_{11} \tag{2.11}$$
$$e_{122} = e_{12} = -e_{11} \tag{2.12}$$
$$e_{212} = e_{221} = e_{26} = -e_{11} \tag{2.13}$$

Therefore, an external electric field pointing from the S site to the Mo site in the hexagonal lattice (armchair direction, E_1) deforms the unit cell by stretching the Mo–S bond and causes internal piezoelectric stress:

$$\Delta\sigma_p = \Delta\sigma_{11} = -\Delta\sigma_{22} \tag{2.14}$$

which is proportional to the electric field:

$$\Delta\sigma_p = -e_{11}E_1 \tag{2.15}$$

All other piezoelectric components, notably the out-of-plane ones are zero. Hence typical PFM that applies out-of-plane electric field cannot effectively excite piezoelectric response in this system. Another conventional method is to measure the dipole induced by strain, as carried out in nanowires [93] and very recently in supported MoS_2 on polymer substrates [94]. However, the interaction between the two-dimensional crystal and the substrate in such flexible devices makes quantitative determination of the intrinsic piezoelectric properties challenging. The piezoelectric charge q generated by the strain from the substrate s_{11} is:

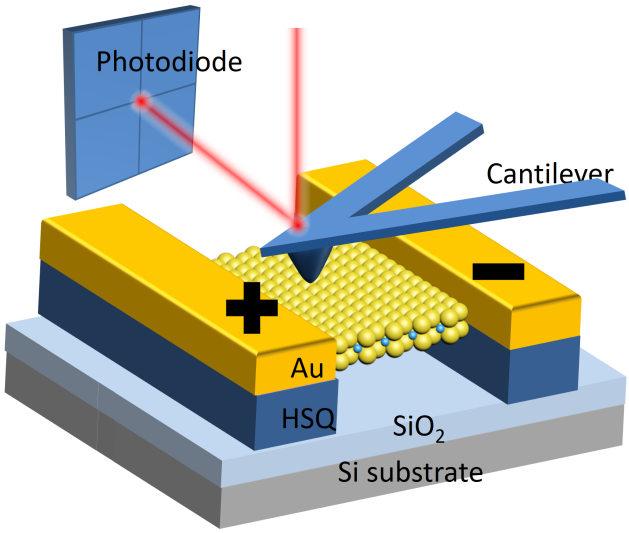

Figure 2.6: To measure the in-plane piezoelectric stress, the MoS_2 film was suspended on two HSQ posts and clamped by two Au electrodes. The film was indented with an AFM probe. The induced stress changed the load on the cantilever, which was observed by the deflection of a laser beam.

$$q = s_{11} e_{11} w \tag{2.16}$$

where w is the width of the sample. For mechanically exfoliated monolayer MoS_2, $w \sim 10$ μm and $s_{11} \sim 0.01$, so we have $q \sim 10^{-17}$ C. Such small signal can be measured with a field-effect amplifier connected in the vicinity of the device under test [95], but nevertheless is easily masked by electrostatic charge. Therefore we developed a method that combined a laterally applied electric field [96] and nanoindentation [64] in an atomic force microscope (AFM) to measure the piezoelectrically generated membrane stress (Fig. 2.6). The MoS_2 stripe was free-standing to avoid substrate effects such as doping and parasitic charges. First, to convert the in-plane stress to an out-of-plane force, the free-standing film was indented by an AFM probe and deformed. Piezoelectric stress was then induced by an in-plane electric field applied through the lateral electrodes. The extra field-induced stress changed the load on the tip and the curvature of the cantilever, which was measured via the reflection of a laser beam from the cantilever. We could then relate the internal stress to the applied electric field and quantify the piezoelectric response of monolayer MoS_2 crystal.

The asymmetric configuration of the sample was chosen for the following reasons. First, a uniform electric field could be applied by the parallel electrodes across the near-square film, simplifying the electric modeling. Second, since the stress had opposite sign in X and Y direction, their projection in the Z direction during indentation would cancel in a symmetric geometry. The asymmetry however made it difficult to deduce the mechanical response analytically, so we used numerical finite element calculation to model the indentation process.

2.4 Theoretical modeling

Theory of elastic mechanics in membrane dictates that the load-indentation curve has the form [97]:

$$F = C_1\sigma^{2D}d + C_2(\nu)Y^{2D}\frac{d^3}{L^2} \tag{2.17}$$

where C_1 and C_2 are two geometric-dependent numerical factors, σ^{2D} is the initial stress in the 2D membrane without indentation, Y^{2D} is the Young's modulus of the 2D membrane, d is the depth of indentation and L is the distance between the clamps. Here we took the Poisson's ratio $\nu = 0.25$ since the different values of ν among literature would affect the results by less than $\pm 5\%$. Thus our target is to determine the values of C_1 and C_2 by finite element calculation.

We employed two models for the finite element calculation: 2D membrane in COMSOL Multiphysics and a shell domain in Abaqus/CAE. The indentation process was then calculated by stationary solver in discrete steps. The displacement of one pair of the edges (along y-axis) was set to zero (clamped by the electrodes) while the other pair were left free. Isotropic Young's modulus and pre-stress were assigned to the membrane. In the 2D membrane model, we simply prescribed the out-of-plane displacement of a round area with a diameter of 30 nm at the center of the membrane and calculated the reaction force on the area. In the shell domain we assigned a hemisphere with a radius of 200 nm to indent at the center of the domain. Their results agreed with each other within 1% because the force is insensitive to the geometry of the contact as long as the contact region is much smaller than the size of the membrane [98].

The calculated load-indentation curve was first fit by a cubic function:

$$F = a_1 d + a_2 d^3 \tag{2.18}$$

As shown in Fig. 2.8 the indentation force agreed very well with the linear elastic theory. Then we varied the initial stress and the Young's modulus and obtained an array of fitting parameter:

$$a_1 = C_1\sigma^{2D} \tag{2.19}$$

$$a_2 = \frac{C_2}{L^2}Y^{2D} \tag{2.20}$$

Indeed we found that a_2 was independent from σ^{2D} and a_1 from Y^{2D}. Thus C_1 and C_2 could be deduced (Fig. 2.9).

Next we used the decoupling approximation to calculate the piezoelectric response [99], i.e. the electric field distribution was evaluated over the unindented sample. We also assumed the distribution of electric field in the membrane was determined by resistance rather than capacitance. In the real devices this must be validated by electric measurement discussed

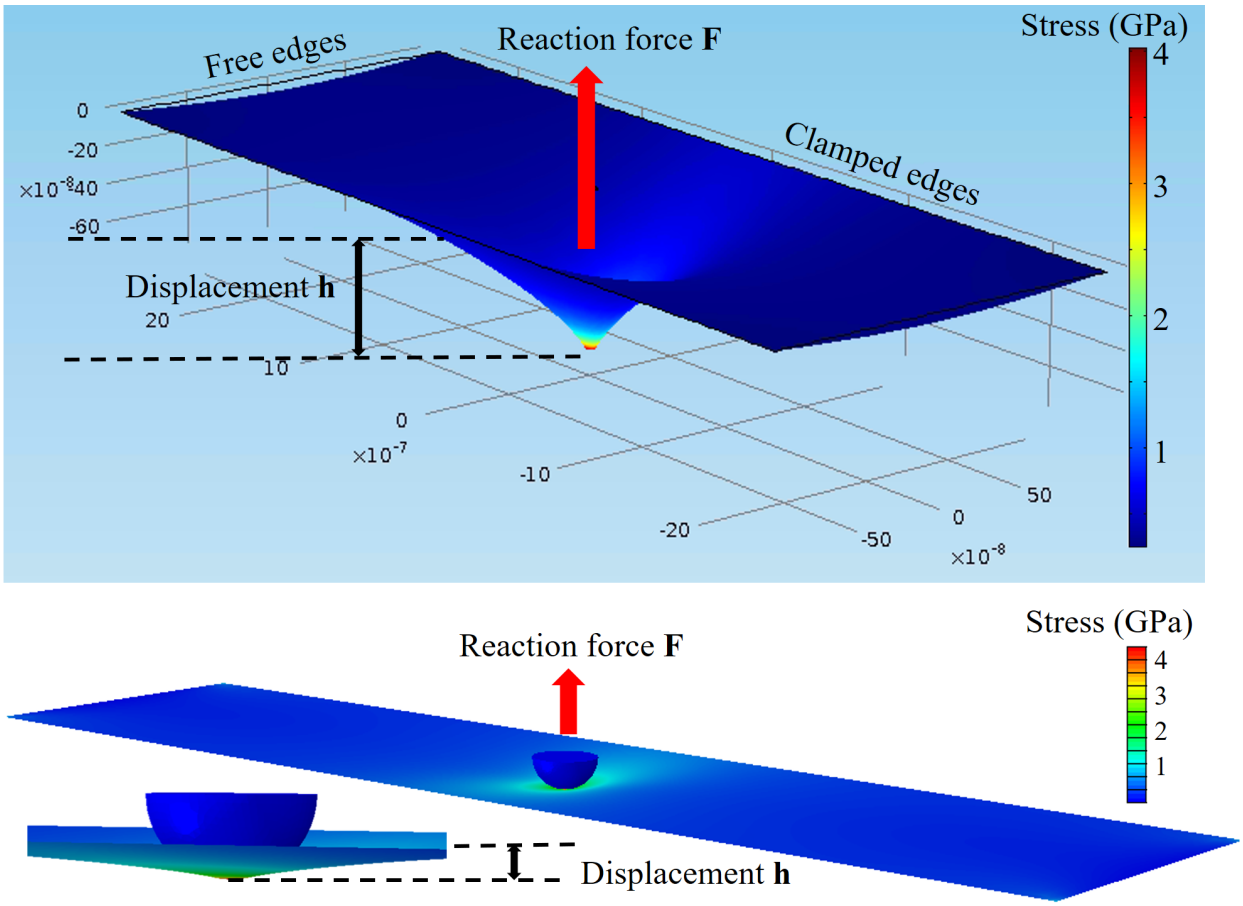

Figure 2.7: The two finite element models of the indentation process for calculating the reaction force as a function of displacement. Top: 2D membrane (displacement exaggerated). Bottom: shell domain plus hemispherical indenter.

in the next section. After that, we could conclude that the electric field is almost uniformly distributed on the rectangular membrane. Finally the piezoelectric stress was incorporated in the calculation through a uniform anisotropic change of pre-stress, which induced a load change (Fig. 2.10). The load was proportional to the anisotropic stress, as expected from small perturbation, and approximately linearly dependent on the depth of indentation:

$$\Delta F_p = C_{12} \Delta \sigma_p d \tag{2.21}$$

If the piezoelectric stress were isotropic, we would expect $C_{12} = C_1$. Yet due to the anisotropic stress and the anisotropic geometry, we found $C_{12} < C_1$ by sweeping the piezoelectric stress (Fig. 2.11).

The values of these coefficients were derived from the simulation results of 6-by-2-µm membrane, which was our average sample geometry. We also confirmed that the numerical

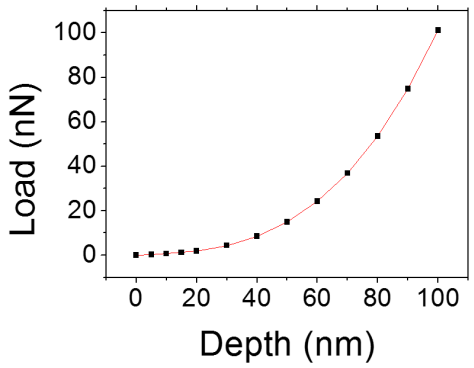

Figure 2.8: Calculated force curve of a clamped membrane during indentation.

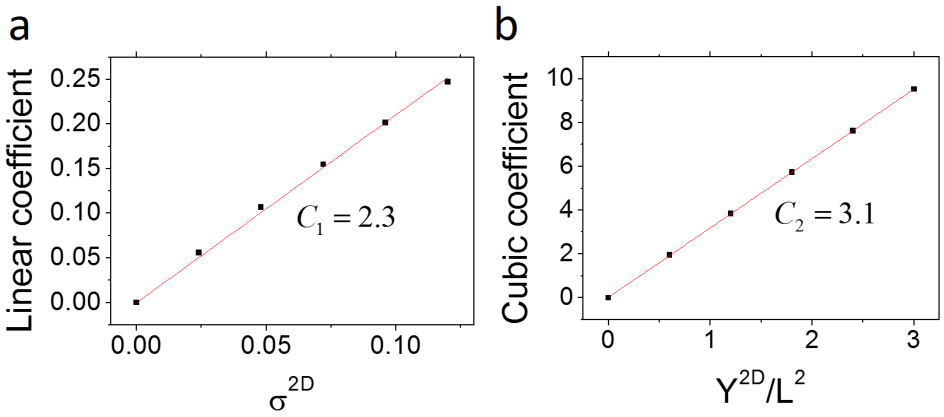

Figure 2.9: The calculated C_1 and C_2 coefficient in the nano-indentation model (Eq. 2.17).

coefficients C_1, C_2 and C_{12} are not sensitive to the aspect ratio of the film or the shape of the free edges, as long as the width is much larger than the distance between clamps (Fig. 2.12). This is because the load is concentrated near the middle of the clamped edge (Fig. 2.7).

2.5 Device fabrication

Our MoS_2 flakes were obtained by exfoliating natural 2H crystals (SPI Supplies) on polymer stacking, which consisted of 270-nm-thick poly-methyl-methacrylate (PMMA, 950K in anisole from Microchem), 50 nm water-soluble polymer (aquaSAVE®from Mitsubishi Rayon America INC.) and another PMMA layer on top of silicon substrate. The top PMMA

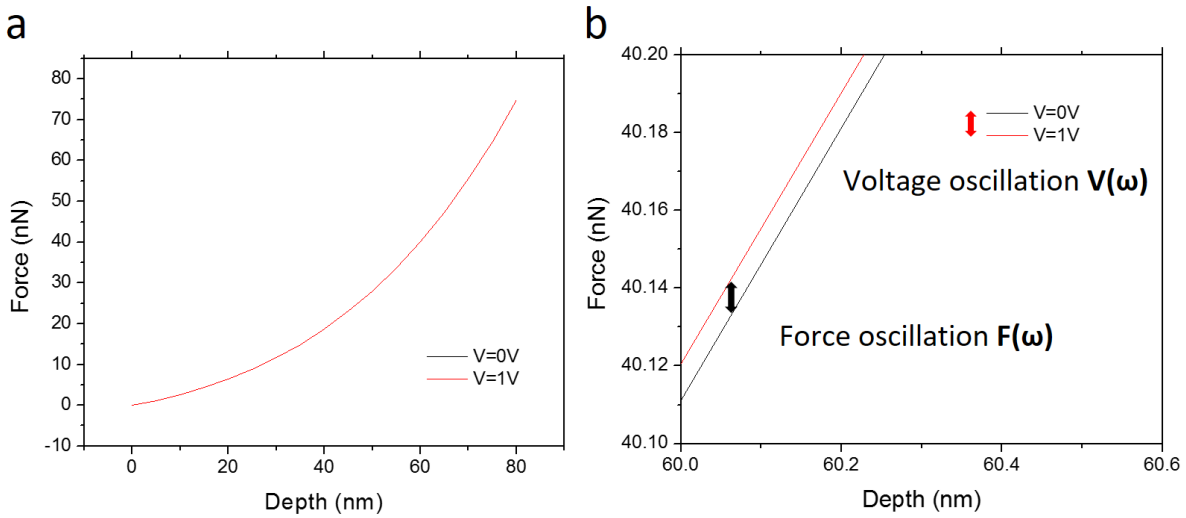

Figure 2.10: (a) Piezoelectric stress induced a load change much smaller than the static load. (b) The change was observed by differential lock-in measurement.

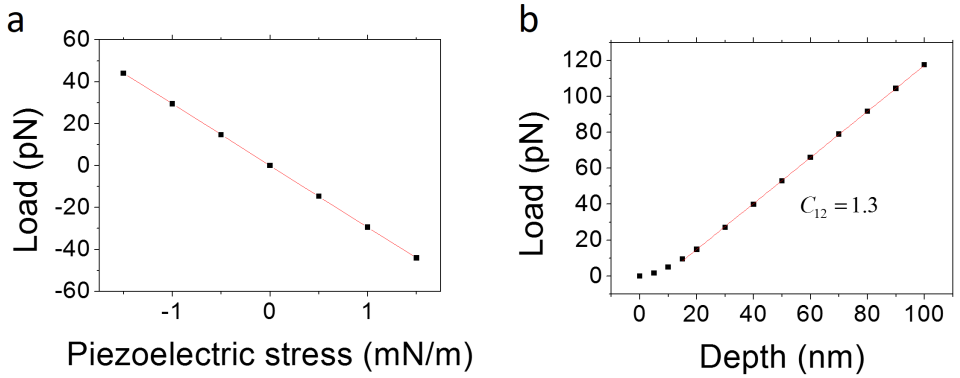

Figure 2.11: Determination of the numerical factor of the piezoelectric response. (a) The change of load was proportional to the perturbation of piezoelectric stress at finite indentation depth. (b) The change of load at fixed piezoelectric stress ($\sigma^{2D} = 1$ mN/m) increased linearly at large depth ($d > 15$ nm).

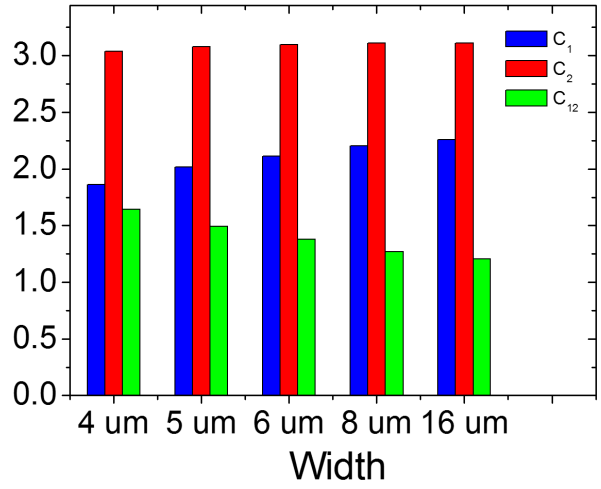

Figure 2.12: The deviation of load and piezoelectric response for our samples with different geometry (width ranging from 4μm to 16μm) were found to be smaller than 5% and 15%, respectively. In the experiment these were the primary sources of error in the calculation of Young's modulus and piezoelectric coefficient.

layer was released in water and transferred onto hydrogen silsesquioxane (450 nm FOX-15 from Dow Corning) spin-coated on silicon substrate with 270 nm thermal oxide. The thickness of flakes with 1-3 layers was inferred from Raman spectrum and photoluminescence [100, 101]. Differentiating 4-5 layers from thicker flakes was more challenging, so we also used second harmonic generation (SHG)[102] to assist the determination of layer number. To speed up the search for monolayer samples, scanning photoluminescence (PL) microscopy (Nikon Eclipse TE2000, excited at 488nm) was employed to provide both the total intensity of PL (cut off with 650nm long-pass filter) that unambiguously highlights monolayer from thicker ones (the signal of which is more than 5 times stronger than bilayers), and the intensity of reflection that gives distinctive contrast for up to 5-layer flakes.

After the monolayers of MoS_2 between the PMMA/HSQ layers were identified, the free-standing nano-electromechanical devices were designed and fabricated accordingly. To apply an electric field along the armchair direction, the electrodes were designed to be parallel to or at 60° with respect to the sharply cleaved edges which form 60° or 120° corners. The edge direction typically corresponded to the zigzag direction (Y-axis in Fig. 2.4), which was further confirmed by the polarization resolved SHG [103]. In addition, the scanning SHG map also verified that the flake (occationally 100 μm in scale) consisted of a single crystal domain. Then the designed pattern which served as supportive posts, mechanical clamping and electrical contact simultaneously (region surrounded by yellow dashed line in Fig. 2.17) was transferred to the device by one-step electron-beam lithography (2000 $\mu C/cm^2$ at 50 keV). A small projection outside the electrode was added to mark the center of the film. After exposure, crosslinked HSQ (amorphous SiO_2) formed supportive posts under

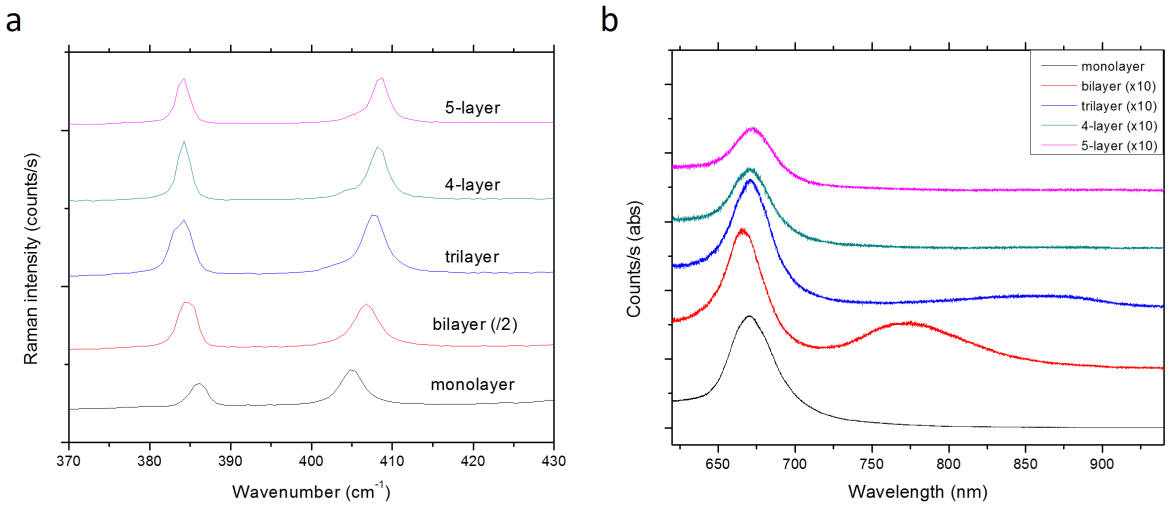

Figure 2.13: Layer-number dependence of (a) Raman and (b) photoluminescence spectrum of MoS_2. The difference is most visible for 1-3 layers. The Raman peak shift is due to increasing inter-layer coupling. The bumps in the photoluminescence in bilayer and trilayer correspond to the width of the indirect band gap.

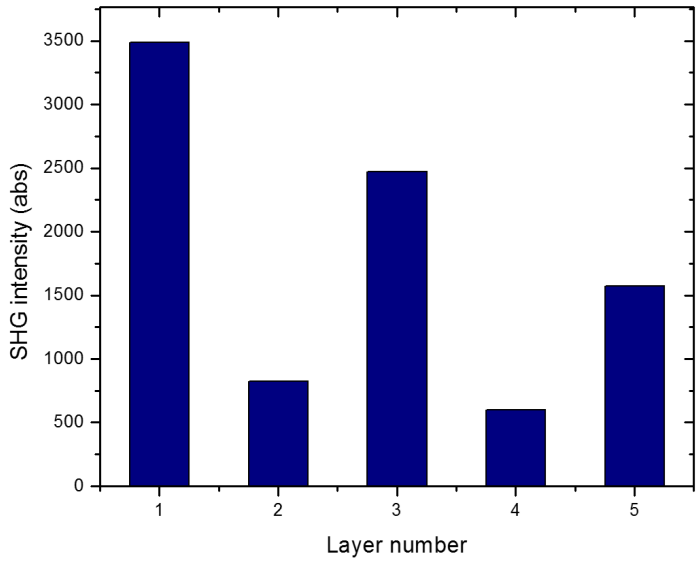

Figure 2.14: Layer-number dependence of second harmonic generation of MoS_2.

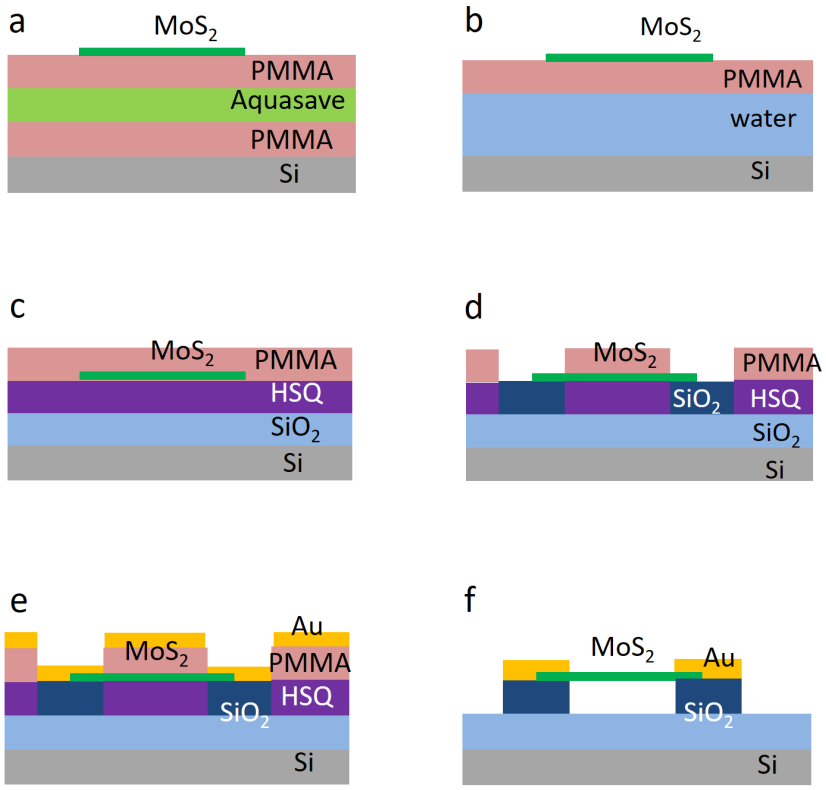

Figure 2.15: Process flow of sample fabrication. (a) MoS_2 flakes were exfoliated on top of PMMA/Aquasave/PMMA stacking. (b) PMMA layer that carried MoS_2 was released by water immersion. (c) The MoS_2/PMMA stacking was transferred onto HSQ. (d) The sample was patterned by electron beam and the PMMA was developed. (e) Metal contact was evaporated. (f) The structure was suspended after lift-off of Au and development of HSQ.

the MoS_2 membrane, and the PMMA was removed in MIBK:IPA 1:3 solution. The sample was then metalized with Cr/Ti/Au (0.5/5/90 nm). Finally, the samples were lifted off in acetone, transferred to aquatic KOH/NaCl solution (0.25 mol/L and 0.5 mol/L respectively) for thorough development of HSQ [104], and dried using critical point dryer. The fabrication preserved the quality of the film as inspected through Raman spectrum, photoluminescence and SEM.

Meanwhile, we fabricated large radius indenter to avoid concentrated stress that might harm the film's mechanical and electrical integrity. The probe was based on standard silicon nitride contact mode cantilevers with an initial spring constant of 0.5 N/m. The cantilevers was chosen as a balance between high force-sensitivity (soft cantilever) and sufficient indentation (hard cantilever). The radius of tips was increased by uniformly depositing 150 nm of

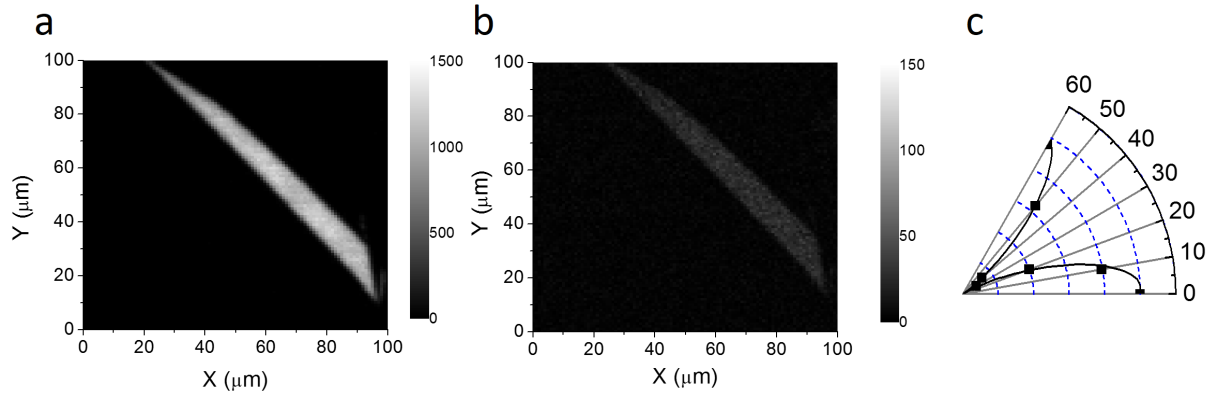

Figure 2.16: The second harmonic generation of MoS_2 is highly polarized. If the incident polarization is parallel to the Mo-S bond direction then the SHG also is polarized in this direction. (a) and (b) show the SHG intensity along and perpendicular to this direction, respectively. (c) By rotating the sample and measuring the SHG intensity polarized parallel to the incident light we also verified the bond direction (armchair, or X-axis in Fig. 2.4) with respect to the polarization.

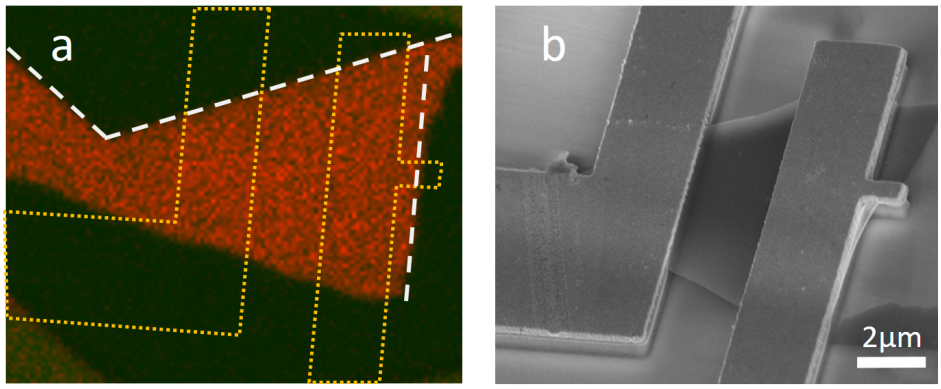

Figure 2.17: Design and imaging of the piezoelectric monolayer MoS_2 device. (a) To maximize piezoelectric coupling, electrodes (outlined with yellow dashed lines) were defined parallel to the zigzag edges (white dashed lines, verified by SHG measurements) of the exfoliated monolayer flakes identified by confocal fluorescence microscopy. The false colors of green and red denote the intensity of reflection and photoluminescence, respectively. (b) The device was imaged by SEM to confirm that free-standing MoS_2 monolayers were clamped between the Au electrodes and HSQ posts.

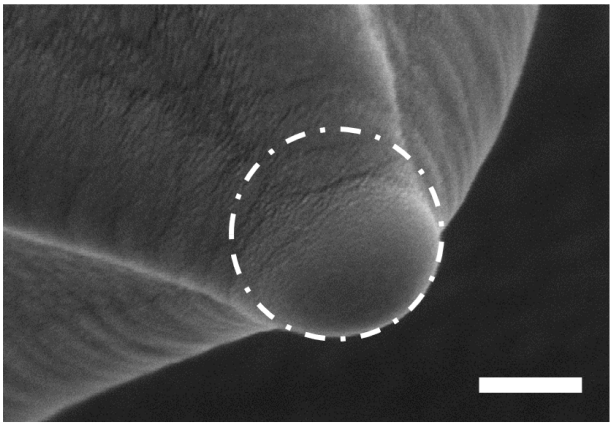

Figure 2.18: The radius of the probe after film deposition was measured by SEM. Scale bar: 200 nm.

Al_2O_3 through atomic layer deposition (ALD). Additional 20-nm palladium was evaporated over the tips with slow rate to provide conductivity. Finally the cantilevers were inspected with scanning electron microscope (SEM) and the average radius was found to be 185 nm. The spring constant of the cantilever was calibrated against a force gauge. We found that after deposition, the resonant frequency (85 kHz) was doubled due to increased stiffness of cantilever (1.0 N/m). The higher stiffness allowed the tip to work also in tapping mode.

2.6 Measurement and result

The experiment was conducted with a modified Dimension 3100 scanning probe microscope. Samples were first wire-bonded (dual in-line ceramic package, DIP24) and mounted in a socket fixed on the sample stage. The socket was wired to voltage sources according to Fig. 2.20. The alternating voltage on the two electrodes drove the piezoelectric response. The net electromechanical interaction contained three terms, piezoelectricity from the film, electrostatic force between the film and the substrate, and electrostatic force between the cantilever and the substrate:

$$\Delta F = V_{ac}(-1.3e_{11}\frac{d}{L} + \frac{C_{fs}}{\epsilon_0}(V_f - V_s) + \frac{C_{cs}}{\epsilon_0}(V_t - V_s)) \tag{2.22}$$

where V_{ac} is the difference of voltage between the electrodes; C_{fs} and C_{cs} are the film-substrate and cantilever-substrate capacitance; V_f, V_s and V_t are the electrochemical potential of the film, substrate and tip/cantilever. To eliminate the contribution from the last two terms, the substrate and the tip were biased so that $V_f = V_t = V_s$. The ac voltage on the two electrodes was set to have opposite sign so that V_f remained constant on average.

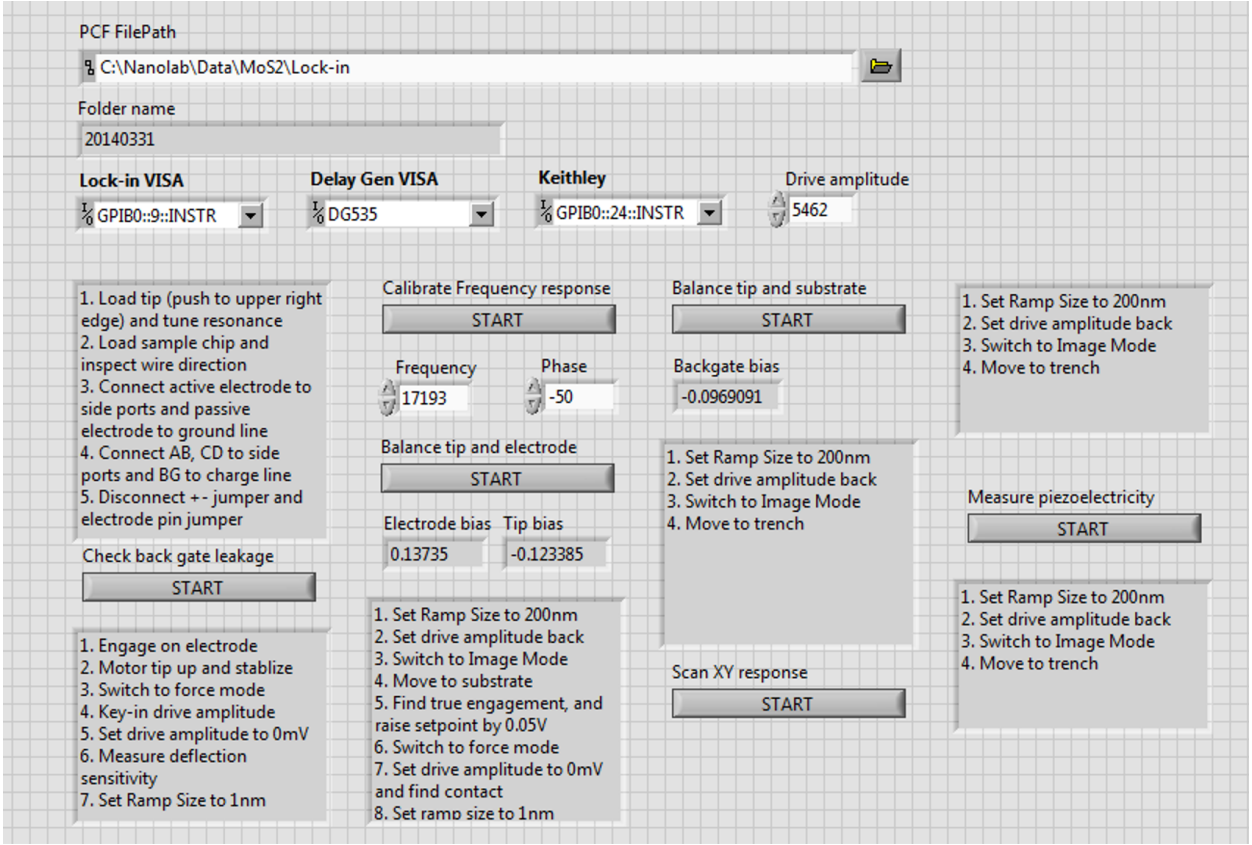

Figure 2.19: The automated data acquisition and proper operation procedure were integrated in a Labview interface.

Electrical characterization was conducted to verify that the response time to reach electrical steady state was fast enough such that the piezoelectric coupling was approximately quasi-static:

$$\tau = RC = \frac{RS\epsilon_0}{h + t_{\mathrm{SiO_2}}/\epsilon_r} \tag{2.23}$$

where S is the area of the suspended film, h is the height of the air gap and $t_{\mathrm{SiO_2}}$ is the thickness of oxide layer. The oxide layer was necessary because crosslinked HSQ had poor mechanical and electrical strength and could not provide enough insulation during wirebonding. The dark resistance of the device was usually ~ 10 GΩ. The low conductivity meant that the suspended film in ambient condition was nearly intrinsic, mainly because surface adsorption of molecules (oxygen and water) trapped the n-type carriers. Therefore $\tau \sim 1$ μs whereas the period of voltage oscillation was ~ 100 μs, and the quasi-static assumption was valid. We found that even weak illumination boosted conductivity by an order of magnitude due to the photocarriers and molecule desorption. Also the Cr layer in the electrode was

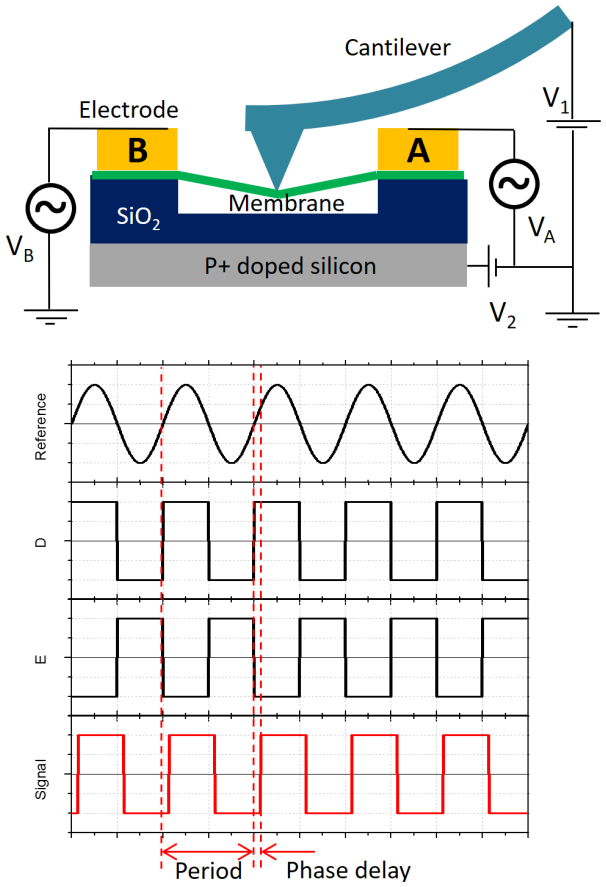

Figure 2.20: Square wave was applied to the electrodes as the source of electromechanical modulation. The reference signal was generated by the internal oscillator of lock-in amplifier (SR830) and fed into delay generator (DG535) that provided two out-of-phase square waves with tunable amplitude. DC biases were applied to the tip and the substrate to balance the electrostatic forces. The expected piezoelectric signal should also be a square wave with zero phase delay.

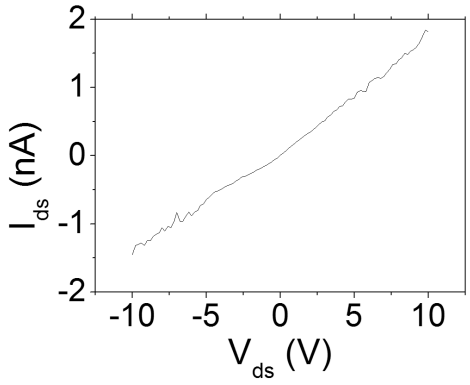

Figure 2.21: IV characterization of the free-standing MoS_2 device.

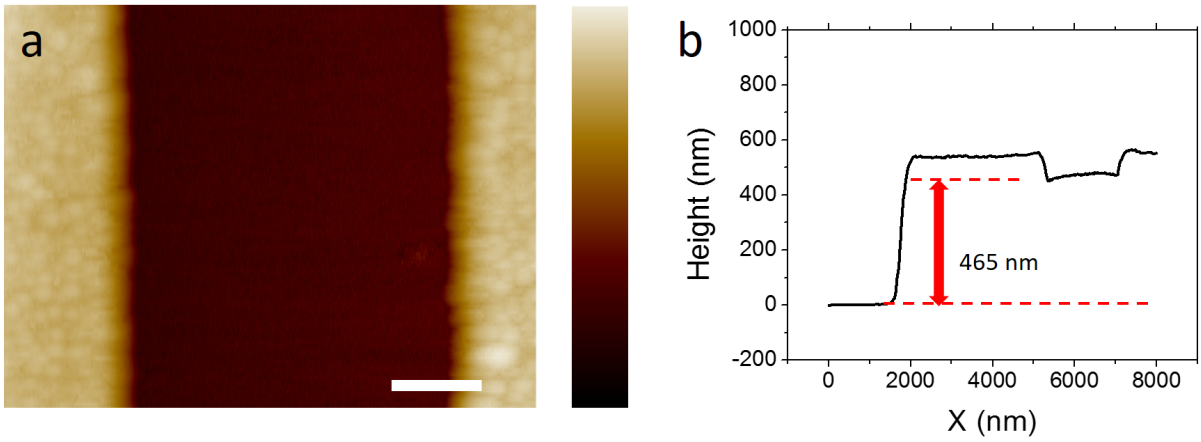

Figure 2.22: (a) Non-contact AFM image of free-standing MoS_2 device. Scale bar: 500 nm. (b) The cross section of the height profile shows a sufficient clearance for indentation.

critical to the contact quality.

Next we inspected the membrane by non-contact AFM. To avoid any thermal drift the system was stabilized overnight. Successfully suspended films usually had pre-stress and yielded clean height profile similar to flat substrate. On the contrary, broken or loose films adhered to the tip and dampened its oscillation amplitude, such that no height profile could be obtained.

Before measurement, the parameters of the tip such as the static deflection sensitivity S_d (which would be converted to force sensitivity S_F with the spring constant of the cantilever) and frequency response were acquired. We kept the piezoelectric driving frequency much below the resonance so that the mechanical response was quasi-static. Due to the electronics of our AFM setup (a nominal 19 kHz low-pass filter) the amplitude and phase read-outs

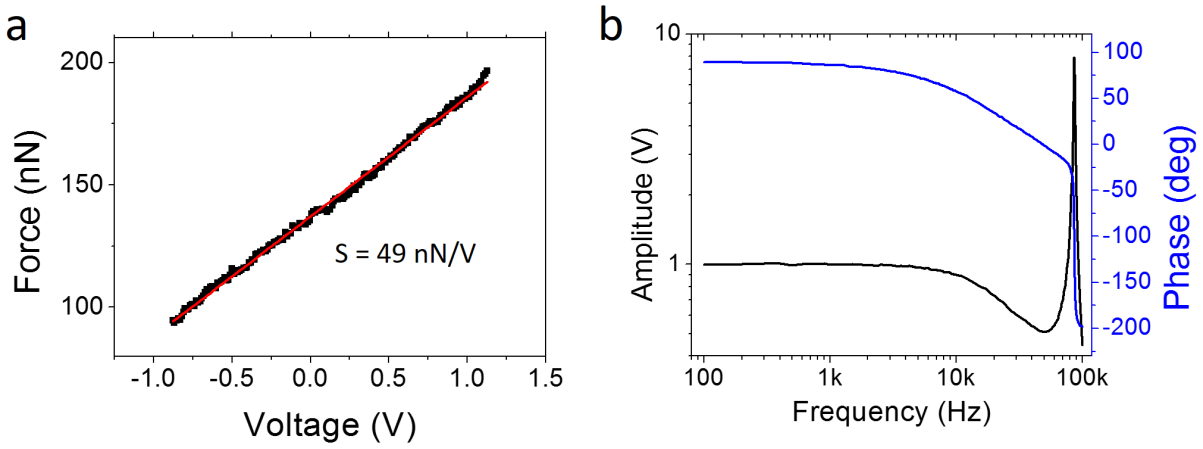

Figure 2.23: (a) Force sensitivity and (b) frequency response of the probe.

must be adjusted to recover the raw data. At our operating frequency $\sim$ 10 kHz, the real amplitude was 15% higher than the direct read-out and the real phase was 30° in advance.

The proper bias was found by measuring the tip-sample and tip-substrate electrostatic force. We applied V_{ac} to the sample, moved the tip over the sample (typical distance is 100-300 nm), and recorded the first and second harmonic of the tip oscillation as functions of the tip bias. When the electrochemical potential was balanced ($V_t = V_f$), the first harmonic signal should be zero. The second harmonic signal was also minimized because any extra charge would induce an attractive force between the tip and sample, reduce their distance and increase the capacitive force. Similarly the potential of the tip and substrate was also balanced ($V_t = V_s$). We assumed that under these conditions there would be minimal film-substrate electrostatic force as well ($V_s = V_f$).

Finally indentation was performed at the center of the sample. The raw data were all acquired through the analog-digital converters of the Nanoscope controller and consisted of three variables, z the travel distance of the base of the cantilever (in nm), D the deflection signal (in Volt) and I the lock-in signal (in Volt). They were related to the target observables by:

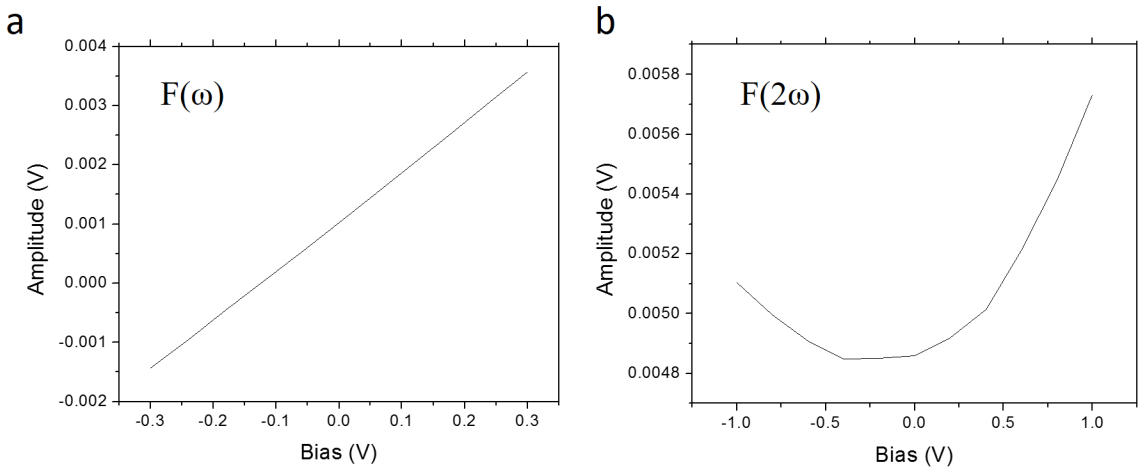

Figure 2.24: (a) First-order and (b) second-order oscillation amplitude of the tip deflection in response to the driving AC voltage across the device as a function of tip bias. The tip was not in contact with the sample so the signal was purely coming from electrostatic force.

$$F_t = S_F D = 2.3\sigma^{2D} d + 3.1 Y^{2D} \frac{d^3}{L^2} \tag{2.24}$$

$$\Delta F_t = S_F S_I I \tag{2.25}$$

$$d = z - S_d D \tag{2.26}$$

$$k_f = \frac{\partial F}{\partial d} = 2.3\sigma^{2D} + 9.3 Y^{2D} \frac{d^2}{L^2} \tag{2.27}$$

$$\Delta F_p = 1.3 \frac{\Delta\sigma_p V_{ac}}{L} = (k_f S_d + S_F) S_I I \tag{2.28}$$

where F_t is the reaction force, S_I the lock-in amplifier's sensitivity and k_f the effective spring constant of the film. The reason k_f appears in the equation is that the piezoelectric stress is calculated with the zero-displacement assumption. In reality, the film and the tip oscillated together during the measurement and part of the stress was relaxed within the film.

The force as a function of indentation depth was first calculated from $D(z)$ with Eq. 2.26. By fitting $F_t(d)$ with Eq. 2.24 (Fig. 2.25(a)) we obtained $Y^{2D} = (1.2 \pm 0.1) \times 10^2$ N/m and $\sigma^{2D} = 45 \pm 5$ mN/m, which agreed well with previous *ab initio* calculations and experimental results [82, 105]. The repeatable load–indentation curves demonstrated the quality of the atomic crystalline film and the effectiveness of the clamp. At a fixed driving voltage (V_{ac} = 1V), the piezoelectric stress $\Delta\sigma_p = 0.12 \pm 0.02$ mN/m was calculated from the function $I(z)$. A positive sign was assigned because the signal and the driving voltage were in phase. Consequently $e = -(2.9 \pm 0.5) \times 10^{-10}$ C/m, meaning the film experienced a tensile strain

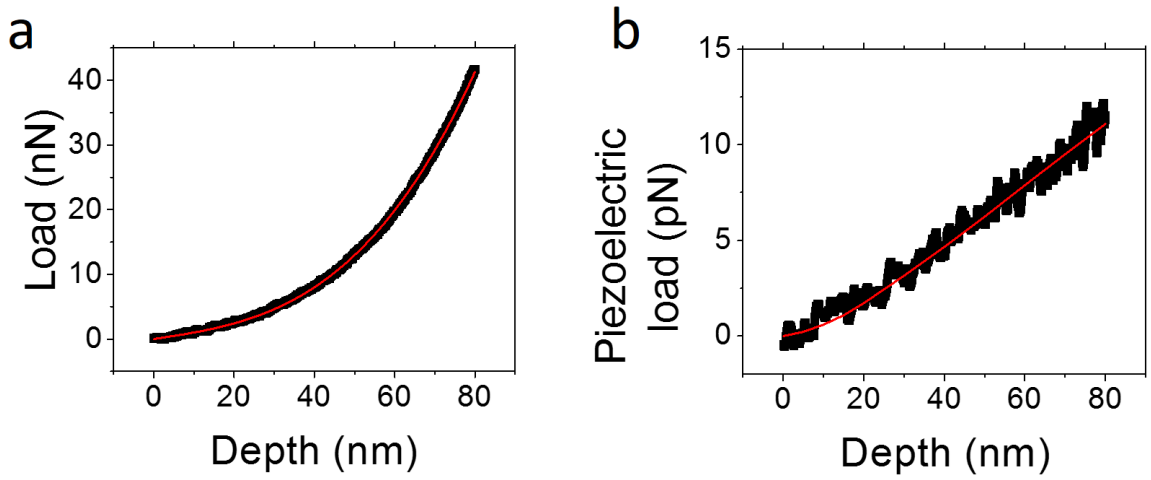

Figure 2.25: (a) The indentation curve and (b) piezoelectric response of the MoS_2 device. Black markers are experimental data and red line denotes the theoretical fitting.

when a positive voltage drop was applied. When normalized to the thickness, this measured piezoelectric coefficient is comparable to the bulk values of standard piezoelectric crystals such as ZnO or AlN.

2.7 Layer and angular dependence

According to DFT calculation we have $e_{11} > 0$. Therefore the minus sign of e indicated the electric field was pointing to the Mo→S direction. In general, when crystal rotates by an angle θ with respect to the electric field, the piezoelectric stress in the original coordinate system is transformed accordingly:

$$\begin{pmatrix} \Delta\sigma_{11} & \Delta\sigma_{12} \\ \Delta\sigma_{21} & \Delta\sigma_{22} \end{pmatrix} = -e_{11}E_1 \begin{pmatrix} \cos 3\theta & -\sin 3\theta \\ -\sin 3\theta & -\cos 3\theta \end{pmatrix} \tag{2.29}$$

where θ is the crystal's azimuthal angle between the mirror plane containing the axis of rotation in the crystal structure (X-axis in Fig. 2.4) and the direction of the electric field. Although the shear force terms become non-zero, they have no contribution to the load of the tip because of the mirror symmetry of the device: after reflection transformation the shear stress reverses sign, while the reaction force on the tip in Z direction should not change sign. In the same way we found the reaction force on the tip in X and Y direction must be zero from all the stress components. We verified this by simulating the piezoelectric force as a function of angle at fixed depth. The result reflected the 3-fold symmetry of the crystal and was related to the experimental observable:

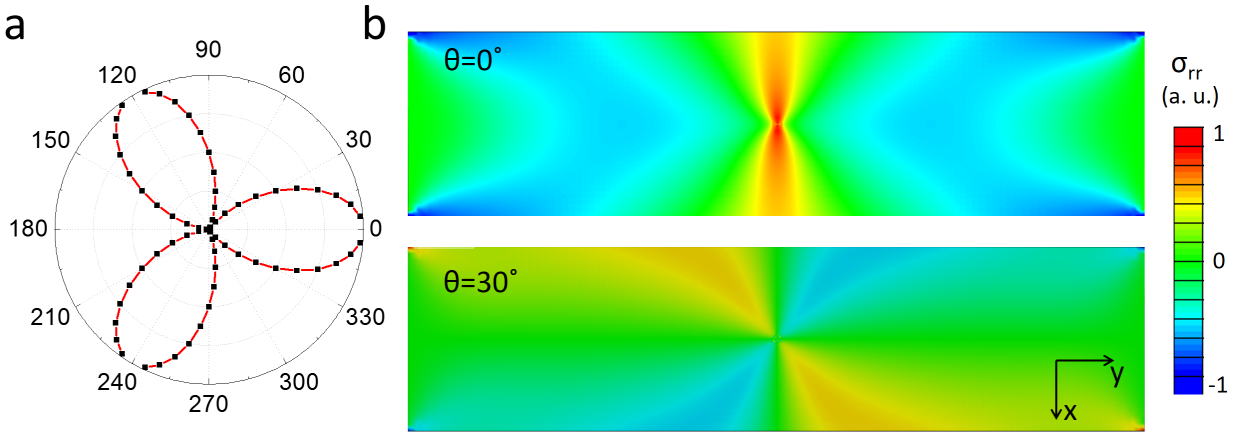

Figure 2.26: (a) The calculated angular dependence of piezoelectric force during indentation. Amplitude ranges from -1 to +1. (b) The distribution of radial piezoelectric stress of the MoS_2 film for different crystalline orientation.

$$-\frac{\Delta\sigma_p}{E} = e = e_{11}\cos(3\theta) \tag{2.30}$$

As a result, the anisotropy of piezoelectricity in monolayer MoS_2 offers a mesoscopic way to unambiguously determine its crystalline orientation in ambient, and distinguish a crystal from its inverse structure once the sign of e_{11} is given. Previously, this was only achieved in ultrahigh-vacuum (UHV) environment using atomic imaging tools [106, 107]. In principle one could experimentally verify the sign of e_{11} by comparing the piezoelectric results and atomic image of the same device, yet currently it is challenging to transfer the fabricated devices to be inspected by transmission electron microscopy.

We fabricated a series of devices based on the same single-crystal flake to study the angular dependence, with θ ranging from 0° to 60° (Fig. 2.27). The effective piezoelectric coupling coefficients of these devices fit well to a cosine curve (red solid line) with a period of 120° and an angular error of less than 2°, in accordance with the crystalline orientation inferred from SHG. The change of sign from the upper devices to the lower ones allowed us to draw the atomic orientation of the two-dimensional crystal.

In addition, we also studied the thickness dependence of the piezoelectric coefficient of two-dimensional membranes exfoliated from natural 2H-MoS_2 crystals. We observed a piezoelectric response only for odd-layer membranes due to inversion symmetry breaking (Fig. 2.28). For even-layer membranes, the contributions to piezoelectricity from alternating orientations of adjacent layers cancelled. Such results in two-dimensional crystals mark the distinctive thickness dependence of the piezoelectric coefficient from the linear scaling of conventional piezoelectric materials. The strain-gradient induced piezoelectric coupling ("flexoelectricity") was estimated to generate ~ 0.1 pN force, more than one order of mag-

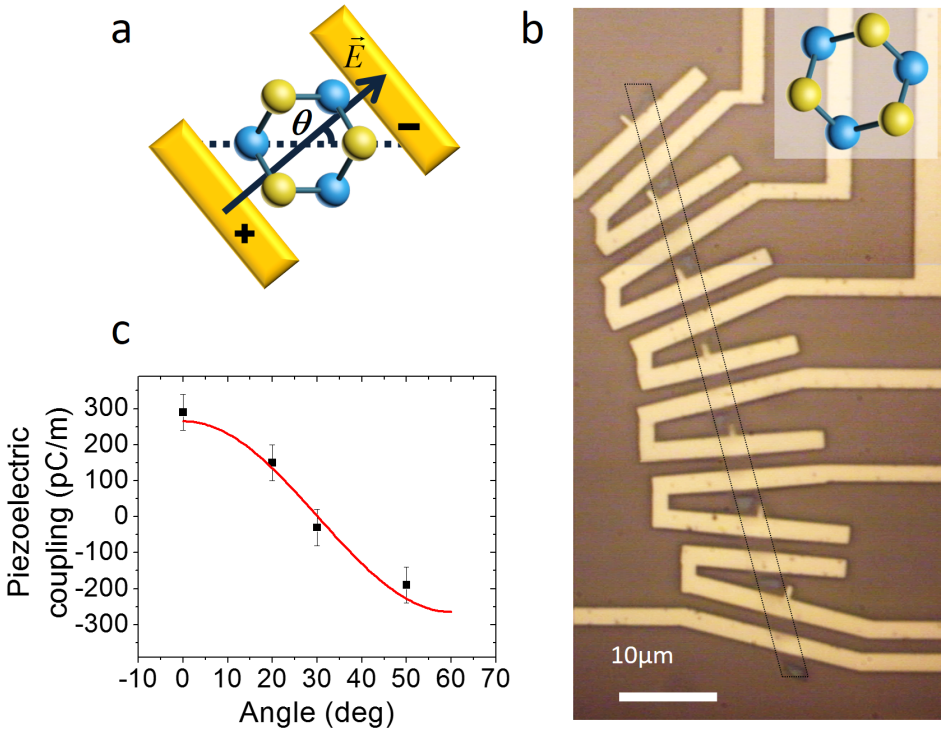

Figure 2.27: Experimental angular dependence of the piezoelectric response in monolayer MoS_2. (a) The rotation of the crystal with respect to the electric field and mechanical boundary was achieved by patterning the electrodes at different angles θ. (b) Optical image of multiple electrode pairs integrated on a long stripe of MoS_2 (dashed outline) rotated by 10° at each section. The relative rotation between the first and last device wass 60°, so the piezoelectric effect should reverse sign as the alignment of the electric field to the Mo–2S dipole changed from parallel to antiparallel. Scale bar, 10 μm. (c) Measured piezoelectric coupling strength (square data points) followed the $\cos(3\theta)$ dependence (the red fitting curve) predicted from the crystalline three-fold symmetry. The sign change was observed from the phase readout of the piezoelectric signal through a lock-in amplifier. This distinguished our low-frequency electric method from SHG (which typically only gives amplitude information), enabling the crystalline orientation (as shown in the inset of B) to be uniquely determined without resorting to atomic images. Error bar was estimated from the noise level of the force measurement and variations in the device geometry.

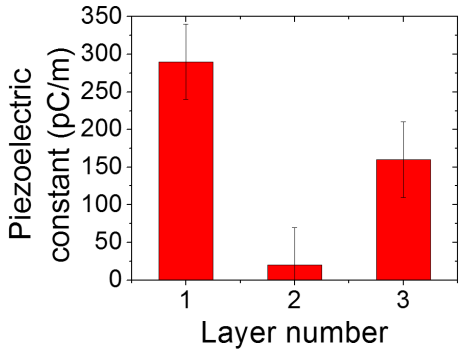

Figure 2.28: Measured piezoelectric coefficient in one-, two- and three-layer MoS_2 membranes, showing that only odd numbers of layers exhibit a significant coupling strength due to their broken inversion symmetry.

nitude lower than the force from piezoelectricity [108], as the curvature of the indented membrane in our experiment was small. Common sources of error for AFM measurements such as the hysteresis of the piezo tube and tip degradation were constantly monitored. The angular and layer dependence of the electromechanical response of the devices also provided independent evidence that the signal in our measurement originated from the piezoelectricity of MoS_2.

2.8 Conclusion

In conclusion, we successfully observed the molecular piezoelectricity in free-standing monolayer MoS_2 crystals. In contrast to bulk piezoelectric materials, we showed that such two-dimensional piezoelectricity only exists when there are an odd number of layers due to inversion symmetry breaking. We found that the angular dependence of piezoelectricity provides a mesoscopic method to probe the absolute orientation of two-dimensional crystals, which is crucial for valleytronic devices and edge engineering. As flexural rigidity scales inversely with device thickness, two-dimensional piezoelectric materials could greatly enhance mechanical displacement and therefore sensitivity. With the reduction in size, weight and energy consumption, devices based on two-dimensional piezoelectric materials will potentially revolutionize ultrasensitive sensors, nanoscale electromechanical systems and low-power electronics [109].

Chapter 3

Out-of-plane piezoelectricity in molybdenum sulfide selenide

In the previous chapter we demonstrated the measurement of in-plane piezoelectricity in single-molecular-layer MoS_2, whose symmetry constrains the number of independent piezoelectric coefficients to one and greatly simplified the measurement. In traditional microelectromechanical systems (MEMS), however, it is often desirable to have out-of-plane coupling, because larger electric field can be applied across the smallest dimension of the film. Almost all layered compounds have mirror symmetry along z-axis, with very few exceptions (like BiTeI [110]). This is because Tasker type III instability forbids the formation of out-of-plane polar surface with conventional ionic materials [111], and forces the reconstruction of many traditional polar crystals such as ZnO into out-of-plane non-polar configuration at two-dimensional limit [112, 113] Even with those covalent crystals that do not reconstruct, successful isolation of a single-layer crystalline material with broken vertical symmetry has never been reported largely due to the presence of vertical electric dipole that provides strong interlayer Coulomb binding. Therefore the other logical approach is to break the symmetry after obtaining the single layer crystal, such as single-sided chemical functionalization demonstrated in graphene [114]. The process unfortunately destroyed the lattice periodicity of graphene and cannot be used in any electronic device, the material's most promising application. Very recently, a novel strategy to synthesize asymmetric MoSSe monolayer was reported [68], by replacing top-layer S atoms of MoS_2 with Se atoms. The term "Janus monolayer" was used to describe such structure because of the chemically distinctive two surfaces. Such an asymmetric TMD monolayer is not available in nature and provides unique opportunity to realize the thinnest piezoelectric material with intrinsic out-of-plane electromechanical coupling. The monolayer remains crystalline and has intrinsic Rashba spin splitting [115–117], as well as unique biphasic surface characters for asymmetric catalytical reactions [118, 119]. In this chapter we used piezoelectric response to verify its polarity and provide insight into potential applications.

The as-synthesized MoSSe belongs to space group *P3m1*, i.e. with three-fold symmetry and a mirror plane perpendicular to the rotation axis (Fig. 3.1). Thus the piezoelectric

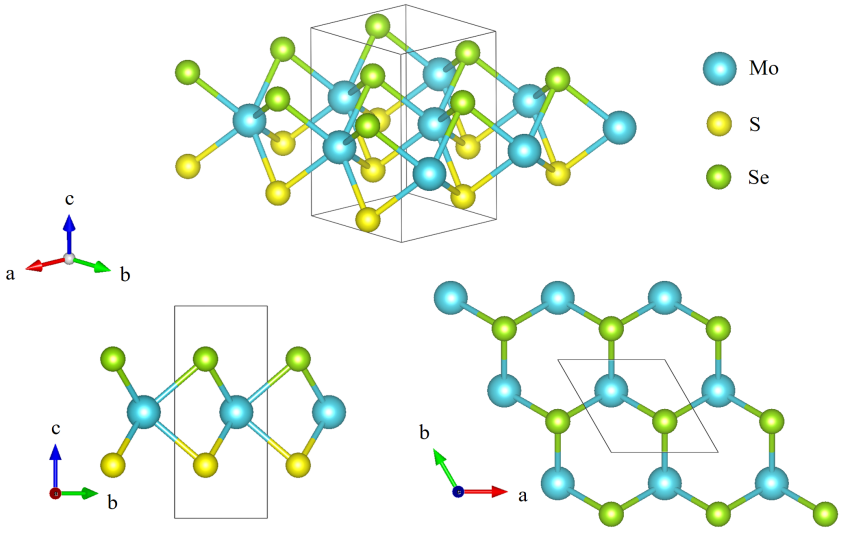

Figure 3.1: Crystalline structure of asymmetric MoSSe.

tensor is [120]:

$$d_{ij} = \begin{pmatrix} d_{11} & 0 & d_{13} \\ -d_{11} & 0 & d_{13} \\ 0 & 0 & d_{33} \\ 0 & d_{51} & 0 \\ d_{51} & 0 & 0 \\ 0 & -2d_{11} & 0 \end{pmatrix} \tag{3.1}$$

Compared with MoS_2, there are more independent coefficients, notably d_{13} and d_{33}. Since the distortion of Mo-S and Mo-Se bonds under an electric field do not cancel, a net length change is induced by applying a vertical voltage. This intrinsic piezoelectricity of the crystal is distinctive from the possible chemically induced piezoresponse by substrate [121]. Due to the small thickness, non-zero d_{13} means small voltage across the film can create large in-plane strain, a very useful feature in tunable resonators and actuators. On the other hand, measuring the in-plane stress requires the fabrication of free-standing devices. Therefore our objective in this work was to verify the existence of d_{33}, which needed less fabrication effort. Nevertheless, measuring small strain across single molecular layer is still very challenging and requires improvement of instrumentation beyond traditional piezoresponse force microscopy.

3.1 Resonance enhanced piezoresponse force microscopy

With lock-in amplification the sensitivity of piezoresponse is high enough to detect very small electromechanical coupling (<0.1 pm/V), at the cost of increasing integration time. This however is not always affordable because of the numerous artifacts presented during the measurement. Therefore the mere amplitude of the response at a single point is usually insufficient to establish an observation. To mitigate this, traditional PFM methods always focus more on the interpretation of the contrast in scanning images. Due to drift from various sources it is unrealistic to set integration time for each point more than a few milliseconds. As a result, PFM is most commonly used to study strong piezoelectric materials (like ferroelectric perovskite oxides) with complex structure at nanoscale, instead of uniform but weak piezoelectric materials. To boost sensitivity, mechanical resonance of the cantilever was utilized, i.e. small agitation at the end of the tip drives large cantilever vibration [122, 123]:

$$A(\omega) = \frac{A_0}{\sqrt{\left(1 - \frac{\omega}{\omega_0}\right)^2 + \left(\frac{\omega}{\omega_0 Q}\right)^2}} \tag{3.2}$$

The resonance frequency ω_0 and quality factor Q are not only determined by the cantilever itself but also sensitive to the contact stiffness (Fig. 3.2). Given the typical resonance enhancement (on the order of 100), even 1% frequency drift due to sample topography or contact force difference gives large artifacts in image contrast. Therefore it is important to adjust the driving frequency accordingly to maintain the enhancement factor.

The traditional phase-locked-loop method for tracking the frequency shift in non-contact imaging is based on the fact that the phase difference between the drive signal and oscillation is most sensitive to the driving frequency on resonance:

$$\phi = \tan^{-1} \frac{\omega}{(\omega_0 - \omega)Q} \tag{3.3}$$

$$\left.\frac{\partial \phi}{\partial \omega}\right|_{\omega=\omega_0} = \frac{Q}{\omega_0} \tag{3.4}$$

However, the phase of piezoresponse depends on the polarization of the sample and cannot be used for reference. In light of this, the dual-frequency resonance-tracking (DART) method is most suitable for studying piezoresponse where both the phase and the amplitude of the signal vary point to point [125]. Instead of using phase as a feedback target ($\phi = \pi/2$), DART's feedback loop maintains the following relationship:

$$\Delta A = A(\omega + \Delta\omega) - A(\omega - \Delta\omega) \approx 0 \tag{3.5}$$

And the sensitivity of the differential amplitude to the frequency deviation is:

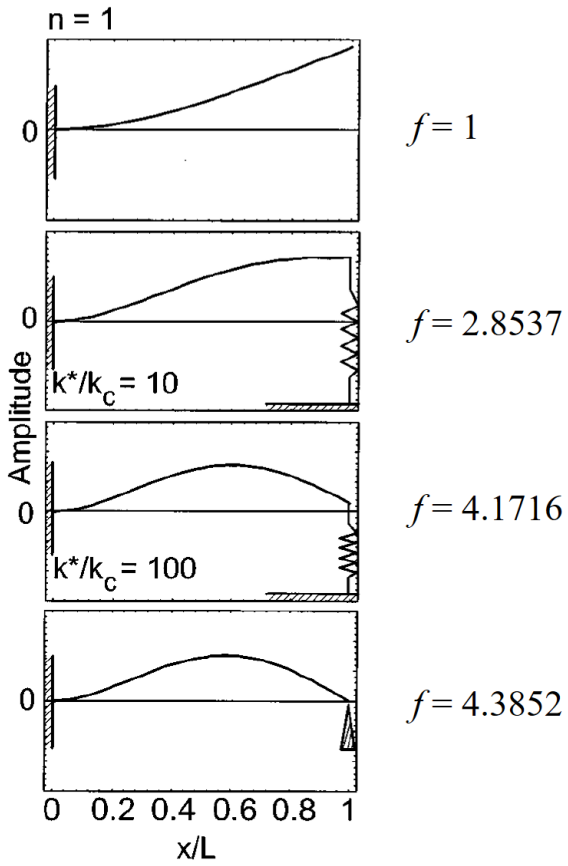

Figure 3.2: Illustration of the first resonance mode of a cantilever with various contact stiffnesses (k^*, normalized to the stiffness of the cantilever k_c). The resonant frequency f also changes accordingly (normalized to the free oscillation frequency). Reprinted with permission from [122].

$$\max\left(\left.\frac{\partial \Delta A}{\partial \omega}\right|_{\omega=\omega_0}\right) = \frac{8A_0Q^2}{3\sqrt{3}\omega_0} \tag{3.6}$$

where $\Delta\omega = \omega_0/2\sqrt{2}$ gives most sensitive tracking. In practice, stable feedback requires that the drifted frequency lies in the range $[\omega - \Delta\omega, \omega + \Delta\omega]$. Therefore larger $\Delta\omega$ enables more robust tracking.

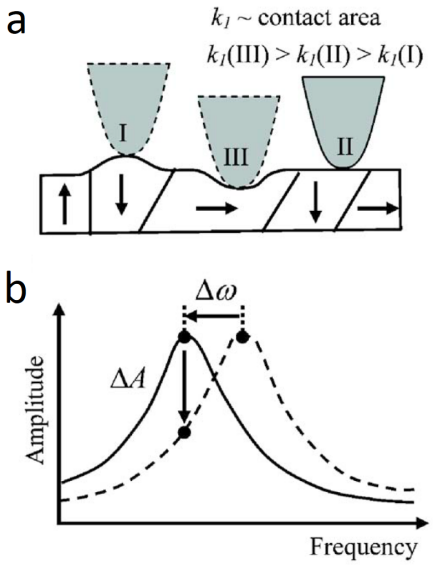

Figure 3.3: (a) The impact of surface topography on contact stiffness, which is strongly dependent on contact area and local composition. (b) Due to the high quality factor, small change in surface topography will move the cantilever out of resonance. For typical crystalline solids under normal scanning condition, the ratio k^*/k_c is on the order of 100-1000. Reprinted with permission from [124].

3.2 Experiment and analysis

Our piezoresponse measurement was performed with an atomic force microscope equipped with built-in DART piezoresponse module (MFP-3D$^{\text{TM}}$, Asylum research). The cantilevers used in the experiment had spring constants of about 2 N/m and free-air resonances at around 60 kHz. The probes were coated with Ir for electrical conductivity, at the cost of slightly reduced resolution. To minimize any substrate effect, we directly synthesized Janus MoSSe on atomically flat conductive substrates (highly oriented pyrolytic graphite, HOPG). The HOPG surface eliminated artifacts from topographical variation, and provided chemically inert surface with weak van der Waals bonding to the sample. The monolayer flake was first located by non-contact survey over large area, due to the lack of optical contrast on HOPG. The size of the flakes is usually around 1 μm.

For the measurement under contact scanning mode, we applied a smaller force ($\sim$10 nN) than typically used to reduce the scratching damage to the monolayer. As expected, the resonance enhancement at around 220 kHz boosted the sensitivity by two orders of magnitude. The apparent electromechanical response of the non-piezoelectric substrate came from the electrostatic interaction between tip and substrate, commonly observed in piezoresponse measurements of very thin films [126]. Similar to non-resonance case in the previous chapter,

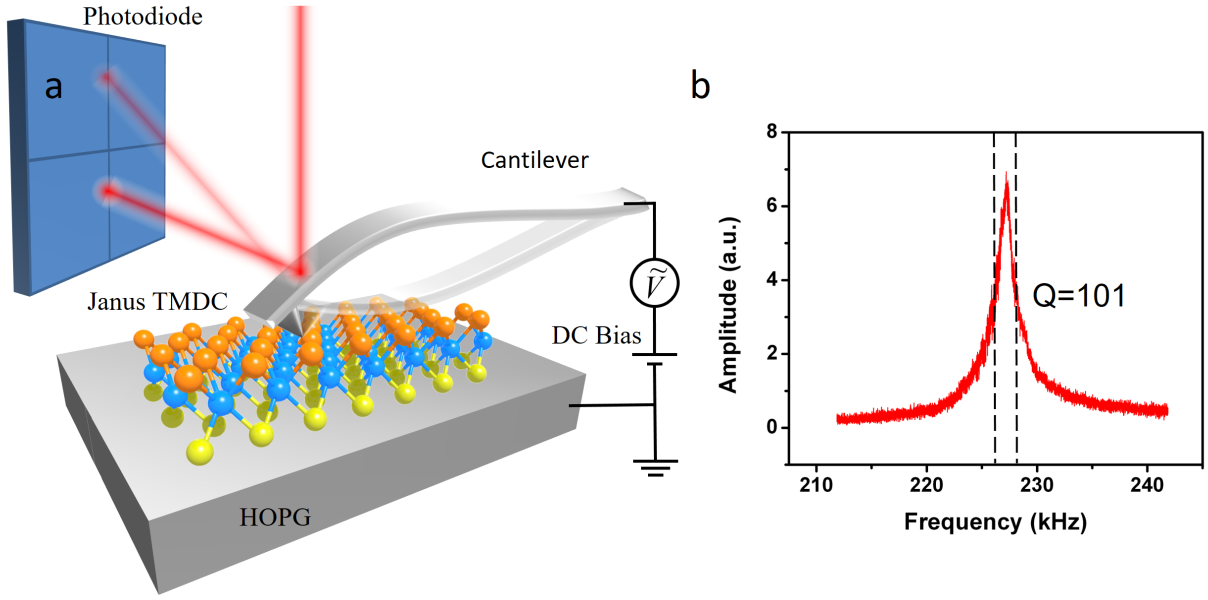

Figure 3.4: (a) Measuring piezoresponse of Janus MoSSe by resonance enhanced PFM. (b) The line width of the resonance is an indication of the quality factor and enhancement.

when the piezoresponse and the electrostatic interaction are both present, the effect of bias on the piezoelectric amplitude can be described as [90]:

$$A = \left| \frac{2\Gamma}{k_c}(V_c - V_{dc})V_{ac} + d_{33}V_{ac} \right| = \left| \frac{2\Gamma}{k_c}\left(\left(V_c + \frac{d_{33}k_c}{2\Gamma}\right) - V_{dc}\right)V_{ac} \right| \tag{3.7}$$

where Γ is the capacitive force constant, k_c the spring constant of the cantilever, V_c the contact potential, V_{dc} the bias, d_{33} the piezoelectric coefficient and V_{ac} the AC driving voltage. Therefore, the bias dependence of the oscillation amplitudes for the substrate and the sample were shifted V-shapes (Fig. 3.5). While it is difficult to quantify Γ, by setting a small bias $V_{dc} = V_c$ we can still have the standard resonant PFM signal $A_{\text{res}} = Qd_{33}V_{ac}$ [127]. Since the electrostatic force mainly came from the cantilever-substrate interaction, it was treated as a deductible constant background within our small scanning area. Besides, charging effect was also negligible due to the proximity of semiconductor and the metallic substrate [128]. During the measurement, the AC bias was limited to 1.5V to avoid electrical damage.

We observed a clear piezoelectric contrast between the Janus MoSSe monolayer and the substrate (Fig. 3.6). Sufficient signal-to-background ratio was only possible after balancing the potential of the tip and the substrate, which minimized the electrostatic effect [129]. We then compared randomized alloy monolayer, in which the chalcogenide sites are randomly occupied by S and Se atoms. The random alloy did not give visible contrast under the same measured condition. This is a strong evidence that the observed piezoelectricity came

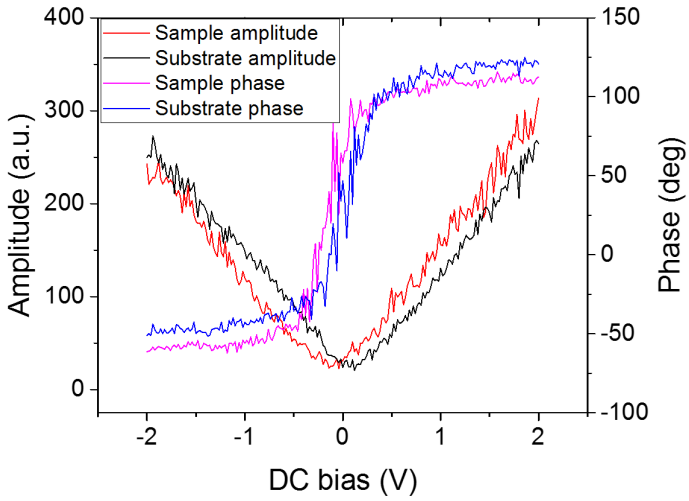

Figure 3.5: The amplitude and phase of PFM signal as a function of DC bias for the sample and the substrate.

from the broken symmetry, instead of topographic, mechanical or electrochemical artifacts. The sharpness of our PFM image is also an indication that the background electrostatic interaction did not disrupt the PFM result.

While most as-grown monolayers were topographically uniform, we obtained additional insight on those flakes carrying backfolding areas with a pair of bilayer and hole, created by thermal expansion mismatch. Since the vertical polarization of each layer is opposite in the bilayers, the total piezoelectricity of the bilayer region should be suppressed [130]. This "more is less" effect is highlighted in the parallel comparison of the cross-sections (Fig. 3.7), where a peak in height always corresponds to a dip of piezoelectric amplitude. To quantify this correlation, we calculated the correlation coefficient between resonant piezoelectric amplitude A and height of the film h using a piecewise model:

$$A = \begin{cases} Qd_{33}Vh/t, & h \leq t \\ Qd_{33}V(2t-h)/t, & h > t \end{cases} \tag{3.8}$$

where $V = 1.5$ V is the driving voltage and $t = 0.6$ nm is the thickness of the single layer. The intuitive impression is further supported by the correlation coefficient $r = 0.57$. Such strong correlation further verified that the PFM contrast was from piezoelectricity with a structural symmetry origin. From the slope we calculated an effective $d_{33} = 0.12 \pm 0.02$ pm/V. It can potentially be improved by one order of magnitude by increasing the dipolar contrast of the chemical bonds. Meanwhile, we caution that the value is qualitative since the effective piezoelectricity of semiconducting MoSSe may be sensitive to the variation of electrical properties, as the cross-section also points out some non-uniformity of piezoresponse

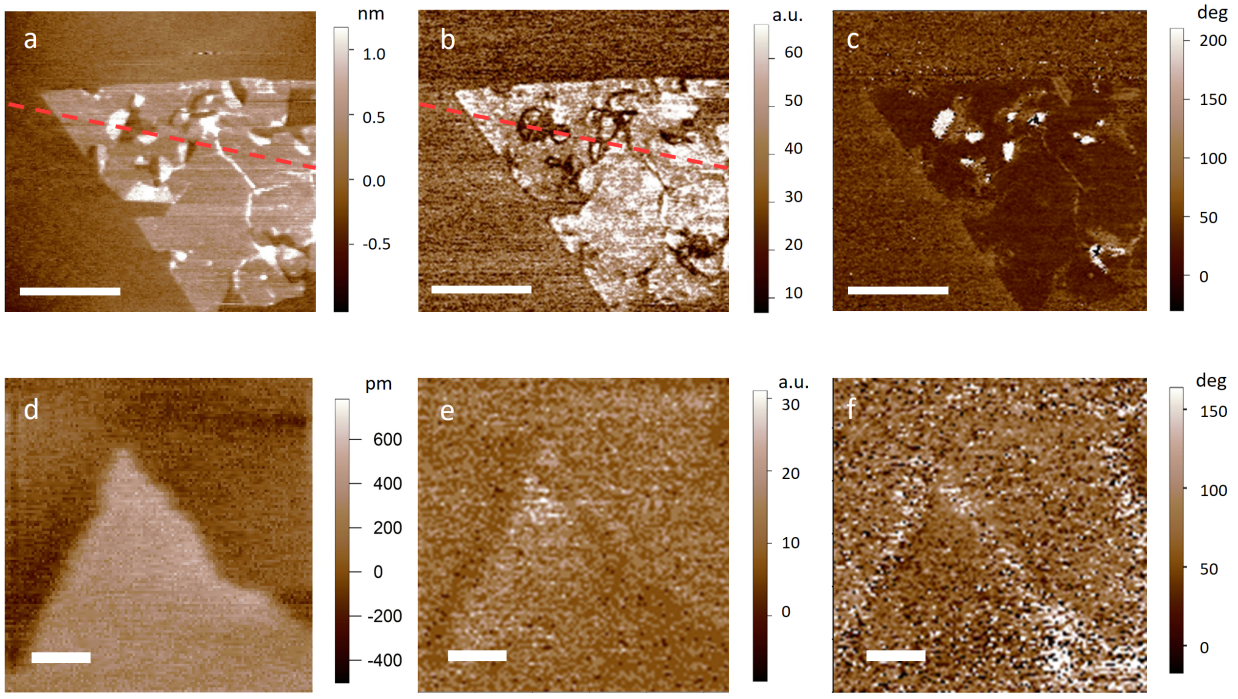

Figure 3.6: The topography (a) along with the amplitude (b) and phase (c) of the PFM signal of a Janus monolayer. The layer was uniform in most area and showed clear piezoelectric contrast, except for some broken and folded regions that gave almost the same response as the substrate. Scale bar: 500 nm. (d-f) the corresponding signal of a randomized MoSSe alloy sample. Compared with Janus MoSSe, the thickness of this monolayer was almost identical but its piezoresponse contrast from the substrate was negligible. Scale bar: 50 nm.

within the monolayer region [131].

3.3 Conclusion

The out-of-plane piezoelectricity demonstrated for the first time in 2D monolayers brings additional degree of freedom to the design and motion control of practical nanoelectromechanical devices. Due to the diverse physical properties of van der Waals layered materials, their stacking can potentially accomplish a wide range of functionalities of traditional thin-film based MEMS architecture at molecular scale.

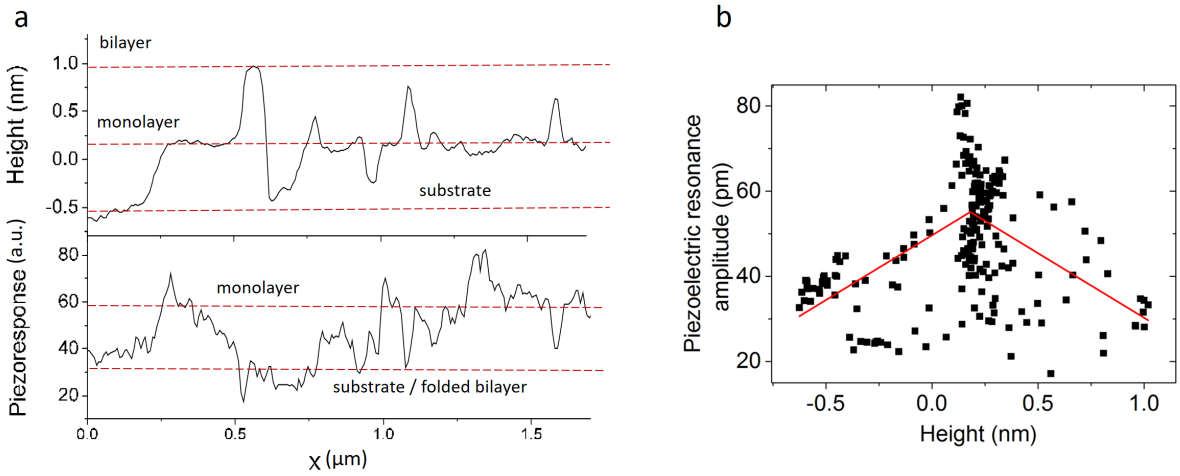

Figure 3.7: (a) The cross-section along the dashed lines in Fig. 3.6 for parallel comparison. From the height (0.7 nm per step) we identified the region of substrate, Janus monolayer and backfolded bilayer. The different piezoelectric amplitude levels of the Janus MoSSe monolayer and the substrate are also outlined. (h) The correlation plot of the height and amplitude data in (g), from which we estimated an out-of-plane piezoelectric constant of around 0.1 pm/V. Since backfolded region contained two layers with opposite polarity, it had weaker piezoelectricity, proving the symmetry origin of the observed contrast and ruling out the topographic or interfacial effects. The uncertainty primarily came from the spatial variation of the signal.

Chapter 4

Raman spectroscopy in molybdenum ditelluride

The previous chapters dealt with linear electromechanical coupling in quasi-static regime. In this chapter we shifted gear and studied the consequence of mechanical nonlinearity at high frequency: phonon softening under strain.

4.1 Phonon anharmonicity

In an ideal harmonic oscillator where the potential energy is proportional to the square of displacement, the energy of the vibrational mode is independent from either the shift of equilibrium position under additional force F, or the amplitude of existing vibration:

$$H = \frac{p^2}{2m} + \frac{kx^2}{2} + Fx \tag{4.1}$$

$$\Delta E = E_{n+1} - E_n = \hbar\sqrt{\frac{k}{m}} \tag{4.2}$$

where H is the standard Hamiltonian plus the external force, and n is the number of existing phonons. However, the real potential energy in a crystal is anharmonic (Fig. 4.1). Intuitively, the potential becomes softer when the phonon population increases, or the lattice constant is increased under stress. The classical manifestation of this effect is thermal expansion, in which high temperature excites more phonons and relaxes the lattice simultaneously. It also enables collision between phonons and gives rise to thermal resistivity. Mathematically, the anharmonicity is captured by the Grüneisen parameter γ [132]:

$$\gamma = \left(\frac{\mathrm{d}P}{\mathrm{d}u}\right)\bigg|_V = \frac{\alpha v_s^2}{C_P} \tag{4.3}$$

where P is the pressure, u the vibrational energy per volume, α the thermal expansion coefficient, v_s the sound velocity and C_P the heat capacity per-mass at constant pressure.

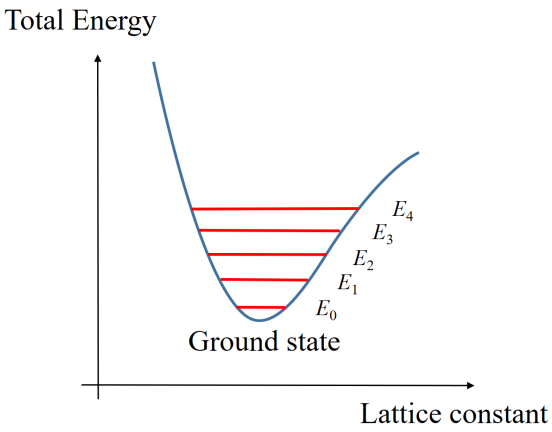

Figure 4.1: Anharmonicity of phonon due to the asymmetric lattice potential. The energy difference between phonon levels decreases and the lattice expands with higher phonon population .

The macroscopic Grüneisen parameter is connected to microscopic phonon softening of each phonon mode:

$$\gamma = \frac{\sum_i \gamma_i c_i}{\sum_i c_i} \tag{4.4}$$

$$\gamma_i = -\frac{\partial \ln \omega}{\partial \ln V} \tag{4.5}$$

where c_i is the contribution of heat capacity from the ith phonon mode and ω is the phonon frequency. Theoretically low-dimensional materials may have much larger γ than bulk. But to quantitatively correlated strain and phonon softening, experimental measurement of Raman frequency change as a function of strain is a prerequisite.

The experimental techniques to measure individual phonon energy are mostly based on inelastic scattering of high-energy particles, including visible photon (Raman spectroscopy [133]), neutron [134], electron [135, 136] and X-ray [137]. Whereas all the other methods can probe the full phonon spectrum, Raman scattering only provides information of phonons at Γ point (near zero momentum) because of the small momentum of visible photon compared to phonon. Yet it has many practical advantages such as high energy resolution with relatively simple instrumentation and very little requirement on samples. Therefore it is widely used in chemical and material analysis. With the discovery of surface enhance Raman spectroscopy [138], the spatial resolution and the sensitivity has been improved to single-molecular level [139]. Even without near-field technique [140] it is sufficient for resolving nanostructures of two-dimensional materials [141]. It is also a powerful method to efficiently map the local defect levels [142] and doping density [143].

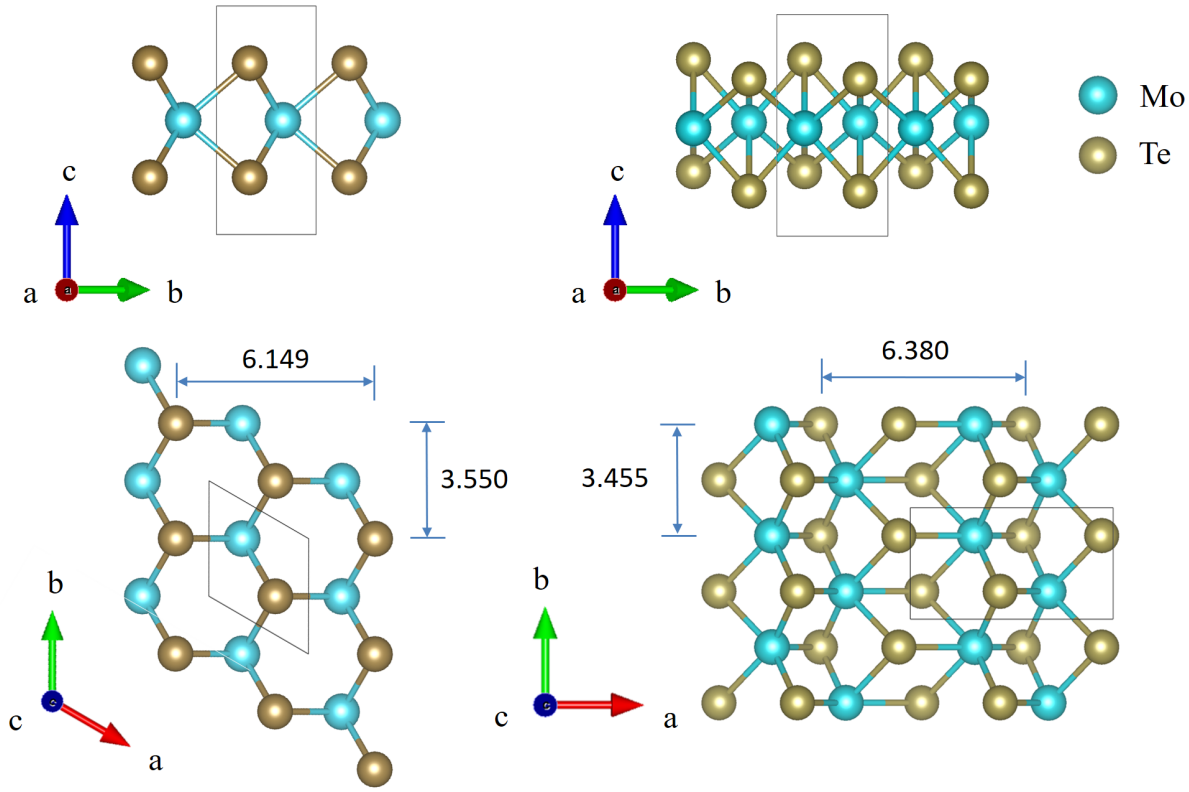

Figure 4.2: The lattice structure of monolayer H (left) and T' (right) $MoTe_2$. The distance between the Te columns is longer in T' than in H phase, but shorter between Te rows [148]. Therefore strain changes their relative energy.

Phonon softening by tensile (compressive) strain translates to the red (blue) shift of Raman peaks. It has been applied to monitoring the residue stress during the growth and processing of polycrystalline semiconductors [144] as well as diamond [145]. To analyze the quality of chemically grown two-dimensional materials, calibrations have been done for graphene [146] and MoS_2 [147]. They showed many similar Raman features owing to the common 3-fold symmetry but quite different Grüneisen parameter, demonstrating the sensitivity of anharmonicity to the details of chemical bonding. $MoTe_2$, another member of the group VIB TMDC, is interesting because of the recently theoretical prediction of phase transition from 2H semiconductor to 1T' semimetal under moderate strain [148]. The 1T' phase is not only a electrical contact material in devices [149], but also a type-II Weyl semimetal [150]. Furthermore, monolayer 1T'-$MoTe_2$ was predicted to be topological insulator under strain [151] Therefore, our objective was to measure the strain-dependent phonon-softening as a reference for strain engineering of $MoTe_2$ in the future.

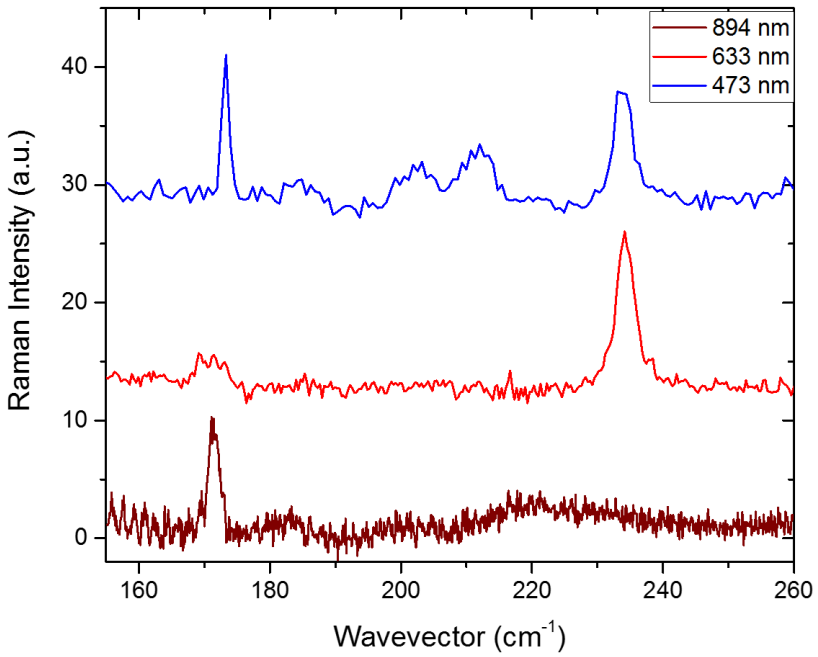

Figure 4.3: Excitation-dependent Raman spectrum in few-layer $MoTe_2$.

4.2 Optical resonance and polarization selection

Our samples were mechanically exfoliated from $MoTe_2$ crystals grown by chemical vapor transport from HQgraphene, and the experimental setup is modified Horiba LabRAM Raman spectrometer. The first challenge came from the weaker electron-phonon coupling in $MoTe_2$ [152] resulting in much weaker Raman scattering than in MoS_2. Therefore we carefully selected the excitation wavelength and utilized the strong optical resonance effect analogous to MoS_2 [153–155]. The excitation-wavelength dependence of Raman spectrum in $MoTe_2$ film (Fig. 4.3) could be understood based on its absorption spectrum [156, 157]. At lower excitation energy (894 nm, around B exciton) the electronic transition conserves circular polarization of light (see the next chapter for discussion in depth) and only out-of-plane mode couples strongly with optical transition. At higher energy (633 nm, around A' exciton), the optical transition is enhanced by the electronic singularity at M point in the Brillouin zone. At even higher energy (473 nm, around C exciton), the one-phonon scattering is weak while a few two-phonon overtones emerge due to more available electronic bands. Since the in-plane mode was expected to soften most under strain, we chose 633 nm excitation in our experiment.

Next we identified ultrathin $MoTe_2$ flakes by atomic force microscope and optical contrast. The Raman signature depends strongly on layer number (Fig. 4.4), particularly the intensity ratio between the 172 cm^{-1} and 235 cm^{-1} peak and the splitting of the former. Both the shift

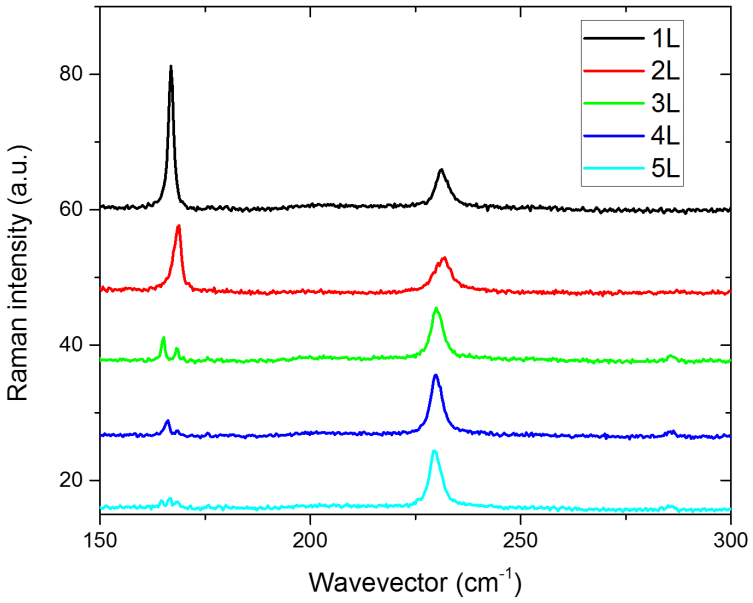

Figure 4.4: Raman spectra of 1- to 5-layer $MoTe_2$.

and the splitting of the 172 cm^{-1} peak in 2-5 layers can be ascribed to the interlayer coupling and the crosstalk with the out-of-plane breathing mode [158].

Finally we determined the corresponding vibrational mode to each Raman peak by classical polarization analysis. This is important for strain analysis because intuitively the in-plane strain affects the in-plane modes to a greater extent. The monolayer H-$MoTe_2$ has three atoms in each unit cell and therefore six optical phonon modes. According to the $P\bar{6}m2$ symmetry, the only Raman active modes and their Raman tensors are [120]:

$$A_1' = \begin{pmatrix} a & & \\ & a & \\ & & b \end{pmatrix} \tag{4.6}$$

$$E'' = \begin{pmatrix} & c & \\ c & & \\ & & \end{pmatrix} \oplus \begin{pmatrix} & -c & \\ -c & & \\ & & \end{pmatrix} \tag{4.7}$$

$$E' = \begin{pmatrix} d & & \\ & -d & \\ & & \end{pmatrix} \oplus \begin{pmatrix} & -d & \\ -d & & \\ & & \end{pmatrix} \tag{4.8}$$

where A_1', E' and E'' are Mulliken symbols and a through d are positive real number denoting the scattering strength. To maximize sample area under light illumination and collection

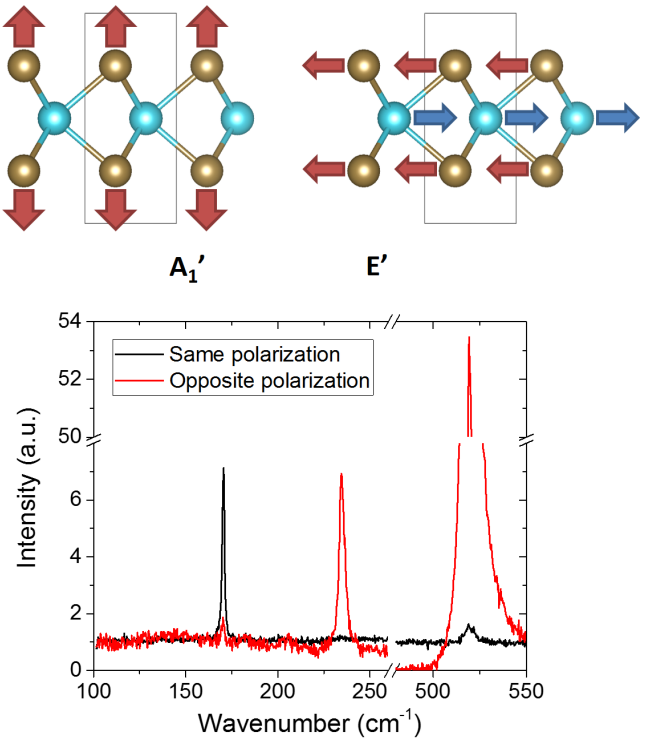

Figure 4.5: The circular polarization of backscattering Raman with respect to incident light distinguishes the two active modes A_1' (upper-left, 171 cm^{-1}) and E' (upper-right, 235 cm^{-1}) in $MoTe_2$. The 520 cm^{-1} peak of silicon substrate which should have the opposite circular polarization to the incident light in [001] direction was used as reference.

we chose normal incidence ($\bar{Z}$) and reflection (Z). Therefore the electric field was only in-plane and E'' mode was silent. The remaining two modes were easily distinguished by the polarization selection rules expressed in the Porto's notation:

- A_1': $\bar{Z}$(RR)Z=a; $\bar{Z}$(RL)Z=0
- E': $\bar{Z}$(RR)Z=0; $\bar{Z}$(RL)Z=d

where R and L stand for right and left circular polarized light, respectively. Hence the vibration modes could be uniquely assigned to each Raman peak [159]. We found that contrary to MoS_2, in $MoTe_2$ the lower energy peak (171 cm^{-1}) corresponds to A_1' mode, and the higher energy peak (235 cm^{-1}) to E' mode, because of the larger mass of tellurium atom compared with molybdenum.

4.3 Straining two-dimensional materials

One of the most widely used methods to apply strain on small samples is substrate-supported strain transfer. In tensile test, the substrate is clamped at the two ends and pulled in opposite direction, when the entire substrate experiences uniaxial tensile strain. In flexural test the finite thickness of the bent substrate means that the outer surface experiences tensile uniaxial strain. Since our sample was tens of micrometers compared with centimeter-size substrate, we only measured the local strain at the center of the substrate where the sample was located. Therefore, the tensile test and the two-point/three-point flexural tests were sufficient. But when large-area inspection is needed, four-point flexural test can apply uniform strain over a significantly larger portion of the substrate. Assuming the sample is rigidly attached to a sufficiently stiff substrate, it should theoretically experience the same strain as the surface. Therefore the strain of the thin flake can be either measured by markers on the surface [146] or calculated from the local curvature of the substrate [147]. In practice however, the substrates are typically composed of flexible polymers with Young's modulus much smaller than the two-dimensional crystals. Hence proper clamping is important for quantitative interpretation of strain testing (Fig. 4.7).

In our strain experiment, Ultrathin flakes were exfoliated directly onto polyethylene trephthalate (PET), polyimide (PI) or polycarbonate substrates, or dry-transfered onto polydimethylsiloxane (PDMS) substrates. The surface roughness was typically below 1nm. The metal clamps on the flakes were fabricated either by lithography (on PET and PI) or shadow mask (on PDMS and polycarbonate), as shown in Fig. 4.7. The clamps were fabricated perpendicular to the Mo-Te bonding direction ("armchair") so that the uniaxial stress effectively stretched the bond. The orientation of the samples were confirmed by second harmonic generation.

4.4 Strain-induced phonon softening

Uniaxial strain not only softens the phonon but also breaks the 3-fold symmetry of the crystal. Therefore, the originally degenerate E' mode splits into two modes (E'_+ and E'_-), and the linear polarization of each mode becomes orthogonal to each other like in the case of MoS_2 [160]:

$$I_{E'_+} \propto \cos^2(\phi + \psi + 3\theta) \tag{4.9}$$

$$I_{E'_-} \propto \sin^2(\phi + \psi + 3\theta) \tag{4.10}$$

where ϕ and ψ are the polarization angle of the incident and scattered light from the strained axis, respectively. θ is the orientation of the crystal defined by the difference between the Mo-Te bonding (a-axis in Fig. 4.2) and the strained axis. Figure 4.8 shows the average Raman peak shift as a function of polarization of the detector under 1.1% uniaxial strain. The shift maximized around 0° and minimized around 90°, confirming that the strain was

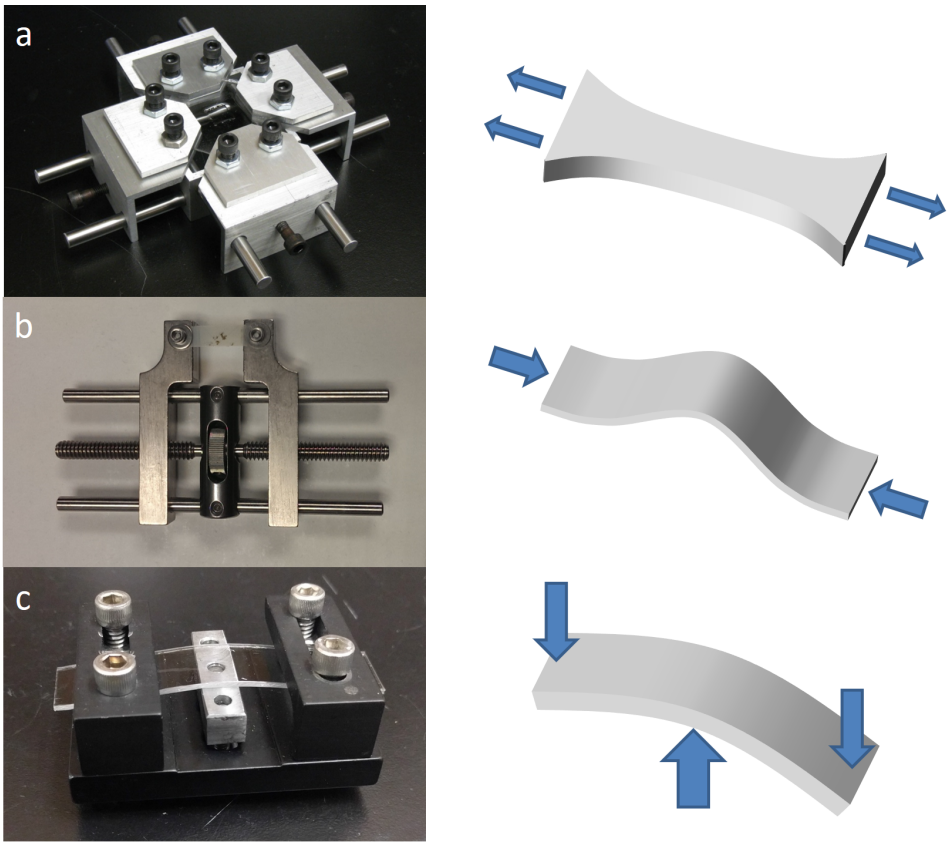

Figure 4.6: Home-made strain platforms and schematics of substrate straining: (a) Tensile testing is most effective for elastic PDMS substrates, because PDMS has very low Young's modulus ($\sim$ 1 MPa depending on composition and curing condition) and very large reversible elastic limit ($>$ 100%). (b) Two-point flexural testing is suitable for PET or PI sheets whose thickness is on the order of 100 μm and requires large curvature to reach the same strain. (c) Three-point flexural testing is for thick polycarbonate plates. The large sample size and small curvature gives better optical access. The central wedge can be replaced by ball indenter to create local biaxial strain.

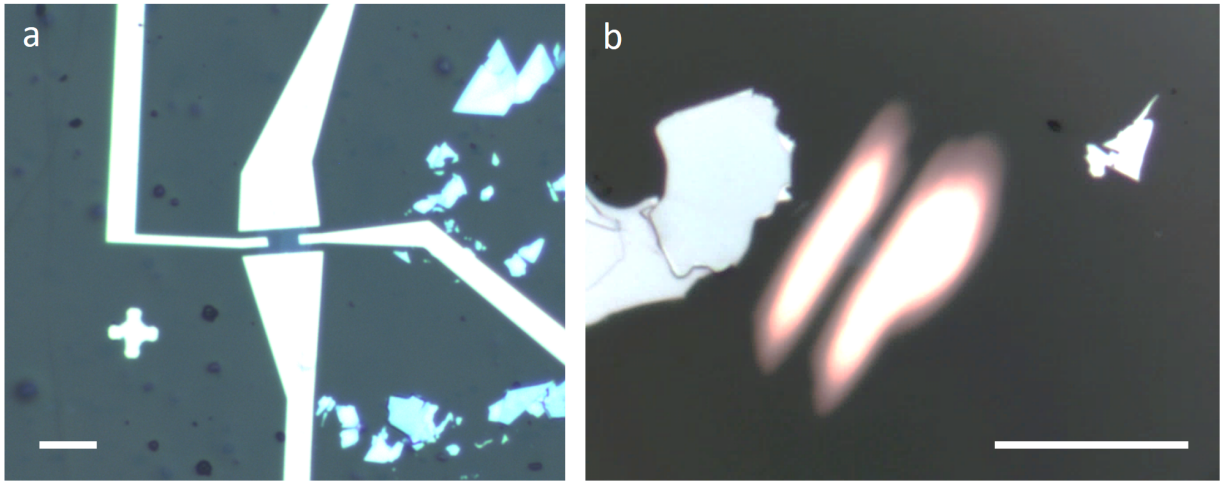

Figure 4.7: Two-dimensional flakes clamped on flexible substrates by (a) e-beam lithography and (b) shadow mask. Scale bar: 20 μm.

along the bonding direction ($\theta = 30°$). The rates of phonon softening were measured on multiple samples and averaged to be 1.4 cm^{-1}/% for the E'_- mode and 0.4 cm^{-1}/% for the E'_+ mode. The values were confirmed by DFT calculation (1.6 and 0.6 cm^{-1}/%, respectively). Therefore, we calculated the Grüneisen parameter and the shear deformation potential for the E'_- mode [161]:

$$\gamma_{E'} = -\frac{\Delta\omega_{E'_+} + \Delta\omega_{E'_-}}{2\omega_{E'}\epsilon} = 0.4 \tag{4.11}$$

$$\beta_{E'} = -\frac{\Delta\omega_{E'_+} - \Delta\omega_{E'_-}}{\omega_{E'}\epsilon} = 0.17 \tag{4.12}$$

where ϵ is the strain along the bending direction. We emphasize that since our substrate was thin shell (thickness $t \ll$ width), there was no transverse strain and the Poisson's ratio of the substrate was irrelevant. The values are significantly less than either graphene or MoS_2 indicating much less anharmonicity. $\gamma_{E'}$ was also verified by applying biaxial stress at the center of the substrate.

Using Raman as calibration tool we could obtain accurate strain values even from samples without clamping. We found that the maximum strain we obtained in $MoTe_2$ was $\sim$ 2.5% regardless of clamping. Figure 4.11 shows the Raman spectrum from strained 3-layer under nominal 4.2% strain (measured from the substrate). The flake also exhibited visible deformation, confirming that the displacement was transferred to the sample, but further straining could not increase phonon softening. Although this strain value was also predicted to be the onset of phase transition, and indeed we observed some optical contrast difference, we were unable to observe any Raman signal expected for the new phase. It is possible

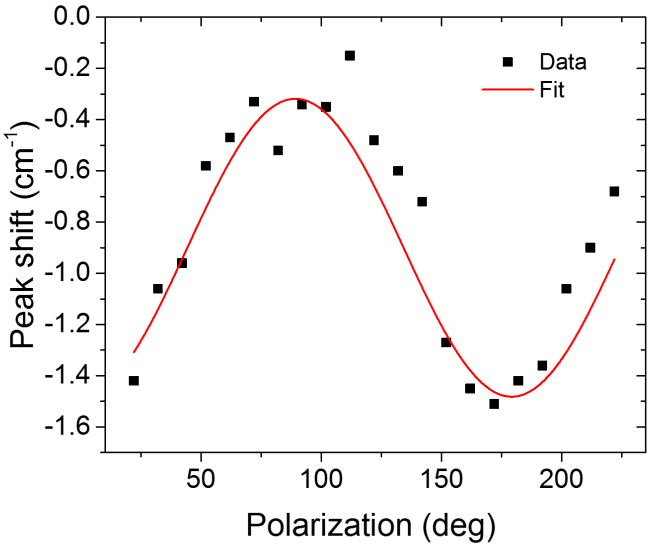

Figure 4.8: Polarization dependence of the E' peak shift. The center of single-peak fitting was plotted in marker and a waveform fitting was in red line. The fitting was only to confirm the direction of strain and had no physical meaning because the spectrum actually contained two peaks.

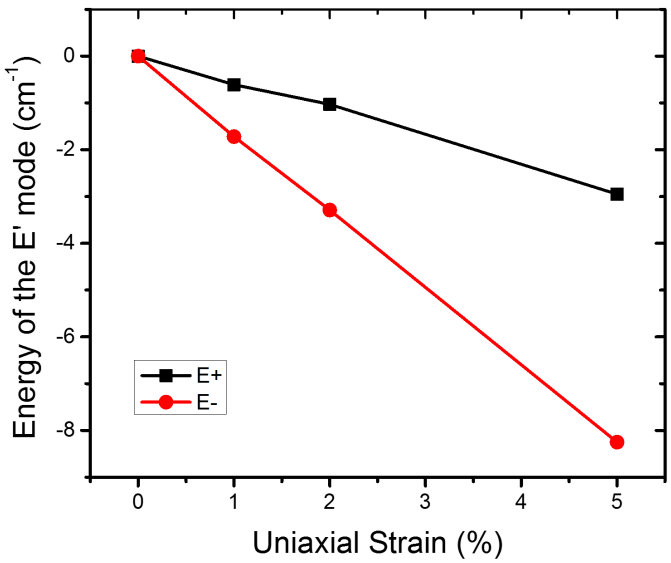

Figure 4.9: Calculated strain dependence of the E' peak shift

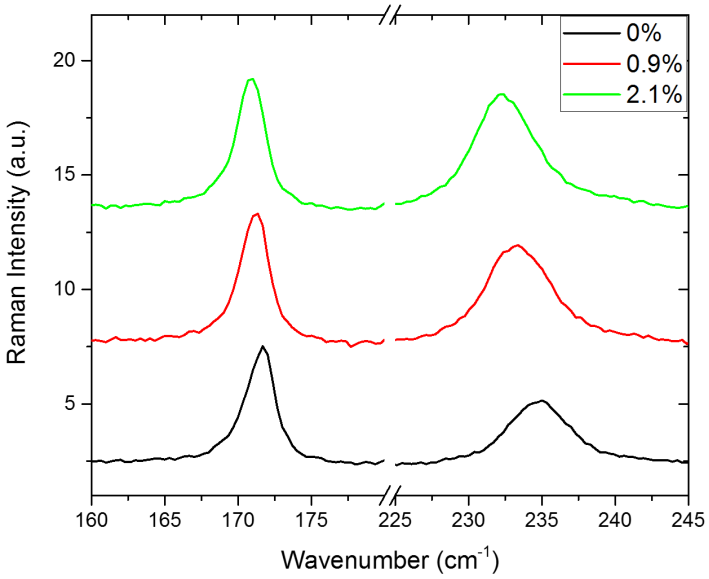

Figure 4.10: Phonon-softening of both A_1' and E' modes of monolayer $MoTe_2$ under biaxial stress. From the peak shifts we calculated $\gamma_{E'} = 0.5$ and $\gamma_{A_1'} = 0.25$. The difference in the value of $\gamma_{E'}$ from uniaxial tests came from experimental uncertainty, and the average value of 0.45 was reported.

that the crystal broke at the weak links near the sites of phase transition, or the new phase was amorphous/unstable in ambient condition, although the flake was protected from the atmosphere by PMMA coating.

4.5 Summary

In summary, we observed the phonon softening induced by uniaxial mechanical strain in $MoTe_2$. The Grüneisen parameters for the two optical phonon modes A_1' and E' were measured and agreed well with first-principle calculation, which indicated smaller phonon anharmonicity than MoS_2. On the other hand, the predicted phase transition was not conclusively observed mainly due to the limitation of the method of tensile mechanical straining in ambient condition.

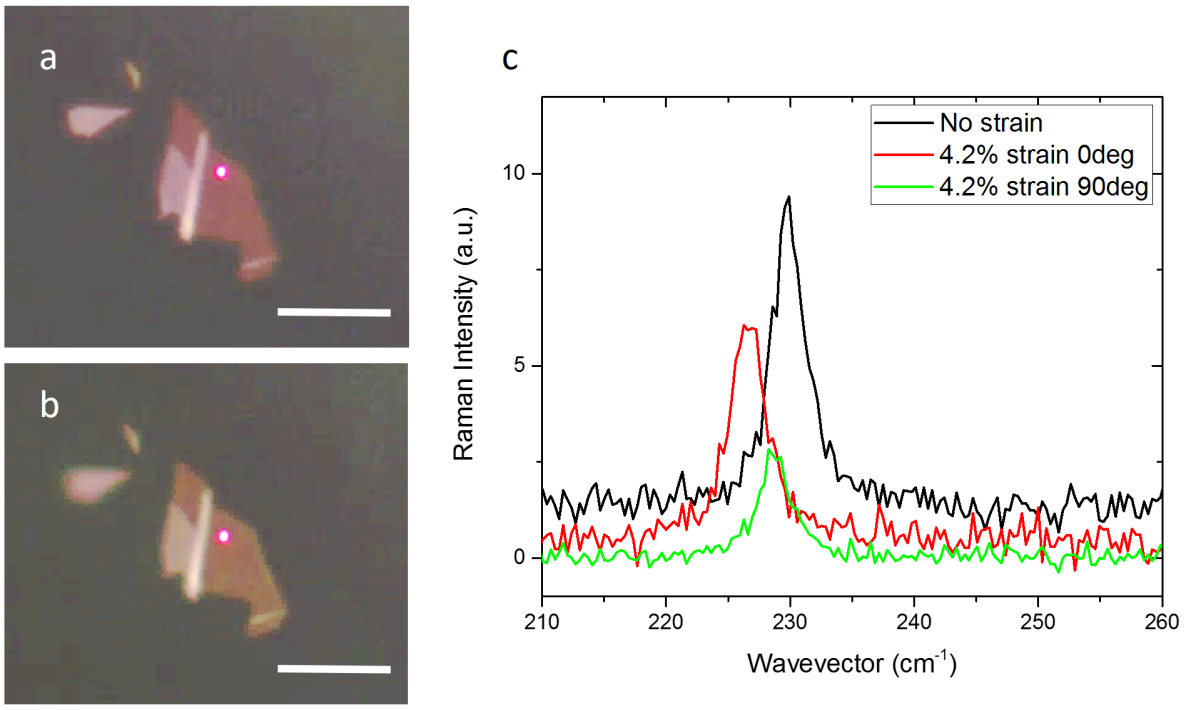

Figure 4.11: Critical strain in 3-layer $MoTe_2$. The optical images of the flake before (a) and under (b) 4.2% strain show color difference and obvious deformation. (c) The Raman spectrum indicated that the real strain was only 2.4%. No new peaks were detectable.

Chapter 5

Chiral phonon in valley polarized tungsten diselenide

In the previous chapter we studied anharmonicity of phonon, one of the fundamental properties of lattice vibration. This chapter explored another fascinating phononic property in two-dimensional materials that had just been discovered recently: angular momentum. The research on phonon traditionally focused on its energy and linear momentum, but very rarely on the angular momentum because few experimental methods can directly couple to this degree of freedom. One such example is in gas-phase infrared spectroscopy, where the quantization of molecular rotation gives a series of absorption lines near each vibrational mode. The conservation of angular momentum leads to the selection rule of rotation-vibrational transition [162]:

$$\Delta J = \pm 1 \tag{5.1}$$

where J is the rotational quantum number. Therefore regardless of the polarization of incident light, the central line corresponding to the transition without changing the rotational energy is forbidden. For Raman scattering, since there are two photons involved, the selection rule becomes $\Delta J = 0, \pm 2$. Similar analysis has been conducted for nuclear transition [163] and nanocrystals [164, 165].

In periodic lattice, although there is no global rotation, lattice can still carry angular momentum through spin-orbital coupling and relaxes the spin angular momentum [166]. The selection rule is not explicit because we typically assume that there must be some phonons among numerous available modes capable of scattering the electrons with the right momentum. This effect plays an important role in the ultrafast light-matter dynamics of ferromagnetic materials [167, 168]. The limitation of photon-phonon scattering is that it only probes phonon around Γ point, i.e. the center of Brillouin zone in reciprocal space with nearly zero linear momentum, because the wavelength of visible light is much larger than the lattice constant. In addition, the phonon eigenmodes at Γ have zero intrinsic angular momentum and thus an effective rotation mode must be synthesized [169]. As a consequence,

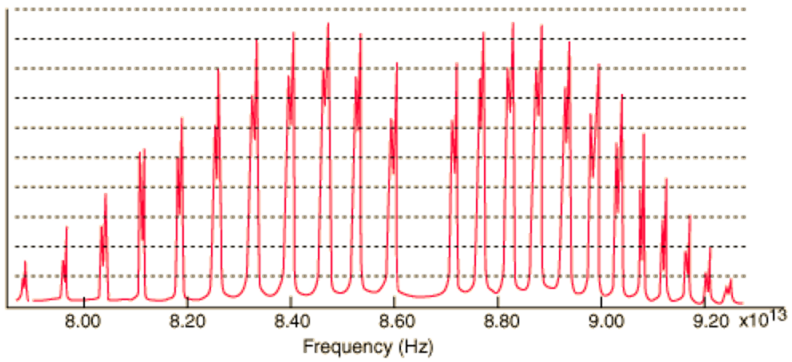

Figure 5.1: The high-resolution infrared absorption spectrum of gaseous HCl. The angular momentum conservation manifests through the missing line near 86.5 THz.

there is no direct evidence of intrinsic angular momentum of phonon and its role in electron-phonon interaction in solids. Recently, chiral phonon was theoretically predicted at non-Γ high-symmetric point in two-dimensional hexagonal lattices [170]. The intrinsic angular momentum and magnetic moment of chiral phonon potentially allows ultrafast information processing and manipulation of magnetism. Our objective here was to experimentally and directly connect the angular momentum of a single phonon mode with photon and electron.

5.1 Valley degree of freedom

The term "valley" describes the energy extrema in semiconductors and semimetals at non-Γ points in momentum space. Time reversal symmetry dictates that such systems must possess pairs of degenerate valleys with opposite momenta. The particles can selectively reside on one of the valleys, i.e. "valley polarized", and carry the information through this valley degree of freedom. Similar to spintronics, the benefit of "valleytronics" comes from the energy degeneracy, so that the energy cost of switching and transporting a bit of information is much lower than that of moving electric charge in conventional electronics. Valley polarization has been realized in a few conventional materials like silicon [171], III-V semiconductor [172] and diamond [173]. However, strong intervalley scattering at room temperature remains a challenge for valleytronic applications in these materials.

Two-dimensional hexagonal lattices provide unique opportunity for exploring valley degree of freedom because of symmetry-suppressed intervalley scattering [174], as shown in Fig. 5.2. First, the hexagonal lattice corresponds to hexagonal reciprocal lattice in momentum space. The conventional way to define the central unit cell of reciprocal lattice (the first Brillouin Zone, FBZ) is to set the lattice point at the center (Γ point) and draw a symmetric boundary around it. Such definition reveals a few sets of equivalent, highly symmetric points

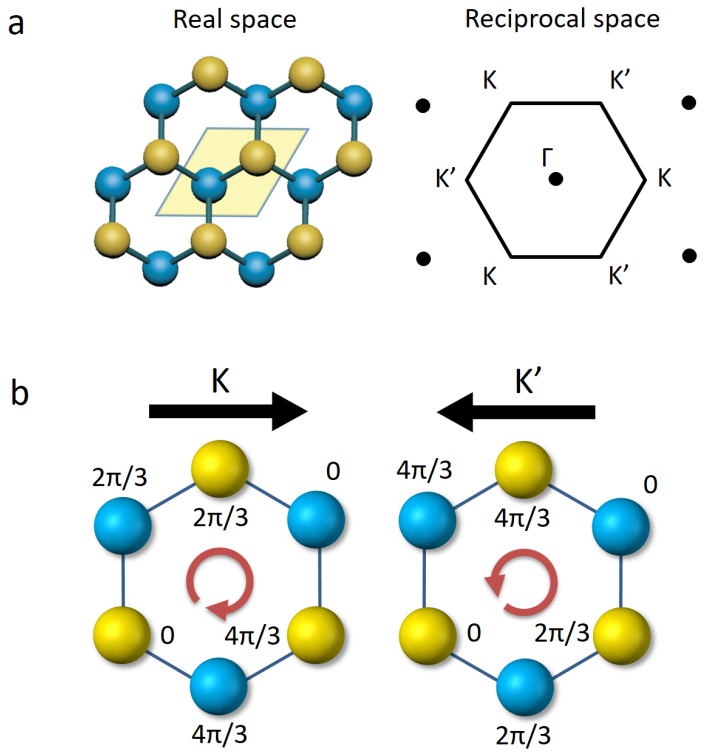

Figure 5.2: Illustration of valley degree of freedom in asymmetric hexagonal lattice. (a) Representations of the lattice in the real space (left) and the reciprocal space (right). The solid lines encircle the central unit cell. (b) The phase relationship of the plane-wave function at K and K' point within a hexagonal ring. The relative phase is equivalent to that of a rotating wavefunction.

such as K and K' at the corner of FBZ. Second, the momentum of electron corresponds to a propagating plane wave which essentially is determined by the phase difference of wavefunction near adjacent atoms. For K and K' point, there are only three choices of relative phase: 0, $2\pi/3$ and $4\pi/3$. Hence the phase configuration of each momentum looks as if the wavefunction is rotating clockwise or anti-clockwise. According to the quantum definition of angular momentum:

$$\hat{L_z} = -\frac{\hbar}{i\phi}\ln(\hat{R}(\phi)) \tag{5.2}$$

it is clear that by setting $\phi = 2\pi/3$, a wavefunction localized on the chalcogenide atom with intrinsic angular momentum of zero gains a pseudo angular momentum of -1 at K (+1 at K'). Therefore, the scattering between K and K' point is forbidden unless additional angular momentum is provided.

The angular momentum associated with valley also offers the possibility to selectively control optical transition between bands at K (or K') point. The wavefunctions of electrons in different bands usually inherent different intrinsic angular momentum from spin and atomic orbital, so that the total angular momenta must summarize the contribution of intrinsic and valley-induced angular momentum distributed on both atoms. The fact that eigenvectors must have the same symmetry as the Hamiltonian ensures that the total angular momenta are always integers. As a consequence, the optical transition satisfies the angular momentum conservation:

$$0 = \Delta l = \Delta l_{\text{final,K(K')}} - l_{\text{inital,K(K')}} \pm 1 + 3m \tag{5.3}$$

where $\pm$ corresponds to right and left circularly polarized light, and the integer m stands for the contribution from the 3-fold symmetry of the lattice. Furthermore, time-reversal symmetry dictates that if the optical transition is allowed, then the K and K' valley must respond to opposite circular polarization.

Early theoretical proposals focused on creating valley polarization in graphene [175, 176] but experimental realization was slow and difficult due to the requirement of artificial symmetry breaking [177–179]. Fortunately, inversion symmetry is already broken by the crystalline structure of the group VIB transition metal dichalcogenides (TMDC), potentially making them a better platform for generation and detection of valley polarization [180]. Moreover, unlike bulk TMDC with indirect band gap, the conduction band minimum and the valence band maximum in monolayer TMDC are both located at K/K' point [100, 181]. Therefore it is possible to optically address valley electrons, whose large momenta typically prevent direct interaction with light.

The experimental realization of valley polarization (nearly 100% in some reports) simply by circularly polarized optical pumping [182–184] profoundly expanded the accessibility and scope of valleytronics (Fig. 5.3). Since then, many quantum processes based on valley degree of freedom have been demonstrated, including valley coherence [185], valley Hall effect [186, 187] and gate operation [188]. The lifetime of valley polarization has also been prolonged by orders of magnitude with interlayer excitons in heterostructures [189] by circumventing very fast intrinsic depolarization mechanism [190, 191]. However, the optically injected valley polarization fails to deliver the original promise of energy efficiency because most of the energy is spent to overcome the band gap instead of the thermal fluctuation. Electrical creation of valley polarization in TMDC such as symmetry-breaking p-n junctions [192] and spin-injection [193] also suffers the same problem.

5.2 Valley polarization and chirality of phonon

From the discussion above, it is evident that the valley degree of freedom is applicable to not only electrons but any quasi-particles in the lattice. Indeed, phonons at K and K' point in hexagonal lattices are also candidate carriers of valley quantum number. Compared with electrons, phonons cost much less energy to store valley information and preserve

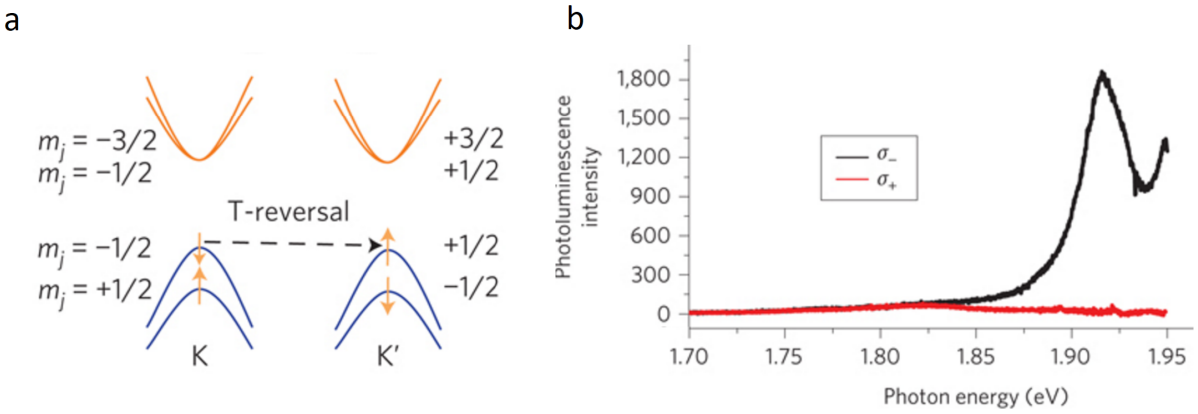

Figure 5.3: Optical pumping of valley polarization. (a) Band diagram near K and K' valley in TMDC. The spin-orbital coupling splits both the conduction band and the valence band. m_j denotes the total angular momentum of the electronic wavefunction. (b) The photoluminescence in MoS_2 at 14 K kept almost pure circular polarization of the incident light if pumped on resonance. Reprinted with permission from [182].

longer coherence time even at room temperature [194]. The most striking feature of the valley-polarized phonons is that they also have intrinsic spin angular momentum and spin-valley locking as electrons, and thus exhibit all the physical properties of valley electrons like symmetry protection, optical selection rule and Berry curvature [170]. The spin angular momentum of phonon is illustrated in Fig. 5.4, where the atomic motion of the phonon eigenmode at K point is circular instead of the linear motion at Γ point (Fig. 4.5). We emphasize that the circular motion at K point is *fundamentally distinctive from the superposition of two degenerate linear modes*, because the spin-valley locking splits the energy of phonons with opposite spin. Therefore unlike short-lived synthesized circular motion [168], the valley lifetime in phonon is determined not by the coherence decay but by the much slower population decay.

In asymmetric hexagonal lattices where the atoms at A and B sites have different mass, the energy degeneracy is fully lifted. For monolayer TMDC, because there are two chalcogenide atoms at the B sites, 9 phonon branches are formed around K and K' valley. However, not all of them are detectable through electron-phonon coupling. In the following sections we will discuss two possible pathways of photon-phonon interactions: Raman scattering and indirect absorption.

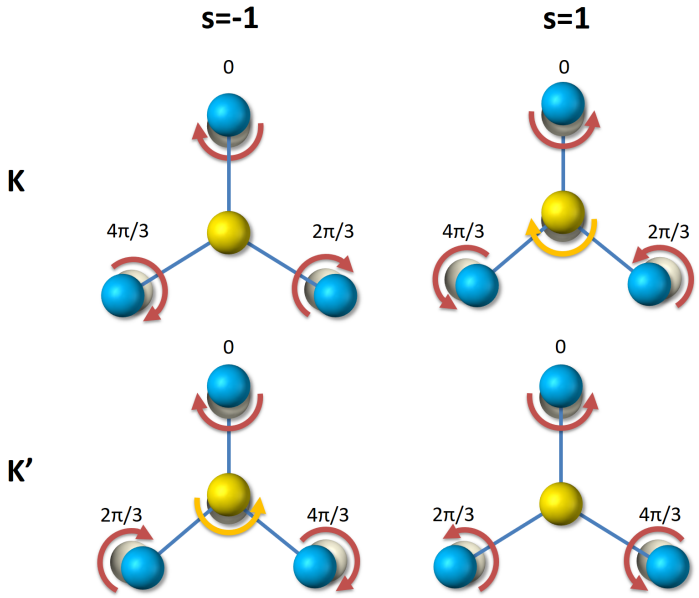

Figure 5.4: Illustration of the vibrational modes of chiral phonon at K and K' point. Blue and yellow denote A and B site in the asymmetric hexagonal lattice, while gray marks the equilibrium position. We started the analysis from a mode (upperleft) in which the atoms at A site move symmetrically and the atoms at B site remain still. In order to keep equal bonding length and angle, the A atom must rotate clockwise (spin $s = -1$). On the other hand, if the spin is flipped, the force on the B atom can no longer be balanced, so it must rotate anti-clockwise. Evidently, these two modes are different and their energy levels split. Time reversal symmetry protects the spin-valley locking, i.e. $E_{\mathrm{K,s}} = E_{\mathrm{K'},-\mathrm{s}}$.

5.3 Raman scattering of large-momentum phonon

As discussed previously, valley phonons typically do not interact with light because of momentum mismatch. There are two exceptions: defect in crystals can relax the momentum selection rules and activate a one-phonon continuum in the Raman spectrum whose intensity is roughly proportional to the density of state (DOS); two-phonon scattering involving simultaneous emission of two phonons with opposite momenta from the same branch adds another continuous background approximately proportional to the double-frequency density of state ($2\omega-$DOS) [195]. Since phonon modes around M point contributes most to the DOS, the defect-activated and the two-phonon peaks in the Raman spectrum of TMDC are traditionally assigned to various modes of M-phonon [196]. However, optical excitation around the electronic resonance disproportionately enhances phonon scattering that connects two real electronic states [197]. Such double-resonant Raman scattering is prominent for phonons with large wavevectors if they effectively connects two remote valleys as in graphene [198].

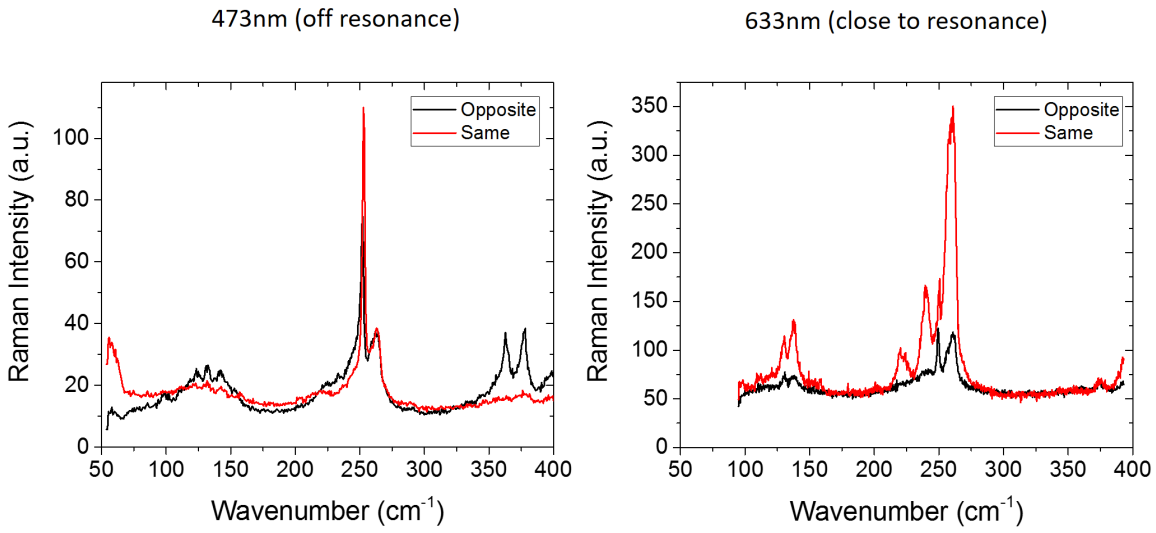

Figure 5.5: The polarization selection rules of Raman scattering by phonons with large momentum through off-resonant (473 nm laser, left) and on-resonant (633 nm laser, right) excitation. The red and black curves stand for scattering light with the same and opposite circular polarization to the incident light. The defect-activated spectrum showed opposite selection rule under the two conditions. The two-phonon spectrum has no obvious off-resonant circular selection and clear on-resonant selection. Both sets of lines indicate the valley phonons may be involved in the scattering process.

This is also the case with monolayer TMDC at the wavelengths of the A and B exciton, and peaks from K-phonons were identified [199, 200].

We compared the polarization selection rule of both one-phonon and two-phonon scattering excited off-resonantly and resonantly (Fig. 5.5. The sample was continuous film of chemical vapor deposited (CVD) WSe_2 [201], chosen for its large valence band splitting explained in details in the next section. First we observed that the circular polarization of the back-scattering with respect to the incident circular polarization for A_1' (Z(LL)$\bar{\text{Z}}$) and E' (Z(LR)$\bar{\text{Z}}$) agreed with literature. These two peaks in monolayer WSe_2 are very close and yet clearly distinguished by their opposite polarization with both excitation wavelengths. Next we found the defect-activated one-phonon continuum between 100-160 cm^{-1} were different in shape and polarization. At 473 nm (off-resonance), the shape of the continuum was very similar to the calculated phonon DOS [202], and the polarization was primarily opposite to the incident light. Yet on resonance, two peaks with the same polarization as the incident light became dominant. The conservation of circular polarization is in accordance with the fact that in monolayer WSe_2 no other point in reciprocal space has allowed optical transition with the same energy as the B-exciton in the originally excited K' valley. It also indicates

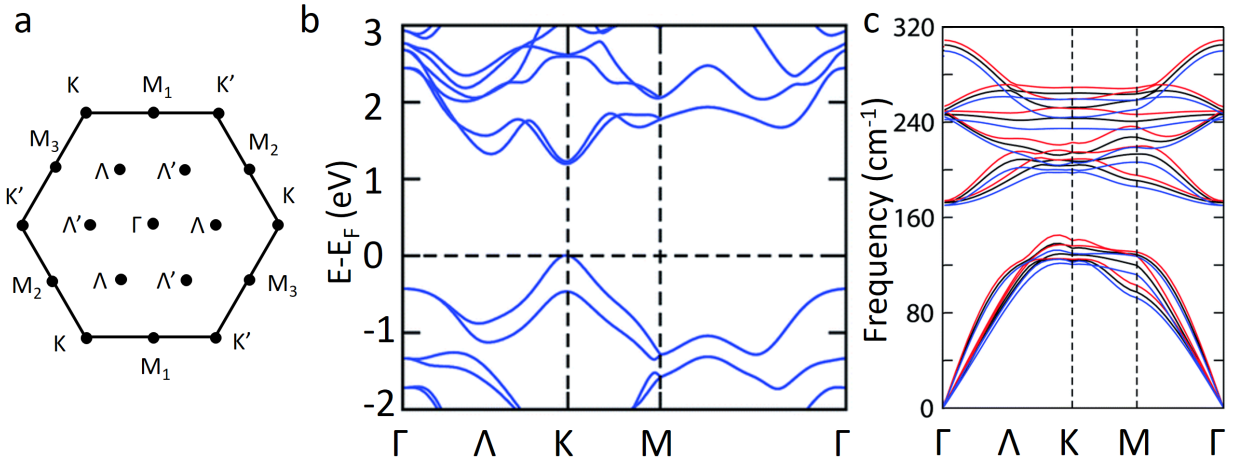

Figure 5.6: (a) The first Brillouin zone of monolayer WSe_2, with high-symmetric points illustrated. The Λ point here is defined as the middle point of the $\Gamma - K$ line. Note that $M_1 = K + \Lambda$. (b) The electronic and (c) phononic band structure of WSe_2 along high-symmetric lines. The blue, black and red lines in (c) correspond to the phonon dispersion of monolayer WSe_2 with -2%, 0% and +2% strain. Adapted with permission from [203]

that such enhancement may be associated with valley phonons.

Then we moved to the continuum between 200-300 cm^{-1}. Visible for both aged CVD samples and high-quality single crystals regardless of defect density, they likely came from the two-photon scattering and the intensity was also correlated with the $2\omega-$DOS. The dispersion of these peaks as a function of excitation was another signature of the two-phonon scattering. While the off-resonant polarization selection was not significant, the on-resonant polarization aligned well with that of the excitation, similar to the one-phonon scattering. From the electronic band structure, we found the double-resonant condition can only be satisfied with a pair of phonons scattering electrons between K and Λ point, or between K and K'-point, or holes between K and Γ point. Therefore both M-phonon and K-phonon contribute to the spectrum. DFT calculation showed that the three acoustic branches of WSe_2 have very similar energy at M and K-point, so from resonant Raman we could directly measure the energy of these phonons to be 14-16 meV.

5.4 Phonon assisted indirect absorption

The electron-phonon scattering enables another one-phonon process: indirect absorption. Although monolayer WSe_2 is a direct-gap semiconductor, the energy difference between spin-split bands is below the optical band gap. Direct optical transition between the spin-split band is forbidden at exactly K/K' point due to the opposite spin, but two types of transition

remain allowed if the valence band maximum has available states, such as when the sample is pumped by circular polarized light (Fig. 5.7). One is between the spin-split bands in the same valley away from the K/K' point, where additional momentum starts to mix the spin through spin-orbital coupling, and the transition is no longer strictly forbidden. The other is spin-allowed intervalley indirect absorption assisted by valley phonon. These two contributions are collectively called intervalence band transition. In photoexcited semiconductors, the phonon-assisted process dominates [204]. Although neither pathways are nearly as strong as direct optical transition, they are considerably enhanced in WSe_2 compared with conventional semiconductor for two reasons. First, in 2D the electronic density of states is finite at K/K' point in contrast to zero in three-dimension (Fig. 1.9). Second, the split bands are almost parallel to each other, leading to even larger optical joint density of states. Therefore the estimated indirect absorption coefficient is on the order of 10^{-5}.

To observe this indirect absorption in a single molecular layer, it is preferable to convert the small relative change of an infrared signal to an absolute change of visible signal. This was achieved through collection of the B-exciton emission from the other valley. The hole population was proportional to the infrared absorption, while the electron population is provided by fast intervalley relaxation to dark exciton states [205]. We differentiated the B-exciton emission from other signals by carefully chose the pump energy around the 2s state of A-exciton. The valley polarization remained high at this wavelength [206]. Due to the large band splitting, strong photoluminescence from A-exciton was easily filtered. The large excitonic energy difference between the 1s and 2s state ensured that the sum frequency generation was well above the B-exciton. Anti-Stokes Raman scattering was reduced by cooling.

Since the indirect absorption only involves one phonon and two electronic bands, it allows us to directly measure the angular momentum of valley phonons. Among the 9 available phonon modes, only two enables electronic intervalley scattering based on symmetry analysis [170]. Moreover, the angular momentum conservation requires:

$$0 = l_{\text{final}} - l_{\text{initial}} = l_{\text{phonon}} \pm l_{\text{photon}} \tag{5.4}$$

where the initial and final angular momentum of the holes are equal for the intervalley spin-conserved transition. Thus the phonon's angular momentum must be opposite to the infrared light in an phonon emission event, or the same in an absorption event. The probability of indirect absorption follows the Fermi's golden rule, assuming that the phonon energy $\hbar\omega_{\text{phonon}}$ and the electron-phonon coupling strength are almost constant near K/K' point:

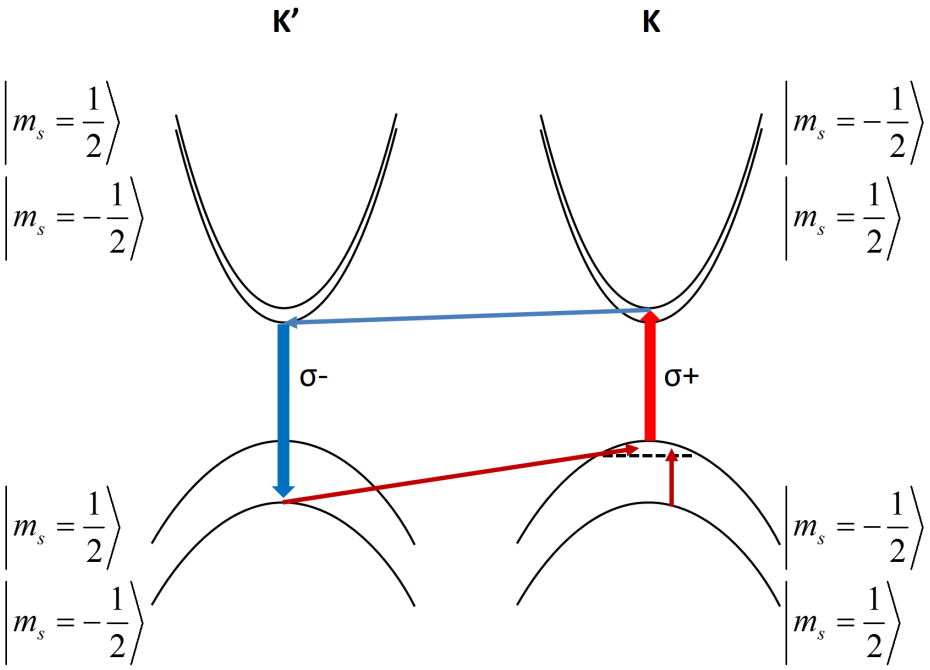

Figure 5.7: Illustration of valley-polarized phonon-assisted indirect absorption. The right-circular-polarized pump creates spin-up holes and spin-down electrons at K valley. Infrared absorption happens between the split bands in the same valley (spin forbidden) and the opposite valley (phonon-assisted and spin allowed). The absorption results in B-exciton emission as the final observable.

$$
\begin{aligned}
\alpha &\propto \int_{-\infty}^{+\infty} \mathrm{d}^2\mathbf{k_1}\mathrm{d}^2\mathbf{k_2}\delta(\frac{\hbar^2(k_1^2-k_2^2)}{2m^*} - \hbar\omega_{\text{photon}} \pm \hbar\omega_{\text{phonon}} + \lambda) f(E_2) \\
&\propto \int_0^{+\infty} f(E_2)\mathrm{d}E_2 \int_0^{+\infty} \delta(E_1 - E_2 - \delta E)\mathrm{d}E_1 \\
&\propto \int_0^{+\infty} f(E_2)H(E_2+\Delta E)\mathrm{d}E_2 \\
&\propto \begin{cases} n_0 & (\Delta E \geq 0) \\ n(E > -\Delta E) & (\Delta E < 0) \end{cases}
\end{aligned}
\tag{5.5}
$$

where $\mathbf{k_1}$ and $\mathbf{k_2}$ are the electronic momenta of the initial and final state, respectively, and E_1, E_2 are the corresponding kinetic energy. λ is the spin-orbital coupling strength and ΔE is the energy surplus of the photon to drive the indirect transition. n_0 is the number of photo-induced holes and $f(E)$ is their energy distribution. $n(E-\Delta E)$ denotes the number

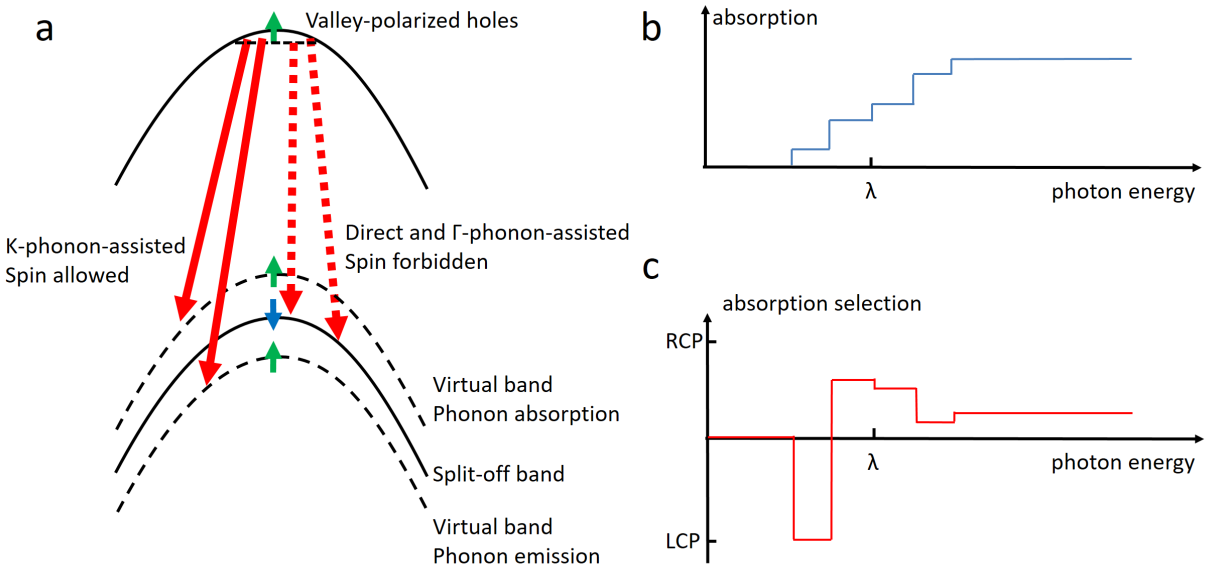

Figure 5.8: Expected spectrum and polarization of indirect inter-valence band transition. (a) Schematic diagram of pathways of intervalence band transition. The absorption and emission of K-phonon project the split-off band in K' valley to virtual bands at K valley. The spin-allowed transitions are marked with solid arrows while the spin-forbidden transitions are dashed arrows. Momentum conservation is guaranteed for phonon assisted transitions. (b) Illustration of the absorption coefficient for phonon energy around the spin-orbital-split energy λ. The five steps correspond to two K-phonon absorption virtual band, one direct band, and two K-phonon emission virtual band. (c) Illustration of the absorption selection defined by $\alpha_R/(\alpha_R + \alpha_L)$. RCP and LCP stand for right- and left-circular polarization, respectively. The two K-phonon modes provide opposite selection rules.

of photo-induced holes with higher energy, regardless the details of the distribution. Because of the two-dimensionality, the absorption spectrum is greatly simplified to the summation of a few step-like functions. Under circular-polarized infrared excitation at zero temperature, only one step from the emission of one phonon mode is expected to appear (Fig. 5.8).

5.5 Polarization-resolved transient infrared spectroscopy

We employed polarization-resolved transient infrared spectroscopy to probe the phononic angular momentum (Fig. 5.9). The CVD WSe_2 sample was mounted in a modified transmission-type cryostat (Janis ST-100) equipped with CaF_2 optical window and cooled down to 90K. The ultrafast light source was provided by Coherent Chameleon optical parametric oscilla-

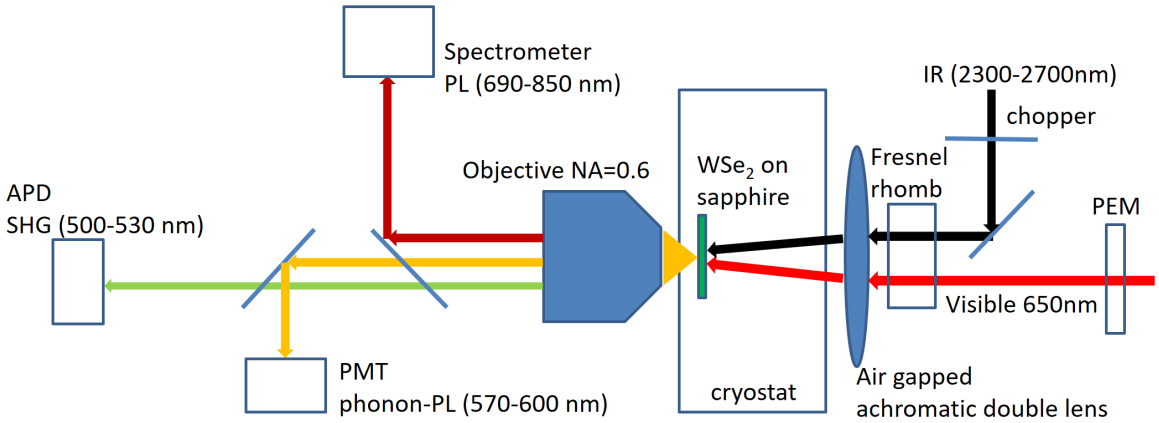

Figure 5.9: Experimental setup of polarization-resolved transient infrared spectroscopy

tor. Valley polarization was initialized by a visible pulse with tunable wavelength between 645-690 nm. The pulse would be polarized by a photoelastic modulator (f=50kHz) that switched between +45° and -45° linear polarization at double frequency without changing intensity. Valley depolarization was expected to be weak because in the lightly p-doped WSe_2, the spin-valley lifetime of holes is on the order of nanosecond [207], much longer than the time scale we studied. The linear polarized infrared pulse was intensity-modulated at 1/6-frequency and delayed by τ through tunable optical path. The pulse duration and the delay were calibrated by sum frequency generation (SFG). Both beams entered the CaF_2 Fresnel rhomb designed for creating a 90° phase difference between the s-and p-wave, becoming circularly polarized and focused on the sample by an infrared air gapped achromatic double lens. The spot size was around 50 μm for both wavelengths. The infrared light was absorbed by the hole population in the sample and created B-exciton emission. All emitted light was collected by a phase-corrected objective lens with numerical aperture of 0.6, and separated according to the wavelengths into three detectors. A free-space coupled photomultiplier captured the wide-angle B-exciton emission. A fiber-coupled avalanche photodiode collected the narrow-angle SFG signal. The spectrometer recorded the A-exciton photoluminescence both as a monitor of sample quality and the real temperature.

The Fresnel rhomb was customized for generating circular polarization from linear polarized light as shown in Fig. 5.11. Total internal reflection (TIR) inside a refractive crystal causes a relative phase gain between the s- and p-wave [208]:

$$\delta = \pi + 2\tan^{-1}\left(\frac{n\sqrt{n^2\sin^2\theta_i - 1}}{\cos\theta_i}\right) - 2\tan^{-1}\left(\frac{\sqrt{n^2\sin^2\theta_i - 1}}{n\cos\theta_i}\right) \tag{5.6}$$

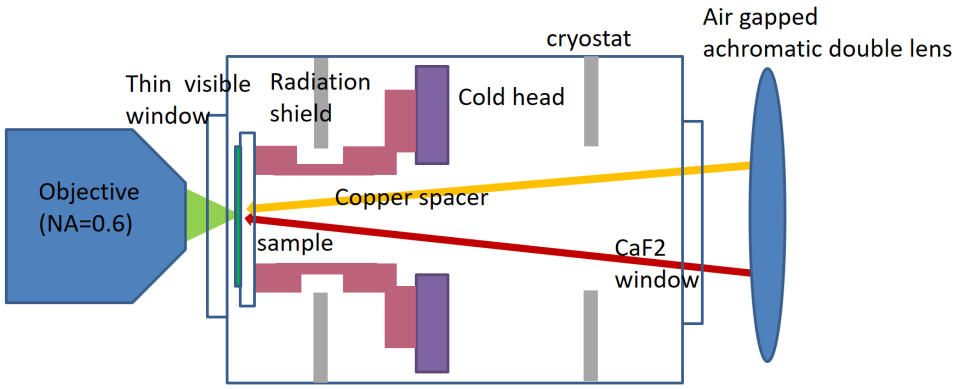

Figure 5.10: In order improve the collection efficiency of luminescence, the sample was brought very close to one of the optical window by a copper spacer. It is necessary to minimize thermal resistance because the thermal radiation from the environment to the sample was as high as tens of milliwatts and potentially raised the temperature of the sample, whereas the temperature sensor of the stage was mounted on the cold head base. The hollow spacer allowed entrance of the excitation beams. Radiation shield effectively lowered the lowest achievable temperature.

where n is the refractive index of the crystal and θ_i is the incident angle which depends on the the cut. Therefore, for materials with low dispersion, TIR enables very broadband retarder. For CaF_2 quarter-wave retarder, the refractive index is not high enough to create 45° delay as in the case of conventional glass visible retarder, so the only choice to accumulate 90° delay is through 4 reflections a pair of symmetrically aligned crystals. The direction of the beam reflected even times is insensitive to the small rotation of crystals. The phase shift from such misalignment is also compensated by the symmetry of the rhomb. In addition, the dispersion of the phase shift is negligible for our application. The only disadvantage is that the phase is now very sensitive to the cut angle and the relative alignment between the two crystals.

5.6 Preliminary results and discussion

Figure 5.12 shows the basic sample characterization pumped with 650 nm pulse. The photoluminescence had three features: exciton at 710 nm, trion shoulder at 725 nm and defect spectra between 730-770 nm. The interpretation of two-photon luminescence (TPL) at shorter wavelength relied on the accurate determination of spin-orbital-split energy λ around 0.5 eV [209, 210]. Based on the sum-frequency generation later we determined that $\lambda \approx 480$ meV in our sample. Including the electronic spin-orbital splitting of about 40 meV, we observed that the TPL contained B-exciton around 565 nm, strong B-trion around 575

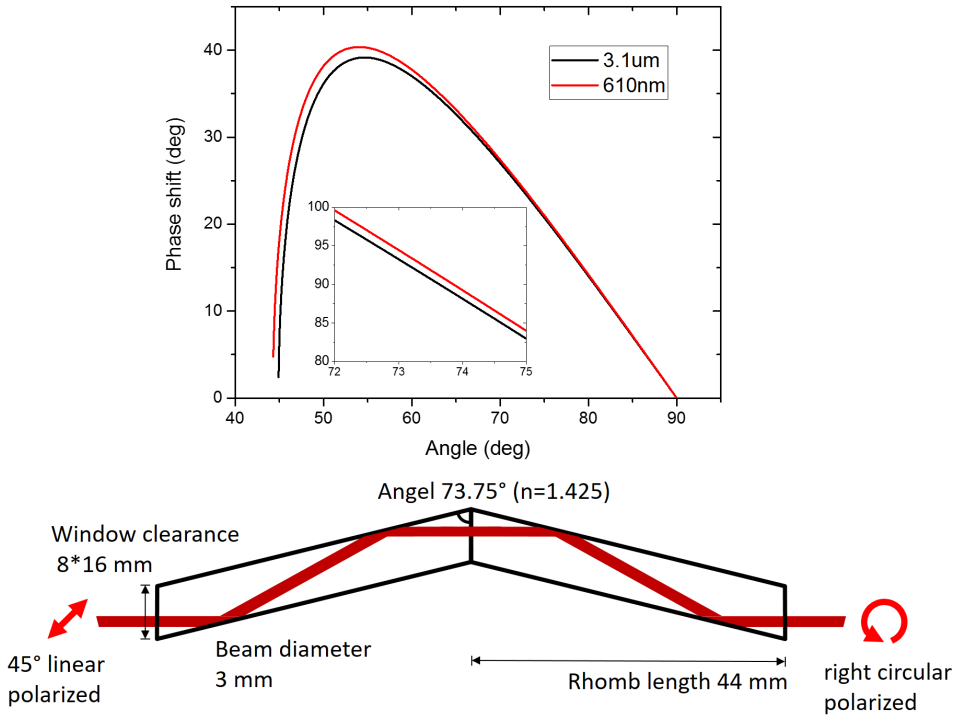

Figure 5.11: Fresnel rhomb as broadband circular polarizer. Top: the relative phase gain between s- and p-wave after one total internal reflection in CaF_2 as a function of incident angle for visible and IR wavelength. Inset: phase gain after four TIR near the designed retardation. Bottom: geometry of the rhomb. The linear polarized beam is transformed into circular polarized beam after four total internal reflection

nm and B-defect spectra between 580-600 nm. The power dependence of photoluminescence under continuous-wave excitation also indicated that the excitons are charged, because the Coulomb repulsion reduced the exciton annihilation [211], in contrast to the saturable exciton emission in more intrinsic samples (Fig. 5.13).

Owning to the large TPL background, the B-exciton emission from indirect infrared absorption was acquired by phase-locking to the intensity modulation of the infrared beam. We verified that the signal was related to hole population and came from pump-induced intervalence band transition by studying its dependence on the delay between the IR and visible pulse (Fig. 5.14). The initial peak had fast decay unresolvable with our current pulse duration, which possibly came from the nonlinear scattering of excited excitons. The following dynamics also agreed with previous report on excitons measured by pump-probe technique [212].

We then determined the optical spin-orbital-coupling strength λ around K point through the two-dimensional spectrum of SFG. Since the photon energy of the visible pump is higher

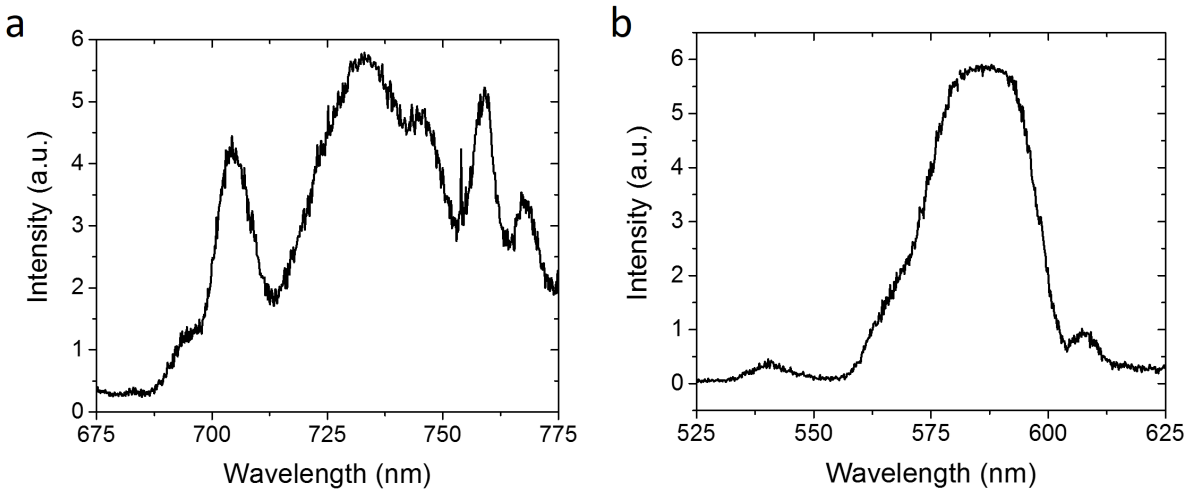

Figure 5.12: (a) The one-photon and (b) two-photon luminescence of WSe_2 under pulsed excitation around 650 nm.

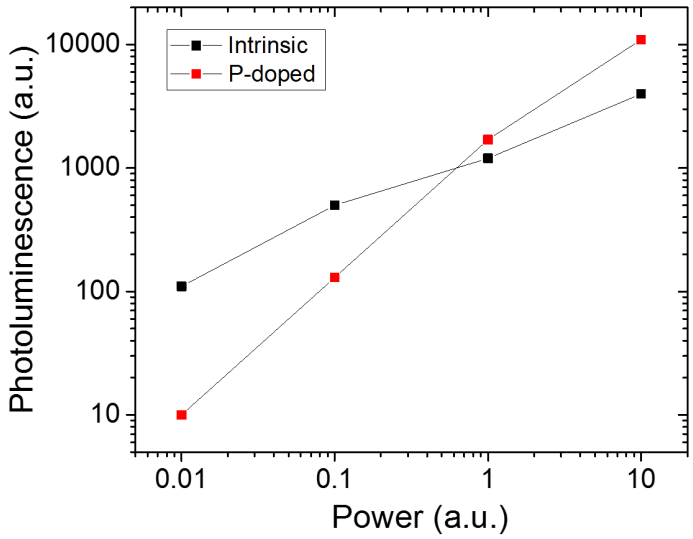

Figure 5.13: The power dependence of photoluminescence of intrinsic and p-doped CVD WSe_2 under continuous-wave excitation at 473 nm. The emission of the intrinsic sample mainly came from exciton that peaked at 750 nm, while the emission of the doped sample came from trion that peaked at 765 nm.

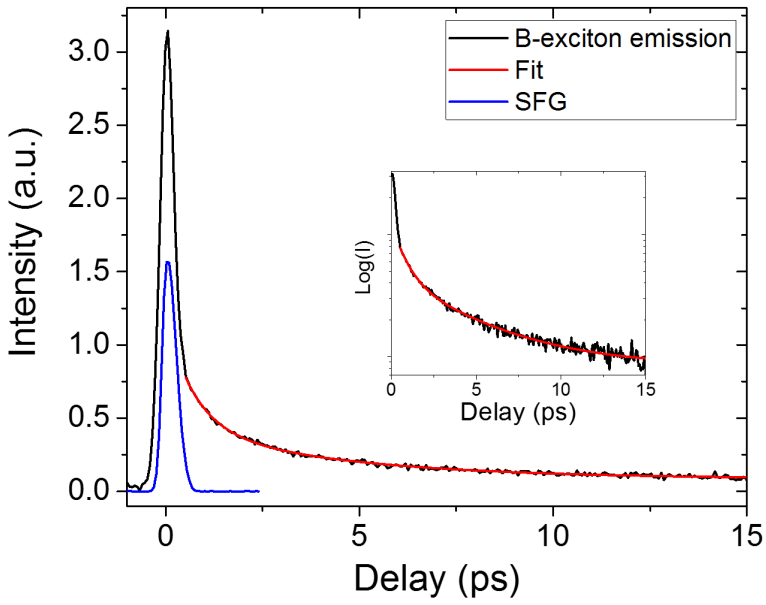

Figure 5.14: The dynamics of transient infrared absorption in CVD WSe_2 pumped with 50 $\mu J/cm^2$ at 650 nm (1.91 eV) and probed at 550 meV. The temporal resolution of 300 fs was obtained by sum-frequency generation from the sample. The signal agreed well with the bi-molecular rate equation (red), which also described the evolution of exciton population of WSe_2 in the literature, indicating that the infrared absorption is proportional to the hole density. Inset is the same plot in logarithmic scale.

than the optical band gap, the resonant SFG is slightly off the K point where the direct optical intervalence band transition is allowed. Therefore all the electronic states involved in the SFG could be real. Figure 5.15 shows the two-dimensional mapping of SFG intensity as a function of the infrared photon energy and the sum frequency. The sharp onset along the infrared spectrum (483 meV) was tentatively associated with λ, and the hot lines at the sum-frequency of 2.4 eV was tentatively assigned to parallel electronic band, although further study is necessary.

Finally, the intensity of the photo-induced infrared absorption was mapped around this energy level (Fig. 5.16). To avoid any hot excitonic effect and maintain sufficient signal we fixed the delay time between the infrared pulse and the visible pump pulse to 1.5 ps. Without resolving the polarization, we observed three steps along the IR spectrum and almost no dependence on the sum frequency (i.e. not depending on the visible pump wavelength) in accordance to the theoretical expectation. We found that the acoustic-like phonon mode (15 meV) has much larger electron-phonon coupling strength than the optical-like phonon mode (25 meV, not observed). In addition, we verified that the spin-allowed K-phonon assisted intervalence band absorption was stronger than the spin-forbidden absorption.

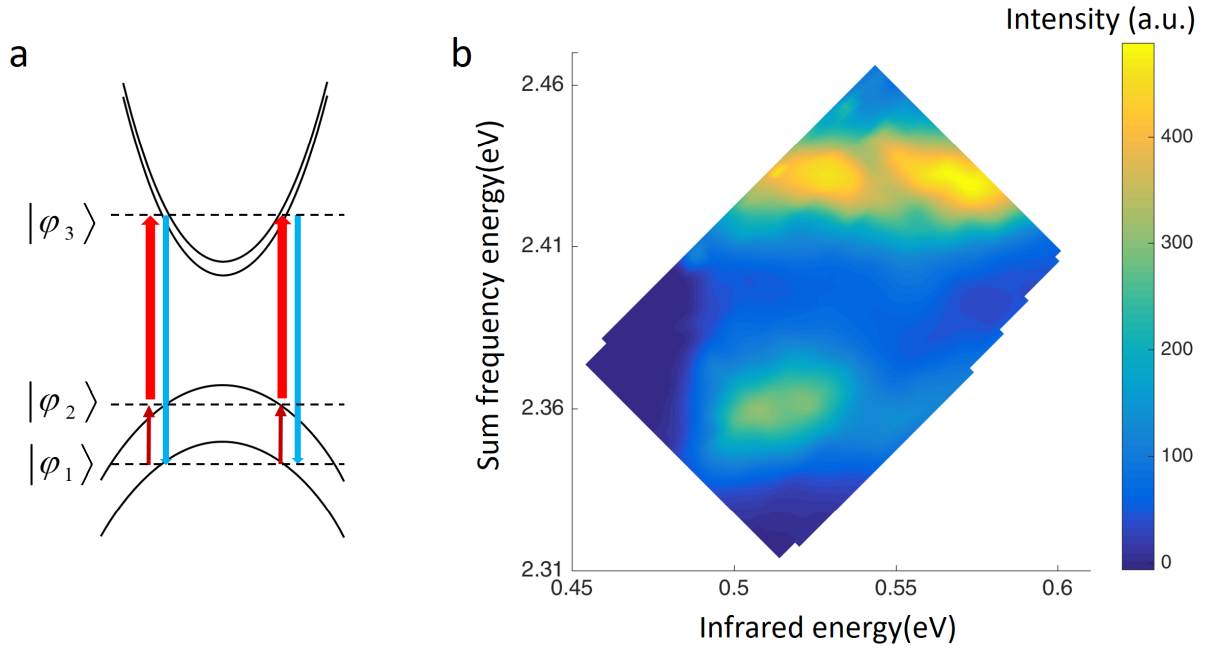

Figure 5.15: (a) Hypothetical diagram of the resonant sum frequency generation (SFG)near the K and K' valley in WSe_2. (b) The dependence of SFG intensity on the infrared photon energy and the sum frequency energy.

5.7 Summary and future work

In summary, we observed the valley phonon in monolayer WSe_2. The phonon energy was measured by both Raman scattering and indirect infrared absorption. We demonstrated the transient infrared spectroscopy based on B-exciton emission and would continue to measure the phononic angular momentum by implementing the circular polarization components. The valley degree of freedom hosted in phonon can potentially be applied for energy efficient valley computing and utilized to control the electronic valley polarization. The intrinsic magnetic moment and the breaking of time-reversal symmetry of valley polarized phonon will potentially expand the idea of mechanically induced non-reciprocity into THz regime [213].

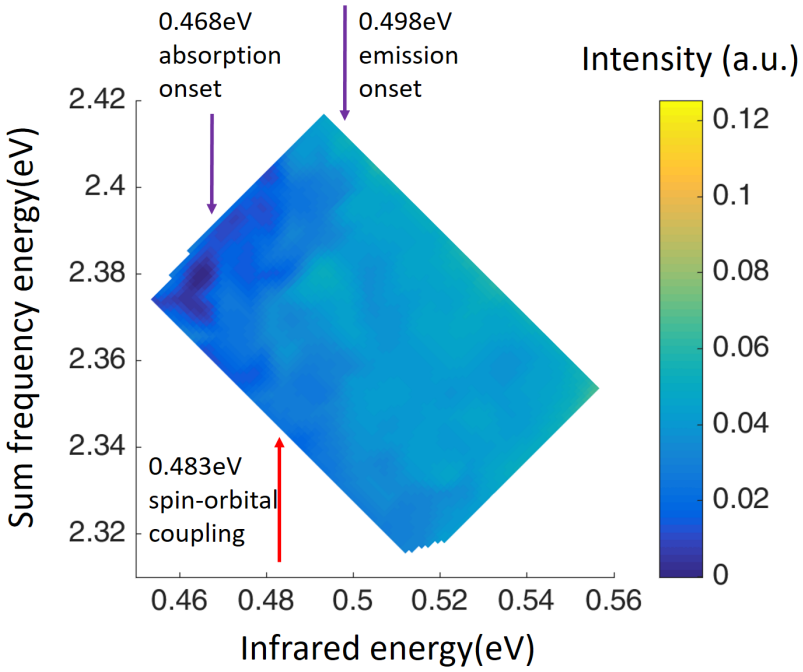

Figure 5.16: Two-dimensional spectrum of the photo-induced infrared absorption as a function of infrared and sum frequency photon energy. The red and purple arrows point to the steps along the infrared photon energy corresponding to the emission/absorption of K-phonon and the direct-optical/Γ-phonon process.

Chapter 6

Conclusion and Outlook

This thesis presented experimental investigation in the emerging field of two-dimensional electromechanical and optomechanical coupling in both quasi-static and high-frequency regime. We demonstrated with monolayer transition metal dichalcogenides (TMDC) that both in-plane and out-of-plane piezoelectricity intrinsically exist in the two-dimensional (2D) limit. The measurement of strain-induced phonon softening casted insight into the phonon anharmonicity and provided reference gauge to strain engineering in the future. The valley-phonon-assisted optical transition in TMDC is a promising approach to reveal the chirality of lattice vibration and develop an energy-efficient valley carrier. So far, our works and concurrent literature from many other research groups have only focused on a few basic properties in this field despite of long-existing theoretical interest, and mechanical devices based on 2D materials remain primitive during the years [214]. In the rest of the chapter we point out some challenges and attempt to propose some future directions among many research opportunities awaiting exploration.

6.1 Fundamental properties of mechanical coupling

The sensitivity of 2D materials to the environment presents both experimental challenge and abundant research topics. Take the measurement of piezoelectricity as an example, free-standing devices are not only difficult to fabricate but also chemically and mechanically fragile, leading to low yield and limited lifetime. On the other hand, experimental evidence showed that substrate can create and/or enhance piezoelectric coupling and place the materials closer to application [128, 215, 216]. Therefore a very attractive subject is to characterize and manipulate the piezoelectricity in 2D materials with *in situ* chemical dressing or electric gating. In addition, both the phonon frequency and the electron-phonon coupling in TMDC depend on carrier density [217]. Thus we expect that their elasticity is also tunable as in graphene [218], as well as the intervalence band transition. Finally, with recent progress in time-resolved transmission electron microscopy and scanning tunneling microscopy it is now possible to study the optomechanical and electromechanical coupling in 2D materials with

atomic resolution [219–221].

6.2 Engineering two-dimensional materials

Strain engineering of 2D materials generated rich physical phenomena such as band gap tuning and piezoresistivity in the past few years [147, 222–226]. However, the mechanical strength of the materials limits the global tensile strain to $\sim 3\%$. Although scanning-probe-based techniques can apply and sense local property changes with substantially higher strain [64, 227, 228], the available experimental techniques to study such small areas in ambient condition are very limited. On the other hand, applying compressive hydrostatic strain is straight-forward and insensitive to the mechanical properties of the sample. Pressure engineering was demonstrated as a powerful tool to change band gap in TMDC to the extent of inducing insulator-metal transition [229–231] and phonon renormalization in artificial structures [232]. We envision that two types of development would be promising. One is the study of monolayers in two-dimensional limit because the tunability in all previous studies of bulk TMDC came primarily from interlayer coupling and sliding, which masked the intrinsic change within the 2D electrons and lattice. The other is the effective hybridization of functional 2D materials assembled in heterostructures under pressure, that will open a much broader area beyond the natural species of layered materials.

6.3 Ultrafast nanomechanics and device applications

The significance of many 2D devices is based on their flexibility for wearable electronics and human interface applications [233]. The mechanical scaling law not only works for flexural rigidity ($\sim d^3$) but also the bulk resonance frequency ($\sim d^{-1}$). The quality factor of the nano-resonator is restricted only by the intrinsic anharmonicity (Grüneisen parameter γ) of the materials and the frequency f [234]:

$$Q = \frac{2\rho c^3}{\pi^2 \gamma^2 C_v T} \frac{1}{f} \tag{6.1}$$

where ρ, c, C_v and T are the density, sound velocity, heat capacitance and temperature, respectively. Thus the resonance remains well-defined at the optical phonon frequency even at room temperature, which is consistent with the sharp Raman peaks in single-crystalline semiconductor TMDC ($Q >$100). At such high frequency ($\sim$THz) the conventional terms in micro-electromechanical systems (NEMS) like capacitive coupling and piezoelectric actuation must be replaced by near-field radiative coupling and infrared-active phonon. The gap between this two regimes is closing in some solid state applications like laser cooling [235–237] and stimulated amplification [19, 238] where the involvement of both the acoustic and optical phonons were demonstrated. It is an open question whether such paradigm shift will have an impact on the state-of-the-art optomechanics and optoelectronics.

Bibliography

1. Wei, L., Kuo, P. K., Thomas, R. L., Anthony, T. R. & Banholzer, W. F. Thermal conductivity of isotopically modified single crystal diamond. *Physical Review Letters* **70,** 3764–3767 (June 14, 1993).
2. Schaffler, F. High-mobility Si and Ge structures. *Semiconductor Science and Technology* **12,** 1515. ISSN: 0268-1242 (1997).
3. Chu, C. W. *et al.* Superconductivity above 150 K in HgBa2Ca2Cu3O8 at high pressures. *Nature* **365,** 323–325. ISSN: 0028-0836 (Sept. 23, 1993).
4. Drozdov, A. P., Eremets, M. I., Troyan, I. A., Ksenofontov, V. & Shylin, S. I. Conventional superconductivity at 203 kelvin at high pressures in the sulfur hydride system. *Nature* **525,** 73–76. ISSN: 0028-0836 (Sept. 3, 2015).
5. Griffith, A. A. The Phenomena of Rupture and Flow in Solids. *Philosophical Transactions of the Royal Society of London A: Mathematical, Physical and Engineering Sciences* **221,** 163–198. ISSN: 1364-503X, 1471-2962 (Jan. 1, 1921).
6. Zhu, T. & Li, J. Ultra-strength materials. *Progress in Materials Science* **55,** 710–757. ISSN: 0079-6425 (Sept. 2010).
7. Ghani, T. *et al. A 90nm high volume manufacturing logic technology featuring novel 45nm gate length strained silicon CMOS transistors* in *Electron Devices Meeting, 2003. IEDM '03 Technical Digest. IEEE International* Electron Devices Meeting, 2003. IEDM '03 Technical Digest. IEEE International (Dec. 2003), 11.6.1–11.6.3. doi:10.1109/IEDM.2003.1269442.
8. Damodaran, A. R. *et al.* New modalities of strain-control of ferroelectric thin films. *Journal of Physics: Condensed Matter* **28,** 263001. ISSN: 0953-8984 (2016).
9. Majumdar, A. Microscale Heat Conduction in Dielectric Thin Films. *Journal of Heat Transfer* **115,** 7–16. ISSN: 0022-1481 (Feb. 1, 1993).
10. DiSalvo, F. J. Thermoelectric Cooling and Power Generation. *Science* **285,** 703–706. ISSN: 0036-8075, 1095-9203 (July 30, 1999).
11. Boukai, A. I. *et al.* Silicon nanowires as efficient thermoelectric materials. *Nature* **451,** 168–171. ISSN: 0028-0836 (Jan. 10, 2008).

12. Stillman, G. E., Wolfe, C. M. & Dimmock, J. O. Hall coefficient factor for polar mode scattering in n-type GaAs. *Journal of Physics and Chemistry of Solids* **31,** 1199–1204. ISSN: 0022-3697 (June 1, 1970).

13. Kittel, C. *Quantum Theory of Solids* 2nd Revised Edition. 528 pp. ISBN: 978-0-471-62412-7. (2016) (Wiley, 1987).

14. Bardeen, J., Cooper, L. N. & Schrieffer, J. R. Microscopic Theory of Superconductivity. *Physical Review* **106,** 162–164 (Apr. 1, 1957).

15. Kohn, W. Image of the Fermi Surface in the Vibration Spectrum of a Metal. *Physical Review Letters* **2,** 393–394 (May 1, 1959).

16. Gasparovic, R. F., Taylor, B. N. & Eck, R. E. Temperature dependence of the superconducting energy gap of Pb. *Solid State Communications* **4,** 59–63. ISSN: 0038-1098 (Jan. 1, 1966).

17. Aynajian, P. *et al.* Energy Gaps and Kohn Anomalies in Elemental Superconductors. *Science* **319,** 1509–1512. ISSN: 0036-8075, 1095-9203 (Mar. 14, 2008).

18. Eichenfield, M., Chan, J., Camacho, R. M., Vahala, K. J. & Painter, O. Optomechanical crystals. *Nature* **462,** 78–82. ISSN: 0028-0836 (Nov. 5, 2009).

19. Rong, H. *et al.* A continuous-wave Raman silicon laser. *Nature* **433,** 725–728. ISSN: 0028-0836 (Feb. 17, 2005).

20. Frisch, D. H. & Smith, J. H. Measurement of the Relativistic Time Dilation Using mu-Mesons. *American Journal of Physics* **31,** 342–355. ISSN: 0002-9505, 1943-2909 (May 1, 1963).

21. Taylor, J. H., Fowler, L. A. & McCulloch, P. M. Measurements of general relativistic effects in the binary pulsar PSR1913 + 16. *Nature* **277,** 437–440. ISSN: 0028-0836 (Feb. 8, 1979).

22. Mermin, N. D. Crystalline Order in Two Dimensions. *Physical Review* **176,** 250–254 (Dec. 5, 1968).

23. Varma, C. M. & Simons, A. L. Strong-Coupling Theory of Charge-Density-Wave Transitions. *Physical Review Letters* **51,** 138–141 (July 11, 1983).

24. Weber, F. *et al.* Extended Phonon Collapse and the Origin of the Charge-Density Wave in 2H-NbSe2. *Physical Review Letters* **107,** 107403 (Sept. 1, 2011).

25. Wilson, J. A., Salvo, F. J. D. & Mahajan, S. Charge-density waves and superlattices in the metallic layered transition metal dichalcogenides. *Advances in Physics* **24,** 117–201. ISSN: 0001-8732 (Mar. 1, 1975).

26. Abrahams, E., Kravchenko, S. V. & Sarachik, M. P. Metallic behavior and related phenomena in two dimensions. *Reviews of Modern Physics* **73,** 251–266 (Mar. 14, 2001).

27. Ohtomo, A. & Hwang, H. Y. A high-mobility electron gas at the LaAlO3/SrTiO3 heterointerface. *Nature* **427,** 423–426. ISSN: 0028-0836 (Jan. 29, 2004).

28. Klitzing, K. v., Dorda, G. & Pepper, M. New Method for High-Accuracy Determination of the Fine-Structure Constant Based on Quantized Hall Resistance. *Physical Review Letters* **45,** 494–497 (Aug. 11, 1980).

29. Koenig, M. *et al.* Quantum Spin Hall Insulator State in HgTe Quantum Wells. *Science* **318,** 766–770. ISSN: 0036-8075, 1095-9203 (Nov. 2, 2007).

30. Oberlin, A., Endo, M. & Koyama, T. Filamentous growth of carbon through benzene decomposition. *Journal of Crystal Growth* **32,** 335–349. ISSN: 0022-0248 (Mar. 1, 1976).

31. Yu, Q. *et al.* Graphene segregated on Ni surfaces and transferred to insulators. *Applied Physics Letters* **93,** 113103. ISSN: 0003-6951, 1077-3118 (Sept. 15, 2008).

32. Lee, Y.-H. *et al.* Synthesis of Large-Area MoS2 Atomic Layers with Chemical Vapor Deposition. *Advanced Materials* **24,** 2320–2325. ISSN: 1521-4095 (May 2, 2012).

33. Zhao, M. *et al.* Large-scale chemical assembly of atomically thin transistors and circuits. *Nature Nanotechnology* **advance online publication.** ISSN: 1748-3387. doi:10.1038/nnano.2016.115. <http://www.nature.com/nnano/journal/vaop/ncurrent/full/nnano.2016.115.html> (2016) (July 11, 2016).

34. Novoselov, K. S. *et al.* Electric Field Effect in Atomically Thin Carbon Films. *Science* **306,** 666–669. ISSN: 0036-8075, 1095-9203 (Oct. 22, 2004).

35. Ugeda, M. M. *et al.* Characterization of collective ground states in single-layer NbSe2. *Nature Physics* **12,** 92–97. ISSN: 1745-2473 (Jan. 2016).

36. Lee, J. *et al.* Imaging electrostatically confined Dirac fermions in graphene quantum dots. *Nature Physics* **12,** 1032–1036. ISSN: 1745-2473 (Nov. 2016).

37. Wilson, J. A. & Yoffe, A. D. The transition metal dichalcogenides discussion and interpretation of the observed optical, electrical and structural properties. *Advances in Physics* **18,** 193–335. ISSN: 0001-8732 (May 1, 1969).

38. Miro, P., Audiffred, M. & Heine, T. An atlas of two-dimensional materials. **43,** 6537–6554. ISSN: 1460-4744 (Aug. 18, 2014).

39. Geim, A. K. & Grigorieva, I. V. Van der Waals heterostructures. *Nature* **499,** 419–425. ISSN: 0028-0836 (July 25, 2013).

40. Withers, F. *et al.* Light-emitting diodes by band-structure engineering in van der Waals heterostructures. *Nature Materials* **14,** 301–306. ISSN: 1476-1122 (Mar. 2015).

41. Novoselov, K. S., Mishchenko, A., Carvalho, A. & Neto, A. H. C. 2D materials and van der Waals heterostructures. *Science* **353,** aac9439. ISSN: 0036-8075, 1095-9203 (July 29, 2016).

42. Novoselov, K. S. *et al.* Two-dimensional atomic crystals. *Proceedings of the National Academy of Sciences of the United States of America* **102,** 10451–10453. ISSN: 0027-8424, 1091-6490 (July 26, 2005).
43. Wallace, P. R. The Band Theory of Graphite. *Physical Review* **71,** 622–634 (May 1, 1947).
44. Castro Neto, A. H., Guinea, F., Peres, N. M. R., Novoselov, K. S. & Geim, A. K. The electronic properties of graphene. *Reviews of Modern Physics* **81,** 109–162 (Jan. 14, 2009).
45. Bonaccorso, F., Sun, Z., Hasan, T. & Ferrari, A. C. Graphene photonics and optoelectronics. *Nature Photonics* **4,** 611–622. ISSN: 1749-4885 (Sept. 2010).
46. Bae, S. *et al.* Roll-to-roll production of 30-inch graphene films for transparent electrodes. *Nature Nanotechnology* **5,** 574–578. ISSN: 1748-3387 (Aug. 2010).
47. Liu, M. *et al.* A graphene-based broadband optical modulator. *Nature* **474,** 64–67. ISSN: 0028-0836 (June 2, 2011).
48. Ross, J. S. *et al.* Electrically tunable excitonic light-emitting diodes based on monolayer WSe2 p-n junctions. *Nature Nanotechnology* **9,** 268–272. ISSN: 1748-3387 (Apr. 2014).
49. Pospischil, A., Furchi, M. M. & Mueller, T. Solar-energy conversion and light emission in an atomic monolayer p-n diode. *Nature Nanotechnology* **9,** 257–261. ISSN: 1748-3387 (Apr. 2014).
50. Baugher, B. W. H., Churchill, H. O. H., Yang, Y. & Jarillo-Herrero, P. Optoelectronic devices based on electrically tunable p-n diodes in a monolayer dichalcogenide. *Nature Nanotechnology* **9,** 262–267. ISSN: 1748-3387 (Apr. 2014).
51. Ye, Y. *et al.* Monolayer excitonic laser. *Nature Photonics* **9,** 733–737. ISSN: 1749-4885 (Nov. 2015).
52. Wu, S. *et al.* Monolayer semiconductor nanocavity lasers with ultralow thresholds. *Nature* **520,** 69–72. ISSN: 0028-0836 (Apr. 2, 2015).
53. Salehzadeh, O., Djavid, M., Tran, N. H., Shih, I. & Mi, Z. Optically Pumped Two-Dimensional MoS2 Lasers Operating at Room-Temperature. *Nano Letters* **15,** 5302–5306. ISSN: 1530-6984 (Aug. 12, 2015).
54. Ye, Z. *et al.* Probing excitonic dark states in single-layer tungsten disulphide. *Nature* **513,** 214–218. ISSN: 0028-0836 (Sept. 11, 2014).
55. Zhu, B., Chen, X. & Cui, X. Exciton Binding Energy of Monolayer WS2. *Scientific Reports* **5,** 9218. ISSN: 2045-2322 (Mar. 18, 2015).
56. Ugeda, M. M. *et al.* Giant bandgap renormalization and excitonic effects in a monolayer transition metal dichalcogenide semiconductor. *Nature Materials* **13,** 1091–1095. ISSN: 1476-1122 (Dec. 2014).

57. Mak, K. F. *et al.* Tightly bound trions in monolayer MoS2. *Nature Materials* **12,** 207–211. ISSN: 1476-1122 (Mar. 2013).

58. Palummo, M., Bernardi, M. & Grossman, J. C. Exciton Radiative Lifetimes in Two-Dimensional Transition Metal Dichalcogenides. *Nano Letters* **15,** 2794–2800. ISSN: 1530-6984 (May 13, 2015).

59. Robert, C. *et al.* Exciton radiative lifetime in transition metal dichalcogenide monolayers. *Physical Review B* **93,** 205423 (May 12, 2016).

60. Ye, J. T. *et al.* Superconducting Dome in a Gate-Tuned Band Insulator. *Science* **338,** 1193–1196. ISSN: 0036-8075, 1095-9203 (Nov. 30, 2012).

61. Li, L. J. *et al.* Controlling many-body states by the electric-field effect in a two-dimensional material. *Nature* **529,** 185–189. ISSN: 0028-0836 (Jan. 14, 2016).

62. Ross, J. S. *et al.* Electrical control of neutral and charged excitons in a monolayer semiconductor. *Nature Communications* **4,** 1474. ISSN: 2041-1723 (Feb. 12, 2013).

63. Seyler, K. L. *et al.* Electrical control of second-harmonic generation in a WSe2 monolayer transistor. *Nature Nanotechnology* **10,** 407–411. ISSN: 1748-3387 (May 2015).

64. Lee, C., Wei, X., Kysar, J. W. & Hone, J. Measurement of the Elastic Properties and Intrinsic Strength of Monolayer Graphene. *Science* **321,** 385–388. ISSN: 0036-8075, 1095-9203 (July 18, 2008).

65. Feng, J., Qian, X., Huang, C.-W. & Li, J. Strain-engineered artificial atom as a broad-spectrum solar energy funnel. *Nature Photonics* **6,** 866–872. ISSN: 1749-4885 (Dec. 2012).

66. Xi, X. *et al.* Strongly enhanced charge-density-wave order in monolayer NbSe2. *Nature Nanotechnology* **10,** 765–769. ISSN: 1748-3387 (Sept. 2015).

67. Zhu, H. *et al.* Observation of piezoelectricity in free-standing monolayer MoS2. *Nature Nanotechnology* **10,** 151–155. ISSN: 1748-3387 (Feb. 2015).

68. Lu, A.-Y., Zhu, H., Xiao, J., Li, L.-J. & Zhang, X. Janus atomic monolayers of transition metal dichalcogenides. *Unpublished.*

69. Zhu, H., Alsaid, Y. & Zhang, X. Phonon-softening and anisotropy by strain in molybdenum ditelluride. *Unpublished.*

70. Zhu, H., Xiao, J., Kaindl, R. A. & Zhang, X. Two-dimensional chiral phonon. *Unpublished.*

71. Valasek, J. Piezo-Electric and Allied Phenomena in Rochelle Salt. *Physical Review* **17,** 475–481 (Apr. 1, 1921).

72. Shirane, G., Hoshino, S. & Suzuki, K. X-Ray Study of the Phase Transition in Lead Titanate. *Physical Review* **80,** 1105–1106 (Dec. 15, 1950).

73. Yang, J. *Analysis of Piezoelectric Devices* ISBN: 978-981-277-318-0. (2016) (WSPC, River Edge, US, 2006).

74. Luo, Y. *et al.* Nanoshell tubes of ferroelectric lead zirconate titanate and barium titanate. *Applied Physics Letters* **83,** 440–442. ISSN: 0003-6951, 1077-3118 (July 21, 2003).

75. Wang, Z. L. & Song, J. Piezoelectric Nanogenerators Based on Zinc Oxide Nanowire Arrays. *Science* **312,** 242–246. ISSN: 0036-8075, 1095-9203 (Apr. 14, 2006).

76. Nguyen, T. D. *et al.* Piezoelectric nanoribbons for monitoring cellular deformations. *Nature Nanotechnology* **7,** 587–593. ISSN: 1748-3387 (Sept. 2012).

77. Sai, N. & Mele, E. J. Microscopic theory for nanotube piezoelectricity. *Physical Review B* **68,** 241405 (Dec. 31, 2003).

78. Quan, X., Marvin, C. W., Seebald, L. & Hutchison, G. R. Single-Molecule Piezoelectric Deformation: Rational Design from First-Principles Calculations. *The Journal of Physical Chemistry C* **117,** 16783–16790. ISSN: 1932-7447 (Aug. 22, 2013).

79. Xiang, H. J., Yang, J., Hou, J. G. & Zhu, Q. Piezoelectricity in ZnO nanowires: A first-principles study. *Applied Physics Letters* **89,** 223111. ISSN: 0003-6951, 1077-3118 (Nov. 27, 2006).

80. Li, S. *et al.* Size effects in nanostructured ferroelectrics. *Physics Letters A* **212,** 341–346. ISSN: 0375-9601 (Apr. 8, 1996).

81. Bune, A. V. *et al.* Two-dimensional ferroelectric films. *Nature* **391,** 874–877. ISSN: 0028-0836 (Feb. 26, 1998).

82. Duerloo, K.-A. N., Ong, M. T. & Reed, E. J. Intrinsic Piezoelectricity in Two-Dimensional Materials. *The Journal of Physical Chemistry Letters* **3,** 2871–2876. ISSN: 1948-7185 (Oct. 4, 2012).

83. Park, S.-E. & Shrout, T. R. Ultrahigh strain and piezoelectric behavior in relaxor based ferroelectric single crystals. *Journal of Applied Physics* **82,** 1804–1811. ISSN: 0021-8979, 1089-7550 (Aug. 15, 1997).

84. Young, R., Ward, J. & Scire, F. The Topografiner: An Instrument for Measuring Surface Microtopography. *Review of Scientific Instruments* **43,** 999–1011. ISSN: 0034-6748, 1089-7623 (July 1, 1972).

85. Binnig, G. & Rohrer, H. Scanning tunneling microscopy. *Surface Science* **126,** 236–244. ISSN: 0039-6028 (Mar. 2, 1983).

86. Binnig, G., Quate, C. F. & Gerber, C. Atomic Force Microscope. *Physical Review Letters* **56,** 930–933 (Mar. 3, 1986).

87. Franke, K., Besold, J., Haessler, W. & Seegebarth, C. Modification and detection of domains on ferroelectric PZT films by scanning force microscopy. *Surface Science* **302,** L283–L288. ISSN: 0039-6028 (Jan. 20, 1994).

88. Kalinin, S. V., Karapetian, E. & Kachanov, M. Nanoelectromechanics of piezoresponse force microscopy. *Physical Review B* **70,** 184101 (Nov. 1, 2004).

89. Saurenbach, F. & Terris, B. D. Imaging of ferroelectric domain walls by force microscopy. *Applied Physics Letters* **56,** 1703–1705. ISSN: 0003-6951, 1077-3118 (Apr. 23, 1990).

90. Hong, S. *et al.* Principle of ferroelectric domain imaging using atomic force microscope. *Journal of Applied Physics* **89,** 1377–1386. ISSN: 0021-8979, 1089-7550 (Jan. 15, 2001).

91. Kalinin, S. V., Jesse, S., Tselev, A., Baddorf, A. P. & Balke, N. The Role of Electrochemical Phenomena in Scanning Probe Microscopy of Ferroelectric Thin Films. *ACS Nano* **5,** 5683–5691. ISSN: 1936-0851 (July 26, 2011).

92. Kim, Y. *et al.* Nonlinear Phenomena in Multiferroic Nanocapacitors: Joule Heating and Electromechanical Effects. *ACS Nano* **5,** 9104–9112. ISSN: 1936-0851 (Nov. 22, 2011).

93. Wang, Z., Hu, J., Suryavanshi, A. P., Yum, K. & Yu, M.-F. Voltage Generation from Individual BaTiO3 Nanowires under Periodic Tensile Mechanical Load. *Nano Letters* **7,** 2966–2969. ISSN: 1530-6984 (Oct. 1, 2007).

94. Wu, W. *et al.* Piezoelectricity of single-atomic-layer MoS2 for energy conversion and piezotronics. *Nature* **514,** 470–474. ISSN: 0028-0836 (Oct. 23, 2014).

95. Levinzon, F. A. Noise of piezoelectric accelerometer with integral FET amplifier. *IEEE Sensors Journal* **5,** 1235–1242. ISSN: 1530-437X (Dec. 2005).

96. Minary-Jolandan, M., Bernal, R. A., Kuljanishvili, I., Parpoil, V. & Espinosa, H. D. Individual GaN Nanowires Exhibit Strong Piezoelectricity in 3D. *Nano Letters* **12,** 970–976. ISSN: 1530-6984 (Feb. 8, 2012).

97. Pan, J. Y., Lin, P., Maseeh, F. & Senturia, S. D. *Verification of FEM analysis of load-deflection methods for measuring mechanical properties of thin films* in *, IEEE Solid-State Sensor and Actuator Workshop, 1990. 4th Technical Digest* , IEEE Solid-State Sensor and Actuator Workshop, 1990. 4th Technical Digest (June 1990), 70–73. doi:10.1109/SOLSEN.1990.109823.

98. Wan, K.-T., Guo, S. & Dillard, D. A. A theoretical and numerical study of a thin clamped circular film under an external load in the presence of a tensile residual stress. *Thin Solid Films* **425,** 150–162. ISSN: 0040-6090 (Feb. 3, 2003).

99. Kalinin, S. V. *et al.* Nanoscale Electromechanics of Ferroelectric and Biological Systems: A New Dimension in Scanning Probe Microscopy. *Annual Review of Materials Research* **37,** 189–238 (2007).

100. Splendiani, A. *et al.* Emerging Photoluminescence in Monolayer MoS2. *Nano Letters* **10,** 1271–1275. ISSN: 1530-6984 (Apr. 14, 2010).

101. Lee, C. *et al.* Anomalous Lattice Vibrations of Single- and Few-Layer MoS2. *ACS Nano* **4,** 2695–2700. ISSN: 1936-0851 (May 25, 2010).

102. Li, Y. *et al.* Probing Symmetry Properties of Few-Layer MoS2 and h-BN by Optical Second-Harmonic Generation. *Nano Letters* **13,** 3329–3333. ISSN: 1530-6984 (July 10, 2013).

103. Yin, X. *et al.* Edge Nonlinear Optics on a MoS2 Atomic Monolayer. *Science* **344,** 488–490. ISSN: 0036-8075, 1095-9203 (May 2, 2014).

104. Yang, J. K. W. & Berggren, K. K. Using high-contrast salty development of hydrogen silsesquioxane for sub-10-nm half-pitch lithography. *Journal of Vacuum Science & Technology B* **25,** 2025–2029. ISSN: 2166-2746, 2166-2754 (Nov. 1, 2007).

105. Bertolazzi, S., Brivio, J. & Kis, A. Stretching and Breaking of Ultrathin MoS2. *ACS Nano* **5,** 9703–9709. ISSN: 1936-0851 (Dec. 27, 2011).

106. Helveg, S. *et al.* Atomic-Scale Structure of Single-Layer MoS2 Nanoclusters. *Physical Review Letters* **84,** 951–954 (Jan. 31, 2000).

107. Van der Zande, A. M. *et al.* Grains and grain boundaries in highly crystalline monolayer molybdenum disulphide. *Nature Materials* **12,** 554–561. ISSN: 1476-1122 (June 2013).

108. Naumov, I., Bratkovsky, A. M. & Ranjan, V. Unusual Flexoelectric Effect in Two-Dimensional Noncentrosymmetric sp2-Bonded Crystals. *Physical Review Letters* **102,** 217601 (May 26, 2009).

109. Lopez-Suarez, M., Pruneda, M., Abadal, G. & Rurali, R. Piezoelectric monolayers as nonlinear energy harvesters. *Nanotechnology* **25,** 175401. ISSN: 0957-4484 (2014).

110. Ishizaka, K. *et al.* Giant Rashba-type spin splitting in bulk BiTeI. *Nature Materials* **10,** 521–526. ISSN: 1476-1122 (July 2011).

111. Tasker, P. W. The stability of ionic crystal surfaces. *Journal of Physics C: Solid State Physics* **12,** 4977. ISSN: 0022-3719 (1979).

112. Freeman, C. L., Claeyssens, F., Allan, N. L. & Harding, J. H. Graphitic Nanofilms as Precursors to Wurtzite Films: Theory. *Physical Review Letters* **96,** 066102 (Feb. 13, 2006).

113. Tusche, C., Meyerheim, H. L. & Kirschner, J. Observation of Depolarized ZnO(0001) Monolayers: Formation of Unreconstructed Planar Sheets. *Physical Review Letters* **99,** 026102 (July 13, 2007).

114. Zhang, L. *et al.* Janus graphene from asymmetric two-dimensional chemistry. *Nature Communications* **4,** 1443 (Feb. 5, 2013).

115. Manchon, A., Koo, H. C., Nitta, J., Frolov, S. M. & Duine, R. A. New perspectives for Rashba spin-orbit coupling. *Nature Materials* **14,** 871–882. ISSN: 1476-1122 (Sept. 2015).

116. Cheng, Y. C., Zhu, Z. Y., Tahir, M. & Schwingenschlogl, U. Spin-orbit–induced spin splittings in polar transition metal dichalcogenide monolayers. *EPL (Europhysics Letters)* **102,** 57001. ISSN: 0295-5075 (2013).

117. Cheng, C., Sun, J.-T., Chen, X.-R., Fu, H.-X. & Meng, S. Nonlinear Rashba spin splitting in transition metal dichalcogenide monolayers. *Nanoscale* **8,** 17854–17860 (2016).

118. Paxton, W. F. *et al.* Catalytic Nanomotors: Autonomous Movement of Striped Nanorods. *Journal of the American Chemical Society* **126,** 13424–13431. ISSN: 0002-7863 (Oct. 1, 2004).

119. Cobo, S. *et al.* A Janus cobalt-based catalytic material for electro-splitting of water. *Nature Materials* **11,** 802–807. ISSN: 1476-1122 (Sept. 2012).

120. Aroyo, M. I. *et al.* Crystallography online: Bilbao Crystallographic Server. *Bulgarian Chemical Communications* **43.** WOS:000292661600002, 183–197. ISSN: 0324-1130 (2011).

121. Rodrigues, G. d. C. *et al.* Strong piezoelectricity in single-layer graphene deposited on SiO2 grating substrates. *Nature Communications* **6,** 7572. ISSN: 2041-1723 (June 25, 2015).

122. Rabe, U., Janser, K. & Arnold, W. Vibrations of free and surface-coupled atomic force microscope cantilevers: Theory and experiment. *Review of Scientific Instruments* **67,** 3281–3293. ISSN: 0034-6748, 1089-7623 (Sept. 1, 1996).

123. Harnagea, C., Alexe, M., Hesse, D. & Pignolet, A. Contact resonances in voltage-modulated force microscopy. *Applied Physics Letters* **83,** 338–340. ISSN: 0003-6951, 1077-3118 (July 14, 2003).

124. Jesse, S., Mirman, B. & Kalinin, S. V. Resonance enhancement in piezoresponse force microscopy: Mapping electromechanical activity, contact stiffness, and Q factor. *Applied Physics Letters* **89,** 022906. ISSN: 0003-6951, 1077-3118 (July 10, 2006).

125. Rodriguez, B. J., Callahan, C., Kalinin, S. V. & Proksch, R. Dual-frequency resonance-tracking atomic force microscopy. *Nanotechnology* **18,** 475504. ISSN: 0957-4484 (2007).

126. Balke, N. *et al.* Exploring Local Electrostatic Effects with Scanning Probe Microscopy: Implications for Piezoresponse Force Microscopy and Triboelectricity. *ACS Nano* **8,** 10229–10236. ISSN: 1936-0851 (Oct. 28, 2014).

127. Xie, S. *et al.* High resolution quantitative piezoresponse force microscopy of BiFeO3 nanofibers with dramatically enhanced sensitivity. **4,** 408–413. ISSN: 2040-3372 (Jan. 4, 2012).

128. Zelisko, M. *et al.* Anomalous piezoelectricity in two-dimensional graphene nitride nanosheets. *Nature Communications* **5,** 4284 (June 27, 2014).

129. Johann, F., Hoffmann, Á. & Soergel, E. Impact of electrostatic forces in contact-mode scanning force microscopy. *Physical Review B* **81,** 094109 (Mar. 17, 2010).

130. Becher, C. *et al.* Functional ferroic heterostructures with tunable integral symmetry. *Nature Communications* **5,** 4295. ISSN: 2041-1723 (July 2, 2014).

131. Wang, X. B. *et al.* The influence of different doping elements on microstructure, piezoelectric coefficient and resistivity of sputtered ZnO film. *Applied Surface Science* **253,** 1639–1643. ISSN: 0169-4332 (Nov. 30, 2006).

132. Bruesch, D. P. in *Phonons: Theory and Experiments I Springer Series in Solid-State Sciences* 34. DOI: 10.1007/978-3-642-81781-6_5, 152–200 (Springer Berlin Heidelberg, 1982). ISBN: 978-3-642-81783-0. <http://link.springer.com/chapter/10.1007/978-3-642-81781-6_5> (2016).

133. Raman, C. V. A new radiation. *Indian Journal of Physics* **2,** 387–398. ISSN: 0019-5480 (1928).

134. BROCKHOUSE, B. N. & STEWART, A. T. Normal Modes of Aluminum by Neutron Spectrometry. *Reviews of Modern Physics* **30,** 236–249 (Jan. 1, 1958).

135. Khanna, S. K. & Lambe, J. Inelastic Electron Tunneling Spectroscopy. *Science* **220,** 1345–1351. ISSN: 0036-8075, 1095-9203 (June 24, 1983).

136. Zhang, Y. *et al.* Giant phonon-induced conductance in scanning tunnelling spectroscopy of gate-tunable graphene. *Nature Physics* **4,** 627–630. ISSN: 1745-2473 (Aug. 2008).

137. Burkel, E., Peisl, J. & Dorner, B. Observation of Inelastic X-Ray Scattering from Phonons. *EPL (Europhysics Letters)* **3,** 957. ISSN: 0295-5075 (1987).

138. Fleischmann, M., Hendra, P. J. & McQuillan, A. J. Raman spectra of pyridine adsorbed at a silver electrode. *Chemical Physics Letters* **26,** 163–166. ISSN: 0009-2614 (May 15, 1974).

139. Zhang, R. *et al.* Chemical mapping of a single molecule by plasmon-enhanced Raman scattering. *Nature* **498,** 82–86. ISSN: 0028-0836 (June 6, 2013).

140. Emory, S. R. & Nie, S. Near-Field Surface-Enhanced Raman Spectroscopy on Single Silver Nanoparticles. *Analytical Chemistry* **69,** 2631–2635. ISSN: 0003-2700 (July 1, 1997).

141. Casiraghi, C. *et al.* Raman Spectroscopy of Graphene Edges. *Nano Letters* **9,** 1433–1441. ISSN: 1530-6984 (Apr. 8, 2009).

142. Tuinstra, F. & Koenig, J. L. Raman Spectrum of Graphite. *The Journal of Chemical Physics* **53,** 1126–1130. ISSN: 0021-9606, 1089-7690 (Aug. 1, 1970).

143. Das, A. *et al.* Monitoring dopants by Raman scattering in an electrochemically top-gated graphene transistor. *Nature Nanotechnology* **3,** 210–215. ISSN: 1748-3387 (Apr. 2008).

144. Kuball, M. Raman spectroscopy of GaN, AlGaN and AlN for process and growth monitoring/control. *Surface and Interface Analysis* **31,** 987–999. ISSN: 1096-9918 (Oct. 1, 2001).

145. Ager, J. W. & Drory, M. D. Quantitative measurement of residual biaxial stress by Raman spectroscopy in diamond grown on a Ti alloy by chemical vapor deposition. *Physical Review B* **48,** 2601–2607 (July 15, 1993).

146. Huang, M. *et al.* Phonon softening and crystallographic orientation of strained graphene studied by Raman spectroscopy. *Proceedings of the National Academy of Sciences* **106,** 7304–7308. ISSN: 0027-8424, 1091-6490 (May 5, 2009).

147. Conley, H. J. *et al.* Bandgap Engineering of Strained Monolayer and Bilayer MoS2. *Nano Letters* **13,** 3626–3630. ISSN: 1530-6984 (Aug. 14, 2013).

148. Duerloo, K.-A. N., Li, Y. & Reed, E. J. Structural phase transitions in two-dimensional Mo- and W-dichalcogenide monolayers. *Nature Communications* **5,** 4214. ISSN: 2041-1723 (July 1, 2014).

149. Kappera, R. *et al.* Phase-engineered low-resistance contacts for ultrathin MoS2 transistors. *Nature Materials* **13,** 1128–1134. ISSN: 1476-1122 (Dec. 2014).

150. Deng, K. *et al.* Experimental observation of topological Fermi arcs in type-II Weyl semimetal MoTe2. *Nature Physics* **advance online publication.** ISSN: 1745-2473. doi:10.1038/nphys3871. <http://www.nature.com/nphys/journal/vaop/ncurrent/full/nphys3871.html> (2016) (Sept. 5, 2016).

151. Qian, X., Liu, J., Fu, L. & Li, J. Quantum spin Hall effect in two-dimensional transition metal dichalcogenides. *Science* **346,** 1344–1347. ISSN: 0036-8075, 1095-9203 (Dec. 12, 2014).

152. Zhang, W., Huang, Z., Zhang, W. & Li, Y. Two-dimensional semiconductors with possible high room temperature mobility. *Nano Research* **7,** 1731–1737. ISSN: 1998-0124, 1998-0000 (Dec. 1, 2014).

153. Carvalho, B. R., Malard, L. M., Alves, J. M., Fantini, C. & Pimenta, M. A. Symmetry-Dependent Exciton-Phonon Coupling in 2D and Bulk MoS2 Observed by Resonance Raman Scattering. *Physical Review Letters* **114,** 136403 (Apr. 2, 2015).

154. Liu, H.-L. *et al.* Anomalous lattice vibrations of monolayer MoS2 probed by ultraviolet Raman scattering. *Physical Chemistry Chemical Physics* **17,** 14561–14568. ISSN: 1463-9084 (May 27, 2015).

155. Del Corro, E. *et al.* Atypical Exciton–Phonon Interactions in WS2 and WSe2 Monolayers Revealed by Resonance Raman Spectroscopy. *Nano Letters* **16,** 2363–2368. ISSN: 1530-6984 (Apr. 13, 2016).

156. Ruppert, C., Aslan, O. B. & Heinz, T. F. Optical Properties and Band Gap of Single- and Few-Layer MoTe2 Crystals. *Nano Letters* **14,** 6231–6236. ISSN: 1530-6984 (Nov. 12, 2014).

157. Guo, H. *et al.* Double resonance Raman modes in monolayer and few-layer MoTe2. *Physical Review B* **91,** 205415 (May 12, 2015).

158. Song, Q. J. *et al.* Physical origin of Davydov splitting and resonant Raman spectroscopy of Davydov components in multilayer MoTe2. *Physical Review B* **93,** 115409 (Mar. 8, 2016).

159. Chen, S.-Y., Zheng, C., Fuhrer, M. S. & Yan, J. Helicity-Resolved Raman Scattering of MoS2, MoSe2, WS2, and WSe2 Atomic Layers. *Nano Letters* **15,** 2526–2532. ISSN: 1530-6984 (Apr. 8, 2015).

160. Wang, Y., Cong, C., Qiu, C. & Yu, T. Raman Spectroscopy Study of Lattice Vibration and Crystallographic Orientation of Monolayer MoS2 under Uniaxial Strain. *Small* **9,** 2857–2861. ISSN: 1613-6829 (Sept. 9, 2013).

161. Mohiuddin, T. M. G. *et al.* Uniaxial strain in graphene by Raman spectroscopy: G peak splitting, Gruneisen parameters, and sample orientation. *Physical Review B* **79,** 205433 (May 29, 2009).

162. Atkins, P. & Paula, J. d. *Physical Chemistry* 1087 pp. ISBN: 978-0-7167-8759-4 (Macmillan, Mar. 10, 2006).

163. Petrache, C. M. *et al.* Rotational bands in the doubly odd nucleus 134Pr. *Nuclear Physics A* **597,** 106–126. ISSN: 0375-9474 (Jan. 22, 1996).

164. Gupalov, S. V. & Merkulov, I. A. Theory of Raman light scattering by nanocrystal acoustic vibrations. *Physics of the Solid State* **41,** 1349–1358. ISSN: 1063-7834, 1090-6460 (Aug. 1, 1999).

165. Comas, F., Trallero-Giner, C., Studart, N. & Marques, G. E. Interface optical phonons in spheroidal dots: Raman selection rules. *Physical Review B* **65,** 073303 (Jan. 18, 2002).

166. Yafet, Y. *Solid State Physics* 538 pp. ISBN: 978-0-08-086478-5 (Academic Press, Jan. 1, 1963).

167. Koopmans, B. *et al.* Explaining the paradoxical diversity of ultrafast laser-induced demagnetization. *Nature Materials* **9,** 259–265. ISSN: 1476-1122 (Mar. 2010).

168. Nova, T. F. *et al.* An effective magnetic field from optically driven phonons. *Nature Physics* **advance online publication.** ISSN: 1745-2473. doi:10.1038/nphys3925. <http://www.nature.com/nphys/journal/vaop/ncurrent/full/nphys3925.html> (2016) (Oct. 24, 2016).

169. Solano-Carrillo, E. Uncovering the source of the anomaly in the electrical resistivity of ferromagnetic metals around liquid-helium temperatures. *arXiv:1607.04585 [cond-mat].* arXiv: 1607.04585. <http://arxiv.org/abs/1607.04585> (2016) (July 15, 2016).

170. Zhang, L. & Niu, Q. Chiral Phonons at High-Symmetry Points in Monolayer Hexagonal Lattices. *Physical Review Letters* **115,** 115502 (Sept. 11, 2015).

171. Kaplyanskii, A. A., Sokolov, N. S., Novikov, B. V. & Gastev, S. V. Selective optical valley pumping in silicon and germanium. *Solid State Communications* **20,** 27–29. ISSN: 0038-1098 (Oct. 1, 1976).

172. Gunawan, O. *et al.* Spin–valley phase diagram of the two-dimensional metal–insulator transition. *Nature Physics* **3,** 388–391. ISSN: 1745-2473 (June 2007).

173. Isberg, J. *et al.* Generation, transport and detection of valley-polarized electrons in diamond. *Nature Materials* **12,** 760–764. ISSN: 1476-1122 (Aug. 2013).

174. Morpurgo, A. F. & Guinea, F. Intervalley Scattering, Long-Range Disorder, and Effective Time-Reversal Symmetry Breaking in Graphene. *Physical Review Letters* **97,** 196804 (Nov. 9, 2006).

175. Rycerz, A., Tworzydło, J. & Beenakker, C. W. J. Valley filter and valley valve in graphene. *Nature Physics* **3,** 172–175. ISSN: 1745-2473 (Mar. 2007).

176. Xiao, D., Yao, W. & Niu, Q. Valley-Contrasting Physics in Graphene: Magnetic Moment and Topological Transport. *Physical Review Letters* **99,** 236809 (Dec. 7, 2007).

177. Gorbachev, R. V. *et al.* Detecting topological currents in graphene superlattices. *Science* **346,** 448–451. ISSN: 0036-8075, 1095-9203 (Oct. 24, 2014).

178. Shimazaki, Y. *et al.* Generation and detection of pure valley current by electrically induced Berry curvature in bilayer graphene. *Nature Physics* **11,** 1032–1036. ISSN: 1745-2473 (Dec. 2015).

179. Sui, M. *et al.* Gate-tunable topological valley transport in bilayer graphene. *Nature Physics* **11,** 1027–1031. ISSN: 1745-2473 (Dec. 2015).

180. Yao, W., Xiao, D. & Niu, Q. Valley-dependent optoelectronics from inversion symmetry breaking. *Physical Review B* **77,** 235406 (June 4, 2008).

181. Mak, K. F., Lee, C., Hone, J., Shan, J. & Heinz, T. F. Atomically Thin MoS2: A New Direct-Gap Semiconductor. *Physical Review Letters* **105,** 136805 (Sept. 24, 2010).

182. Mak, K. F., He, K., Shan, J. & Heinz, T. F. Control of valley polarization in monolayer MoS2 by optical helicity. *Nature Nanotechnology* **7,** 494–498. ISSN: 1748-3387 (Aug. 2012).

183. Zeng, H., Dai, J., Yao, W., Xiao, D. & Cui, X. Valley polarization in MoS2 monolayers by optical pumping. *Nature Nanotechnology* **7,** 490–493. ISSN: 1748-3387 (Aug. 2012).

184. Cao, T. *et al.* Valley-selective circular dichroism of monolayer molybdenum disulphide. *Nature Communications* **3,** 887. ISSN: 2041-1723 (June 6, 2012).

185. Jones, A. M. *et al.* Optical generation of excitonic valley coherence in monolayer WSe2. *Nature Nanotechnology* **8,** 634–638. ISSN: 1748-3387 (Sept. 2013).

186. Mak, K. F., McGill, K. L., Park, J. & McEuen, P. L. The valley Hall effect in MoS2 transistors. *Science* **344,** 1489–1492. ISSN: 0036-8075, 1095-9203 (June 27, 2014).

187. Lee, J., Mak, K. F. & Shan, J. Electrical control of the valley Hall effect in bilayer MoS2 transistors. *Nature Nanotechnology* **11,** 421–425. ISSN: 1748-3387 (May 2016).

188. Ye, Z., Sun, D. & Heinz, T. F. Optical manipulation of valley pseudospin. *Nature Physics* **advance online publication.** ISSN: 1745-2473. doi:10.1038/nphys3891. <http://www.nature.com/nphys/journal/vaop/ncurrent/full/nphys3891.html> (2016) (Sept. 19, 2016).

189. Rivera, P. *et al.* Valley-polarized exciton dynamics in a 2D semiconductor heterostructure. *Science* **351,** 688–691. ISSN: 0036-8075, 1095-9203 (Feb. 12, 2016).

190. Yu, T. & Wu, M. W. Valley depolarization due to intervalley and intravalley electron-hole exchange interactions in monolayer MoS2. *Physical Review B* **89,** 205303 (May 12, 2014).

191. Hao, K. *et al.* Direct measurement of exciton valley coherence in monolayer WSe2. *Nature Physics* **advance online publication.** ISSN: 1745-2473. doi:10.1038/nphys3674. <http://www.nature.com/nphys/journal/vaop/ncurrent/full/nphys3674.html> (2016) (Feb. 29, 2016).

192. Zhang, Y. J., Oka, T., Suzuki, R., Ye, J. T. & Iwasa, Y. Electrically Switchable Chiral Light-Emitting Transistor. *Science* **344,** 725–728. ISSN: 0036-8075, 1095-9203 (May 16, 2014).

193. Ye, Y. *et al.* Electrical generation and control of the valley carriers in a monolayer transition metal dichalcogenide. *Nature Nanotechnology* **11,** 598–602. ISSN: 1748-3387 (2016).

194. Cho, G. C., Kütt, W. & Kurz, H. Subpicosecond time-resolved coherent-phonon oscillations in GaAs. *Physical Review Letters* **65,** 764–766 (Aug. 6, 1990).

195. Merlin, R., Pinczuk, A. & Weber, W. H. in *Raman Scattering in Materials Science* (eds Weber, D. W. H. & Merlin, P. R.) *Springer Series in Materials Science* 42. DOI: 10.1007/978-3-662-04221-2_1, 1–29 (Springer Berlin Heidelberg, 2000). ISBN: 978-3-662-04221-2. <http://link.springer.com/chapter/10.1007/978-3-662-04221-2_1> (2016).

196. Zhang, X. *et al.* Phonon and Raman scattering of two-dimensional transition metal dichalcogenides from monolayer, multilayer to bulk material. *Chemical Society Reviews* **44,** 2757–2785 (2015).

197. SCOTT, J. F., LEITE, R. C. C. & DAMEN, T. C. Resonant Raman Effect in Semiconductors. *Physical Review* **188,** 1285–1290 (Dec. 15, 1969).

198. Thomsen, C. & Reich, S. Double Resonant Raman Scattering in Graphite. *Physical Review Letters* **85,** 5214–5217 (Dec. 11, 2000).

199. Sourisseau, C., Cruege, F., Fouassier, M. & Alba, M. Second-order Raman effects, inelastic neutron scattering and lattice dynamics in 2H-WS2. *Chemical Physics* **150,** 281–293. ISSN: 0301-0104 (Feb. 1, 1991).

200. Del Corro, E. *et al.* Excited Excitonic States in 1L, 2L, 3L, and Bulk WSe2 Observed by Resonant Raman Spectroscopy. *ACS Nano* **8,** 9629–9635. ISSN: 1936-0851 (Sept. 23, 2014).

201. Huang, J.-K. *et al.* Large-Area Synthesis of Highly Crystalline WSe2 Monolayers and Device Applications. *ACS Nano* **8,** 923–930. ISSN: 1936-0851 (Jan. 28, 2014).

202. Huang, W., Luo, X., Kwan Gan, C., Ying Quek, S. & Liang, G. Theoretical study of thermoelectric properties of few-layer MoS2 and WSe 2. *Physical Chemistry Chemical Physics* **16,** 10866–10874 (2014).

203. Amin, B., P. Kaloni, T. & Schwingenschlögl, U. Strain engineering of WS2 , WSe2 , and WTe2. *RSC Advances* **4,** 34561–34565 (2014).

204. Haug, A. Phonon-assisted intervalence band absorption in semiconductor lasers. *Semiconductor Science and Technology* **5,** 557. ISSN: 0268-1242 (1990).

205. Zhang, X.-X., You, Y. & Heinz, T. F. Experimental Evidence for Dark Excitons in Monolayer WSe2. *Physical Review Letters* **115,** 257403 (Dec. 15, 2015).

206. Wang, G. *et al.* Giant Enhancement of the Optical Second-Harmonic Emission of WSe2 Monolayers by Laser Excitation at Exciton Resonances. *Physical Review Letters* **114,** 097403 (Mar. 4, 2015).

207. Hsu, W.-T. *et al.* Optically initialized robust valley-polarized holes in monolayer WSe2. *Nature Communications* **6,** 8963. ISSN: 2041-1723 (Nov. 25, 2015).

208. Hoffman, C. & Driggers, R. *Encyclopedia of Optical and Photonic Engineering, Second Edition* -1. ISBN: 978-1-4398-5097-8. <http://www.crcnetbase.com/doi/book/10.1081/E-EOE2> (2016) (CRC Press, Aug. 27, 2015).

209. Riley, J. M. *et al.* Direct observation of spin-polarized bulk bands in an inversion-symmetric semiconductor. *Nature Physics* **10,** 835–839. ISSN: 1745-2473 (Nov. 2014).

210. Le, D. *et al.* Spin–orbit coupling in the band structure of monolayer WSe2. *Journal of Physics: Condensed Matter* **27,** 182201. ISSN: 0953-8984 (2015).

211. Kumar, N. *et al.* Exciton-exciton annihilation in MoSe2 monolayers. *Physical Review B* **89,** 125427 (Mar. 24, 2014).

212. Poellmann, C. *et al.* Resonant internal quantum transitions and femtosecond radiative decay of excitons in monolayer WSe2. *Nature Materials* **14,** 889–893. ISSN: 1476-1122 (Sept. 2015).

213. Shen, Z. *et al.* Experimental realization of optomechanically induced non-reciprocity. *Nature Photonics* **advance online publication.** ISSN: 1749-4885. doi:10.1038/nphoton.2016.161. <http://www.nature.com/nphoton/journal/vaop/ncurrent/full/nphoton.2016.161.html> (2016) (Aug. 22, 2016).

214. Bunch, J. S. *et al.* Electromechanical Resonators from Graphene Sheets. *Science* **315,** 490–493. ISSN: 0036-8075, 1095-9203 (Jan. 26, 2007).

215. Qi, J. *et al.* Piezoelectric effect in chemical vapour deposition-grown atomic-monolayer triangular molybdenum disulfide piezotronics. *Nature Communications* **6,** 7430. ISSN: 2041-1723 (June 25, 2015).

216. Kim, S. K. *et al.* Directional dependent piezoelectric effect in CVD grown monolayer MoS2 for flexible piezoelectric nanogenerators. *Nano Energy* **22,** 483–489. ISSN: 2211-2855 (Apr. 2016).

217. Chakraborty, B. *et al.* Symmetry-dependent phonon renormalization in monolayer MoS2 transistor. *Physical Review B* **85,** 161403 (Apr. 6, 2012).

218. Chen, C. *et al.* Modulation of mechanical resonance by chemical potential oscillation in graphene. *Nature Physics* **12,** 240–244. ISSN: 1745-2473 (Mar. 2016).

219. Mannebach, E. M. *et al.* Dynamic Structural Response and Deformations of Monolayer MoS2 Visualized by Femtosecond Electron Diffraction. *Nano Letters* **15,** 6889–6895. ISSN: 1530-6984 (Oct. 14, 2015).

220. Cremons, D. R., Plemmons, D. A. & Flannigan, D. J. Femtosecond electron imaging of defect-modulated phonon dynamics. *Nature Communications* **7,** 11230 (Apr. 15, 2016).

221. Ackerman, M. L. *et al.* Anomalous Dynamical Behavior of Freestanding Graphene Membranes. *Physical Review Letters* **117,** 126801 (Sept. 13, 2016).

222. Castellanos-Gomez, A. *et al.* Local Strain Engineering in Atomically Thin MoS2. *Nano Letters* **13,** 5361–5366. ISSN: 1530-6984 (Nov. 13, 2013).

223. He, K., Poole, C., Mak, K. F. & Shan, J. Experimental Demonstration of Continuous Electronic Structure Tuning via Strain in Atomically Thin MoS2. *Nano Letters* **13,** 2931–2936. ISSN: 1530-6984 (June 12, 2013).

224. Hui, Y. Y. *et al.* Exceptional Tunability of Band Energy in a Compressively Strained Trilayer MoS2 Sheet. *ACS Nano* **7,** 7126–7131. ISSN: 1936-0851 (Aug. 27, 2013).

225. Desai, S. B. *et al.* Strain-Induced Indirect to Direct Bandgap Transition in Multilayer WSe2. *Nano Letters* **14,** 4592–4597. ISSN: 1530-6984 (Aug. 13, 2014).

226. Manzeli, S., Allain, A., Ghadimi, A. & Kis, A. Piezoresistivity and Strain-induced Band Gap Tuning in Atomically Thin MoS2. *Nano Letters* **15,** 5330–5335. ISSN: 1530-6984 (Aug. 12, 2015).

227. Fu, D. *et al.* Mechanically modulated tunneling resistance in monolayer MoS2. *Applied Physics Letters* **103,** 183105. ISSN: 0003-6951, 1077-3118 (Oct. 28, 2013).

228. Song, S. *et al.* Room Temperature Semiconductor–Metal Transition of MoTe2 Thin Films Engineered by Strain. *Nano Letters* **16,** 188–193. ISSN: 1530-6984 (Jan. 13, 2016).

229. Nayak, A. P. *et al.* Pressure-induced semiconducting to metallic transition in multilayered molybdenum disulphide. *Nature Communications* **5,** 3731. ISSN: 2041-1723 (May 7, 2014).

230. Chi, Z.-H. *et al.* Pressure-Induced Metallization of Molybdenum Disulfide. *Physical Review Letters* **113,** 036802 (July 16, 2014).

231. Zhao, Z. *et al.* Pressure induced metallization with absence of structural transition in layered molybdenum diselenide. *Nature Communications* **6,** 7312. ISSN: 2041-1723 (June 19, 2015).

232. Fan, W. *et al.* Vibrational spectrum renormalization by enforced coupling across the van der Waals gap between MoS2 and WS2 monolayers. *Physical Review B* **92,** 241408 (Dec. 18, 2015).

233. Akinwande, D., Petrone, N. & Hone, J. Two-dimensional flexible nanoelectronics. *Nature Communications* **5,** 5678. ISSN: 2041-1723 (Dec. 17, 2014).

234. Woodruff, T. O. & Ehrenreich, H. Absorption of Sound in Insulators. *Physical Review* **123,** 1553–1559 (Sept. 1, 1961).

235. O'Connell, A. D. *et al.* Quantum ground state and single-phonon control of a mechanical resonator. *Nature* **464,** 697–703. ISSN: 0028-0836 (Apr. 1, 2010).

236. Chan, J. *et al.* Laser cooling of a nanomechanical oscillator into its quantum ground state. *Nature* **478,** 89–92. ISSN: 0028-0836 (Oct. 6, 2011).

237. Zhang, J., Li, D., Chen, R. & Xiong, Q. Laser cooling of a semiconductor by 40 kelvin. *Nature* **493,** 504–508. ISSN: 0028-0836 (Jan. 24, 2013).

238. Kittlaus, E. A., Shin, H. & Rakich, P. T. Large Brillouin amplification in silicon. *Nature Photonics* **10,** 463–467. ISSN: 1749-4885 (July 2016).